Development of immune checkpoint inhibitors made of PD-1 variants or small molecule derivatives

PD-1変異体あるいは小分子誘導体からなる免疫チェックポイント阻害剤の開発

March, 2023

Boyang NING
宁　博洋

Development of immune checkpoint inhibitors made of PD-1 variants or small molecule derivatives

PD-1変異体あるいは小分子誘導体からなる免疫チェックポイント阻害剤の開発

March, 2023

Waseda University Graduate School of Advanced Science and Engineering

Department of Life Science and Medical Bioscience, Research on Biomolecular Assembly

Boyang NING
宁　博洋

Table of contents

List of Abbreviations

APC	Antigen-presenting cells
ADC	Antibody-drug conjugate
BCN	Bicyclo[6.1.0]non-4-yne
BMS	Bristol-Myers Squibb
CAR-T	Chimeric antigen receptors T cell
cDNA	Complementary DNA
CFPS	Cell-free protein synthesis
CTLA-4	Cytotoxic T-lymphocyte associated antigen 4
DARPin	Ankyrin repeat proteins
EC_{50}	Half maximal effective concentration
FAM	Carboxyfluorescein
FDR	False discovery rate
HPV	Human papillomavirus
HER2	Human epidermal growth factor receptor 2
IC_{50}	Half maximal inhibitory concentration
ICI	Immune checkpoint inhibitor
IgV	Immunoglobulin variable
irAEs	Immune-related adverse events
ITIM	Immunoreceptor tyrosine-based inhibitory motif
Kd	Dissociation constant
mAb	Monoclonal antibody
MHC	Major histocompatibility complex
ncAA	Noncanonical amino acid
NGS	Next-generation sequencing
PAMAMG4	Generation 4 Poly(amidoamine)
PCA	Principal component analysis
PD-1	Programmed cell death 1
PD-L1	Programmed death-ligand 1
PRM	Peptide/ribosome/mRNA complex
PylRS	Pyrrolysyl-tRNA synthetase
scfv	Single-chain variable fragment
SHP	Src Homology 2 domain-containing phosphatase
SMI	Small molecular inhibitors
ssDNA	Single-stranded DNA
TAA	Tumor-associated antigens
T_C	Cytotoxic T cell
TME	Tumor microenvironment
Treg	Regulatory T cell
TSA	Tumor-specific antigens
WBT	Washing buffer used in ribosome display

Chapter I | Attempts to Develop Better Immune Checkpoint Inhibitor

1.1. General Introduction of Cancer Immune Therapy

1.1.1. Cancer and cancer therapy

Cancer is defined as a group of diseases involving uncontrollable cell growth of the transformed cell with the potential to spread to other parts of the body[1]. Cancer, together with infectious disease and cardiovascular disease, are three leading causes of death in industrialized nations.[1] Several cancer therapies exist and some of them are specialized for certain cancer types such as hormone therapy. In this section, I will introduce general cancer therapies including local therapy, traditional chemotherapy, and targeted therapy.

When the cancer is at its early stage, that is, before it starts to spread, local therapy such as surgery and radiation is effective. However, local therapy is not feasible for the systematic spread of tumors such as leukemia and metastatic tumors. The traditional method is chemotherapy with cytotoxic drugs which interfere with the process of mitosis and cause apoptosis. However, traditional indiscriminately kill both tumor cells and normal cells, causing server adverse effects and encountering the problem of drug resistance. On the other hand, target therapy seeks to specifically remove cancer cells while keeping healthy cells. For example, the antibody-drug conjugate (ADC) uses an antibody to target cancer-specific surface antigens and carries cytotoxic drugs to kill the cancer cell. However, traditional ADCs, for example, the T-DM1 which targets HER2, failed to show the anti-cancer effect for HER2 low-expression cells, limiting their application.[2] Moreover, cancer cells could evolve to alter the cytotoxic drug's metabolism and finally obtain drug resistance.[3,4] Although encountered the above difficulties, the Trastuzumab deruxtecan, developed by the Daichi Sankyo company, shows a bystander effect owing to its novel cytotoxic drug payload. Trastuzumab deruxtecan exhibited significant efficacy for HER2-low expression patients at phase 3 clinical trial and becomes the first FDA- approved ADCs to treat HER2-low advanced breast cancer[5], throwing light on the next generation ADCs. On the other hand, without directly killing cancer cells, immunotherapy manipulates the immune response to indirectly kill cancer cells even without knowing the precise targets.[6]

1.1.2. T cell priming and activation process

As early as the 1950s, Frank MacFarlane Burnet, recipient of the 1960 Nobel Prize, and Lewis Thomas independently built the first immunosurveillance hypothesis, according to which cells of the immune system are responsible for detecting and destroying tumor cells[7]. Although the natural killer cell also was reported with an anti-cancer effect[8], the anti-cancer effect of the T cell is most well-studied. In this section, I will review the anti-cancer process of T cells and general tumor antigens.

As shown in **Figure 1.1.1**, the process from T cell activation to the final elimination of cancer cells is composed of seven stages and called as cancer-immunity cycle[9]. In the 1st stage, the cancer cell antigens are released due to cancer cell death and are captured by antigen-presenting cells (APCs). In the 2nd stage, APCs process the antigen and present the antigen with the major histocompatibility complex (MHC) on the cell surface. In the 3rd stage, naive T cells meet the APCs at the lymph node and are activated by the APCs. The activated naïve T cell differentiates to be the effector T cell. One kind of effector T cell, the cytotoxic T cell (Tc), traffics to the tumor site (4th stage) and infiltrates into the tumor site (5th stage). After recognizing the MHC/antigen complex of the tumor cell with TCR (6th stage), the Tc kills the tumor cell by releasing the cytotoxic granule and cytokines (7th stage).

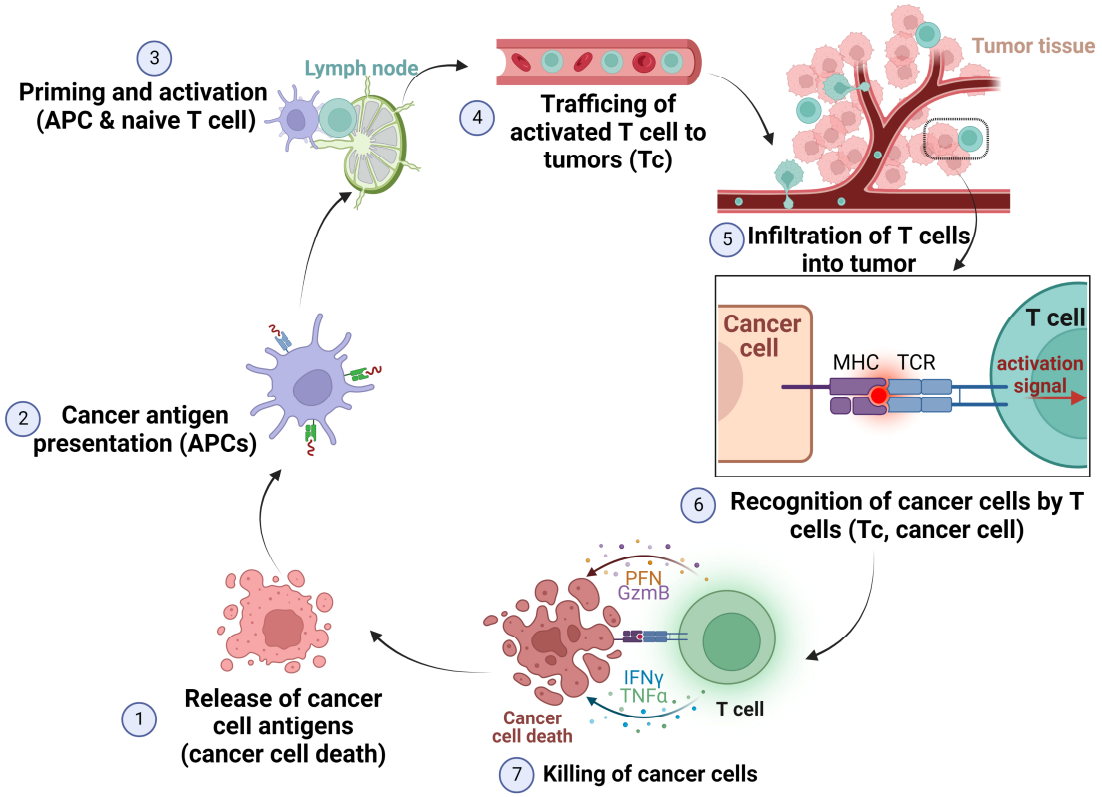

Figure 1.1.1. The seven stages of the cancer-immunity cycle [9]. Cancer antigen released from cancer cell death (1st stage) is captured and presented by the APCs (2nd stage). Two stimulation signals of MHC/TCR and B7/CD28 together primer and activate the naïve T cell to the effector cells (3rd stage). One of the effector

cells of Tc traffics (4th stage) and infiltrates into tumor tissue (5th stage). After recognizing the tumor antigen (6th stage), Tc kills cancer cells through the immune attack (7th stage). APCs: antigen-presenting cell; Tc: Cytotoxic T cell; MHC: major histocompatibility complex; TCR: T cell receptor; PFN: perforin. GzmB: granzyme B. This picture was drawn based on the content from other reference [9] under the license number of 5495291172675 (Copyright © 2013 Elsevier Inc. All rights reserved.)

The ability of the T cell to recognize tumor antigens forms the basis of immunotherapies. Three types of cancer antigens could be recognized by T cells[10]. The first is tumor-specific antigens (TSAs), also referred to as nonpeptides, mainly resulting from several tumor-specific genomic aberrations, such as point mutation, indels, and gene fusions. They are highly immunogenic since they are recognized as foreign. However, they are often unique to each patient [10] and therefore difficult to be directly used for drug design. Most tumor filtration T cells recognize this type of antigen. The adoptive T-cell therapies which *ex vivo* expand the patient-isolated tumor-infiltrating T cell and reinfuse back to patients, hold the promise to utilize this type of antigens[11]. The second is viral antigens, which are also highly immunogenic but not necessarily expressed by the tumor cell[10], such as human papillomavirus (HPV). To those antigens, the vaccine is a better choice rather than targeting infected tumor cells. The third is tumor-associated antigens (TAAs), self-antigens that are not specifically expressed in tumors. For example, NY-ESO-1 is normally expressed in the germline genome but could be detected in serval human tumors. Gp100 is specifically expressed by melanocytes and is the common melanoma antigen[12]. HER2 is expressed in various normal tissue[13] but is overexpressed in tumor cells. However, since the TAAs are self-antigens, a process known as central tolerance eliminates the T cells (also B cells) which have a high-affinity TCR for self-antigens before they leave the primary lymphoid organ and become naïve T cells[14]. Therefore, TAAs generally exhibit weak immunogenicity[10,15], and nature T cells that recognize TAAs have low potency since their TCR binds weakly to TAAs. The chimeric antigen receptors T cell (CAR-T) replaces the nature TCR with an artificial TCR, coupling with other co-stimulation molecules, to enhance the anti-tumor effect of T cell [16].

Although central tolerance could delete the majority of self-reactive T cells, low-affinity self-reactive T cells could survive this surveillance and escape to the periphery[17]. To prevent autoimmunity, the activity of T cells is regulated at multiple stages via multiple co-stimulatory and inhibitory regulators, called immune checkpoints[18]. The most two well-known inhibitory immune checkpoints are lymphocyte antigen 4 (CTLA-4) and programmed cell death 1 (PD-1).

1.1.3. Immune checkpoints and cancer

In this section, I will review the biological function of CTLA-4 and PD-1 immune checkpoints and explain how cancer cell utilizes those immune checkpoints for escaping immunosurveillance as shown in **Figure 1.1.2**.

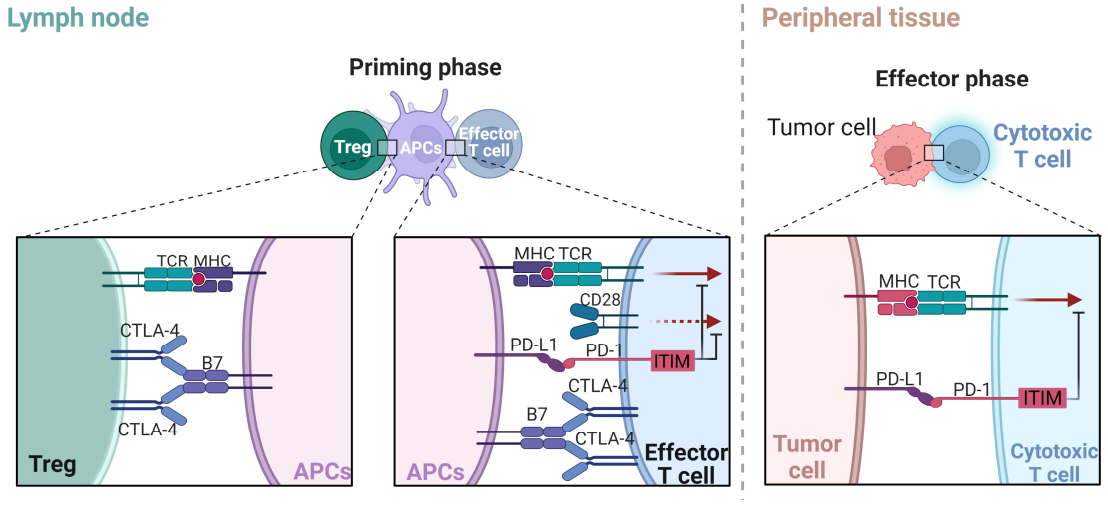

Figure 1.1.2. The immune inhibitory mechanism of CTLA-4 and PD-1 [1]. CTLA-4 is expressed in the activated T cell and Treg cell. Because CTLA-4 depletes the CD28's ligand of B7, T cells could not be activated due to the loss of the second activation signal from CD28. CTLA-4 could multivalently bind with B7 with a higher affinity than CD28. On the other hand, PD-1 is expressed in T cells and after binding with its ligand of PD-L1, the ITIM motif of PD-1 could recruit phosphatase to inactive TCR signaling as well as CD28 signaling. ITIM: immunoreceptor tyrosine-based inhibitory motif. This figure was drawn based on content of the textbook [1].

In the third stage of **Figure 1.1.1**, the activation of prime T cells with APCs needs serval signals. The first signal comes from the interaction between the TCR and MHC/antigen complex as well as TCR co-receptor CD8/MHC-I. Those interactions trigger the phosphorylation of several key molecules for signal transduction. Besides, the second signal, triggered by the interaction between CD28 and B7 is necessary to prevent T cell anergy[19]. CD28 is a homodimer protein expressed on the surface of naïve T cells. The co-stimulatory ligands of CD28 are B7 molecules, including B7-1 (CD80) and B7-2 (CD86), expressed on the surface of APCs as homodimers. CTLA-4 initially resides on intracellular membranes but moves to the T cell surface after prime T cell activation[20] and regulatory T cells (Treg) constitutionally express high levels of CTLA-4 on their surface[21]. Similar to CD28, CTLA-4 is expressed as a homodimer but could bind with B7 with a higher affinity[22]. Besides, unlike CD28, which binds one dimer of B7, one dimer of CTLA-4 could bind two B7 dimers, exhibiting an avidity advantage[23]. Moreover, CTLA-4 medicates the internalization and degradation of B7[24]. Although it has been reported that CTLA-4 could activate inhibitory signal[25], the inhibition mechanism of CTLA-4 is considered by depleting the ligand of the co-stimulatory receptor CD28. Since the co-stimulatory signal of CD28/B7 is only necessary for

the activation of naïve T cells (priming phase) but not in the process of activation of cytotoxic T cells (effector phase), CTLA-4 exerts its regulatory effect mainly at the priming stage within lymphoid organs. CTLA-4 is important in immune checkpoint regulation as human patients with genetic CTLA-4 deficiency exhibit severe lymphocytic infiltration and autoimmunity[26].

On the other hand, PD-1 differs from CTLA-4 in the mechanism and stage. T cells express PD-1 on the cell surface after TCR stimulation[27,28]. PD-1 is a type 1 transmembrane protein containing the immunoreceptor tyrosine-based inhibitory motif (ITIM) in its cytoplasmic region[29]. PD-1 has two kinds of ligand, both belonging to the B7 homologs, PD-L1 and PD-L2. PD-L1 is constitutively expressed in various types of cells, including both lymphocyte and nonlymphocytic cell[30], whereas PD-L2 is mainly expressed in APCs. After PD-1 binding to its ligand PD-L1 or PD-L2, the tyrosine in ITIM is phosphorylated and recruits the SH2-containing phosphatase (SHP). SHP could remove phosphate groups from many phosphorylated proteins, thus inactive TCR signaling as well as CD28 signaling[31] and finally induce T cell exhaustion. Therefore, PD-1 exerts its regulatory effect by direct block the signal transduction at both the priming phase and effector phase. Compared to the mice lacking CTLA-4 who died at 3-4 weeks of age from uncontrolled lymphoproliferation[32], PD-1 deficient mice live longer with an autoimmune dilated cardiomyopathy[33].

Nowadays, it is appreciated that the relationship between the immune system and cancer is more complex and was summarized into the conceptual framework called “cancer immunoediting”[7]. The immune system could eliminate cancer cells but also select the cancer cell that could finally escape from the immune system. Cancer cells could avoid immune recognition in a variety of ways, one of which is tumor-induced immune suppression. Cancer cells could attract inhibitory Treg cells to the tumor microenvironment (TME) via several chemokines. Treg cells are inhibitory T cells with high expression of CTLA-4 on their surface and could suppress immune functions through various mechanisms including CTLA-4 mediated suppression[34]. On the other hand, various cancer cells show high PD-L1 expression on their surface[35]. Besides, cancer cells could secrete PD-L1 to mediate immunosuppression[36,37]. Given these facts, it has been proposed the inhibition of immune points could be used as a cancer treatment.

1.1.4. Success and limitation of antibody immune checkpoint inhibitors (ICIs):

In this section, I will summarize the clinical results of antibody ICIs and list the limitations of ICIs from mechanistic and pharmaceutical viewpoints.

In 2011, Ipilimumab, a human IgG1 anti-CTLA-4 monoclonal antibody (mAb), gained FDA approval for the treatment of non-resectable stage III/IV melanoma, based on the result that Ipilimumab could confer the overall survival of 10.1 months to the patients [38]. Later, long-term survival data demonstrated the three-year survival rate is 22% among all Ipilimumab-treated patient[39]. However, Ipilimumab shows less potency in other cancer types[40,41] and therefore it only has been approved for treating melanoma. On the other hand, in 2014, human IgG4 anti-PD-1 mAb nivolumab and pembrolizumab were approved by FDA for treating refractory and unresectable melanoma. In the clinical trials [42], the one-year survival rate of nivolumab-treated patients is 72.9%, while for chemotherapy-treated patients the one-year survival rate is 42.1%. Since then, nivolumab and pembrolizumab extend their indications for various cancer types, such as non-small-cell lung carcinoma[43,44]. Similarly, the anti-PD-L1 mAb, such as atezolizumab, was approved for the treatment of various cancer[45]. Given this success, James P. Allison and Tasuku Honjo, who discovered the CTLA-4 and PD-1, respectively, won the 2018 Nobel Prize in Physiology or Medicine.

Although ICIs exhibit unprecedented potency, they have limitations such as adverse effects and a relatively low clinical response rate. Overall, the adverse effect of ICIs is better tolerable than traditional chemotherapeutics[46]. Since immune checkpoints have an important role in preventing autoimmunity, the adverse effects of their inhibition are mainly related to immune systems and are thus called immune-related adverse events (irAEs)[47]. The most common event is skin manifestations such as mucositis and pruritus, observed in 47%-68% of patients treated with anti-CTLA-4 antibodies and 30-40% of patients treated with anti-PD-1 or anti-PD-L1 antibodies[48]. For the severe events requiring intervention, 30 % were observed in anti-CTLA-4-treated patients and 15% were observed in anti-PD-1 or anti-PD-L1 treated patients[47]. From clinical results, anti-CTLA-4 therapy generally has a higher risk of severe irAEs than anti-PD-1/PD-L1 therapies[49], which is consistent with the animal experiment[32,33]. Besides irAEs, the clinical response rate is different with cancer types and generally low. For example, in the clinical trials of nivolumab, the response rate is 28% in advanced melanoma, 18% in non-small-cell lung cancer, and 27% in renal cell carcinoma[50]. Based on the anti-cancer process of T cells, the main biological reasons could be given as low immunogenicity of cancer cells [51], insufficient T cell trafficking and infiltration [52], as well as the existence of other immune suppression mechanisms in the tumor microenvironment [53]. Since the above reasons of low response are intrinsically related to the mechanism of ICIs, a combination with other therapy is necessary. For example, SGN-PDL1V, an ADC drug constructed from anti-PD-L1 mAb and vedotin drug-linker, showed activity even in low PD-L1 expression mice experiment and is now under the Phase 1 study[54]. Besides these mechanistic reasons, given the fact that mAb is the only approved ICI drug, there are some pharmaceutical limitations

for antibody ICIs.

Firstly, the large-size and neonatal Fc receptor-mediated recycling[55] contributes to the slow clearance of antibodies, which means the irAEs will continue for a long time even after stopping the drug administration[56]. Secondly, it was reported that antibodies have a poor distribution in the tumor region distal to the blood vessel[57]. Since the infiltration rate of T cells into the tumor is highly related to the response to ICIs treatment [52], the poor distribution may lead to incomplete inactivation of T cells. Thirdly, compared to prokaryote protein production or chemical synthesis, antibody production with mammalian cells has many challenges in large-scale cell culture and has a limited production yield[58], which increases the manufacturing cost. The above drawbacks motivate me to develop novel inhibitors with smaller molecular sizes and lower manufacturing costs. Since the PD-1/PD-L1 inhibitors generally have milder side effects and better therapeutic potency when compared with CTLA-4, I choose PD-1/PD-L1 as my study target and the following introduction will focus on PD-1/PD-L1 immune checkpoints.

1.1.5. Structural characteristic of PD-1/PD-L1 complex

In this chapter, I will explain the structural difficulty of designing the PD-1/PD-L1 ICIs.

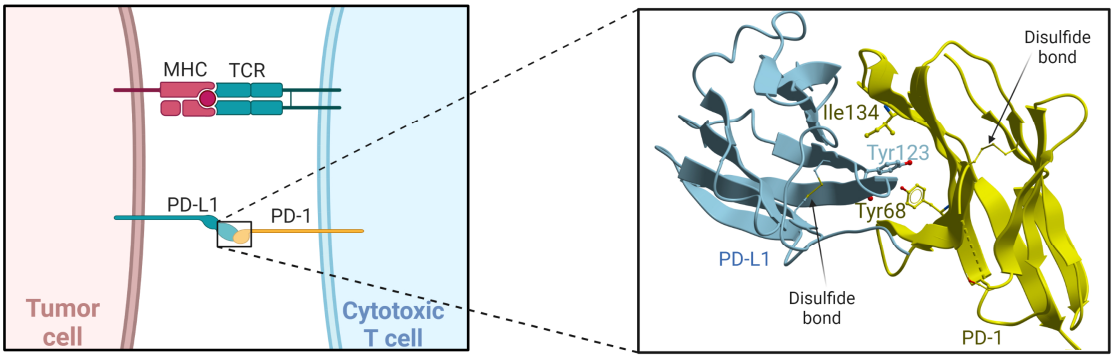

Figure 1.1.3. The crystal structure of the human PD-1/PD-L1 IgV-like domain (retrieved from PDB: 4zqk [59]). A characteristic two-layer β-sheet sandwich structure can be observed for both PD-1 and PD-L1. Disulfide was marked on the graph as it stabilizes the two β-sheets. The Tyr123 of PD-L1 and Tyr68/Ile134 of PD-1 are marked on the graph as Tyr123 form π-π stacking and alkyl-π interaction with Try68 and Ile134, respectively. The crystal structure was retrieved from Zak, K.M., Dubin, G., Holak, T.A. (2015) Structure of the complex of human programmed death-1 (PD-1) and its ligand PD-L1 doi: 10.2210/pdb4ZQK/pdb.

The extracellular domain of PD-1 and PD-L1 consists of an N-terminal domain followed by a typical immunoglobulin variable (IgV) like domain. In 2015, Zak et al [59] revealed the crystal structure of the human PD-1/PD-L1 complex. According to the crystal structure (**Figure 1.1.3**), the IgV-like domain has a two-layer β-sheet sandwich structure and is stabilized by a single inter-sheet disulfide bond. PD-1 and PD-L1 interact with each other through their front sheet of IgV domain, forming a huge contact surface area of 1,970 Å^2. The core of this contact surface is mainly formed by hydrophobic interaction including the π-π stacking and alkyl-π interaction between PD-1 (i.e., Val64, Tyr68, Ile126, Leu128, Ala132, Ile134) and PD-L1 (i.e., Ile54, Tyr56, Met115, Ala121, Tyr123) [59]. Furthermore, the PD-1/PD-L1 contact surface is relatively flat and lacks a suitable binding pocket. Given these properties, small molecule inhibitors are difficult to be designed since their small molecular size only provided a limited contact surface area [60]. Besides, the inhibitors tend to have many hydrophobic groups which will decrease their water-solubility. In fact, this surface is not a favored target for many approved antibodies, for example, nivolumab binds to the N-terminal loop in the PD-1 domain[61].

1.1.6. Current emerging non-IgG PD-1/PD-L1 ICIs

Although the PD-1/PD-L1 complex is a difficult target for drug design, many ICIs are discovered through high-throughput screening. In this section, emerging non-IgG ICIs of small molecular inhibitors (SMI), peptide inhibitors, and protein inhibitors will be introduced.

In 2015, a patent owned by Bristol-Myers Squibb (BMS) company screened out a series of compounds that could inhibit PD-1/PD-L1 interaction and thus called BMS compounds (**Figure 1.1.4**)[62]. The general structure contains a core 2-substituted biphenyl group and an additional aryl group, linked together with a two-atom spacer. In 2016, Zak et al. revealed the crystal structure of BMS-202/PD-L1 and found that the BMS compound exerts its inhibition effect by inducing the dimerization of PD-L1 [63]. Specifically, the core group mainly interacts with the Ala121 and Met115 of both PD-L1 through, while the aryl group mainly interacts with one of the PD-L1's Tyr56. The above interaction involves hydrophobic interactions such as π-alkyl interactions and π-π stacking and together forming a cylindrical binding cleft. Since then, tens of BMS-compounds-like inhibitors with superior activity and drug properties have been published in patents and papers[64]. For example, adding a substituent group of 2,3-dihydro-1,4-benzdioxine to the other side of the core biphenyl created enhanced inhibitors, such as BMS-1166 [65]. Besides, since the induced PD-L1 homodimer has a symmetry conformation, symmetric inhibitors such as LH1307[66] or Compound-4[67] were created with superior activities. Furthermore, some derivatives indicate that the two-atom spacer is an alternative[68], and the core biphenyl group or aryl group could be replaced by other aromatic heterocycles as well (A22)[69]. Besides BMS compounds, other small molecules with novel structures have also been reported[70,71], however, they lack the co-crystal structural data to support their inhibition mechanism. The major challenge for current BMS-like small molecules is their acute cytotoxicity and low bioactivity. For example, although BMS-1166 has the top-level performance of cytotoxicity and bioactivity among the BMS compounds, it still shows cytotoxicity with half-maximal death concentration of 40.5 μM and could not fully activate T cell at its maximum nontoxic concentration in the cell assay[72].

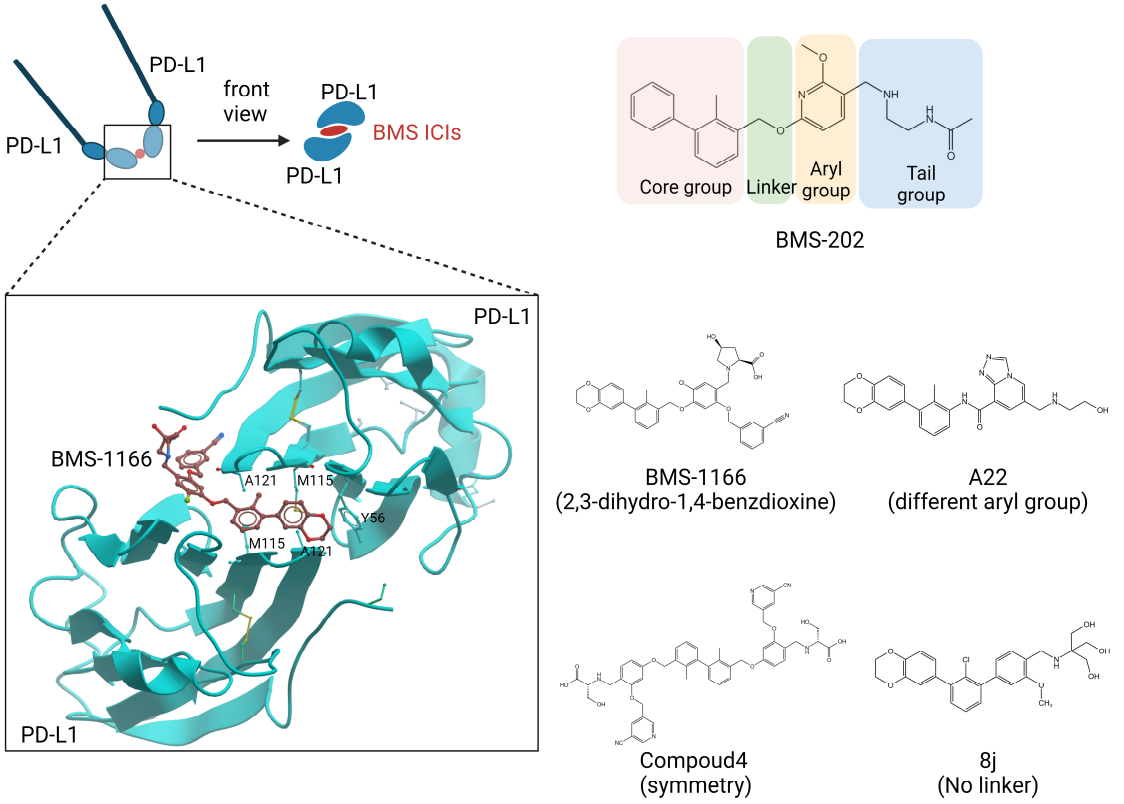

Figure 1.1.4. The mechanism of action and structure of BMS SMIs. BMS SMIs induced the PD-L1 dimerization to indirectly inhibit PD-1/PD-L1 interaction [62,63]. From the front view, the two PD-L1s are almost symmetry. The common structure is composed of a core group of the 2-substituted biphenyl group, a two-atom linker, an aryl group, and a tail group. Characteristic derivatives are listed at the right bottom of the figure. Some main interaction residues are marked in the graph. The crystal structure of BMS-1166/PD-L1 was retrieved from the Zak, K.M., Grudnik, P., Skalniak, L., Dubin, G., Holak, T.A. (2019) Structure of human Programmed cell death 1 ligand 1 (PD-L1) with low molecular mass inhibitor doi: 10.2210/pdb6R3K/pdb.

BMS compounds circumvent the problem of their limited protein contact area by inducing PD-L1 dimerization. However, for direct inhibition of PD-1/PD-L1 interaction, a large molecular is necessary to provide enough contact area. Therefore, the peptide inhibitor was developed since they process this property. The most well-studied peptide inhibitors are a series of cyclic peptides co-developed by BMS company with PEPTIDREAM INC company[73]. Within BMS peptides, peptide-57, peptide-71, and p101 (**Figure 1.1.5**) were studied for their co-crystal structure with PD-L1[74,75]. The structures showed that the two peptides work as anti-PD-L1 antibodies by directly binding with PD-L1 to inhibit PD-1 binding. Furthermore, BMS-986189 has passed the phase I clinical trial with promising safety and pharmacokinetics properties and its analog starts a new phase I clinical trial in 2022 (ISRCTN17572332). Besides cyclic BMS peptides, there are many other peptides have been developed, such as the D-peptides[76]. Compared to BMS small molecules, the BMS peptides show no cytotoxicity and could fully activate T cells. However, most of peptide ICIs's bioactivity is still much weaker than approved antibodies ICIs (i.e., the EC_{50} of nivolumab is 1.27 nM[74] while the EC_{50} of

p101 is 7.5 μM[75]).

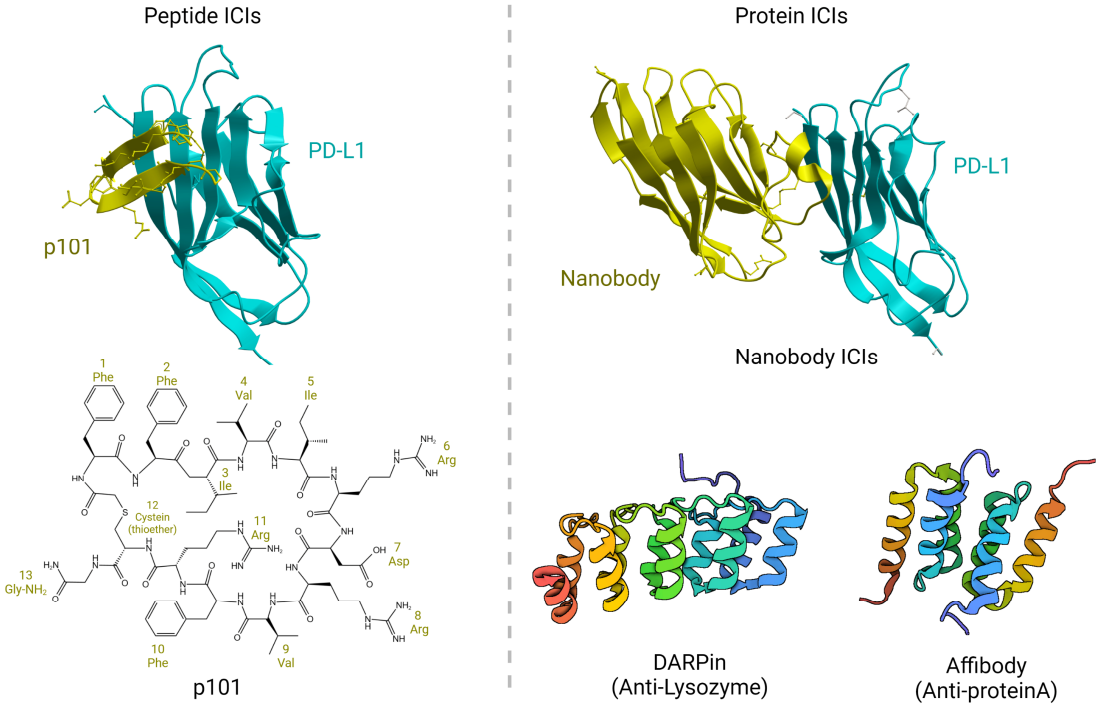

Figure 1.1.5. The peptide and protein ICIs. The crystal structure of peptide ICIs of p101 and PD-L1 is presented at the left top [78]. The chemical structure of p101 is presented at left bottom [75]. The Cys12 is reactivated with 1st residue of N-Chloroacetyl-L-phenylalanine to form the cyclic peptide. PD-1/PD-L1 targeted DAPRins and Affibodies have no available crystal structure. Instead of that, the characteristic crystal structure representation is shown at the right bottom (PDB:5OOU & PDB: 2M5A). The structure of p101/PD-L1 complex was retrieved from Zyla, E., Dubin, G. (2021) Structure of human PD-L1 in complex with macrocyclic inhibitor dio: 10.2210/pdb7OUN/pdb. The structure of the nanobody was retrieved from Zhou, A., Wei, H. (2016) Crystal structure of PD-L1 complexed with a nanobody at 1.7 Angstron resolution doi: 10.2210/pdb5JDS/pdb. The structure of DARPin was retrieved from Fischer, G., Hogan, B.J., Houlihan, G., Edmond, S., Huovinen, T.T.K., Hollfelder, F., Hyvonen, M. (2017) Designed Ankyrin Repeat Protein (DARPin) YTRL-1 selected by directed evolution against Lysozyme doi: 10.2210/pdb5OOU/pdb. The structure of Affibody was retrieved from Hard, T. (2013) Protein A binding by an engineered Affibody molecule doi: 10.2210/pdb2M5A/pdb.

The target-recognizing motif of antibodies is within their IgV domains. Therefore, using the variable domain, a simplified protein inhibitor could be created. For example, the single-chain variable fragment (scfv)[77] or nanobody[78] (**Figure 1.1.5**) has been developed as the PD-1/PD-L1 inhibitor. On the other hand, PD-1 has been used as a scaffold for developing as a PD-L1 inhibitor since the extracellular domain of PD-1 an IgV-like domain. As an example, a high-affinity PD-1 extracellular mutant named HAC has been developed by yeast display and showed a stronger inhibition effect than antibodies[79]. Apart from the IgV scaffold, other alternative scaffolds have also been used for developing PD-1/PD-L1 protein inhibitors. For example, inhibitors composed of α-helix structures (**Figure 1.1.5**) like the ankyrin repeat

proteins (DARPin®) scaffold[80] and the affibody scaffold have been reported[81]. Generally, protein inhibitors could achieve comparable *in vitro* bioactivity as antibodies due to their large contact surface. However, since most protein ICIs are either non-human proteins or bear many mutations, they may have higher immunogenicity than humanized ICI antibodies, where *in vivo* therapeutic effects would be dampened by anti-drug antibodies.

1.2. Purpose and Strategy of This Study

This study aimed to develop novel PD-1/PD-L1 ICIs with a lower manufacturing cost and a smaller molecular size while having a comparable inhibitory effect with antibodies. Therefore, I focused on the improvements of current non-IgG ICIs to develop three novel ICIs as described in the following three chapters.

In chapter 2, the development of a protein ICI was described. Current protein ICIs are highly either made from exogenous protein scaffolds or bearing many mutations. PD-1 is an endogenous binder of PD-L1 and could be easily produced by *E. coli*. However, the wild-type PD-1 has a weak binding affinity with PD-L1 (Kd around 6 μM) [82] which limits its competitive inhibition ability. To obtain a high-affinity PD-1 mutant without introducing unnecessary mutations to increase its immunogenicity. Accurate mutagenesis was performed by combining the *in silico* mutagenesis and in-cell verification.

In chapter 3, the development of a noncanonical peptide ICI was described. Current peptide ICIs lack the key molecular to provide the target-binding interaction which is presumably the reason for their compromised bioactivity. Besides, SMIs could not directly inhibit PD-1/PD-L1 interaction due to their limited PD-1/PD-L1 interaction surface area, which presumably leads to their low bioactivity and cytotoxicity. To overcome the disadvantage of SMIs and peptide ICIs, SMI was incorporated into the peptide library for discovering a potent noncanonical peptide ICI via PD-L1 binding screening.

In chapter 4, the development of an SMI-conjugated dendrimer was described. The current SMI showed low bioactivity and high cytotoxicity[83]. To utilize the current SMI, multivalent conjugation of SMI to a nanocarrier was considered. Firstly, the multivalent effect could increase the inhibition activity of SMI. Secondly, the SMI could target PD-L1 and deliver the nanocarrier to the PD-L1-expressing tumor site. Thirdly, the immune checkpoint inhibition and cytotoxicity from SMI and the therapeutic drug could provide a synergic anti-cancer effect. Overall, three novel ICIs were developed in this thesis, and they together could be used for expanding the modality of early ICIs drug discovery.

In chapter 5, a conclusion and prospects would be described. This thesis used novel methods to develop the improved protein ICI, the SMI-peptide ICI, and the SMI-conjugated polymer ICI for achieving a better therapeutic effect. Although currently the bioactivity is not as high as the best non-antibody ICIs, these novel ICIs provided new type of inhibitors and is promising to become more potent with structural optimization.

References

1. Murphy, K. (Kenneth M.). *Janeway's immunobiology*. (Garland Science, Taylor & Francis Group, 2017).
2. Ogitani, Y. *et al.* DS-8201a, A Novel HER2-Targeting ADC with a Novel DNA Topoisomerase I Inhibitor, Demonstrates a Promising Antitumor Efficacy with Differentiation from T-DM1. *Clinical Cancer Research* **22**, 5097–5108 (2016).
3. Drago, J. Z., Modi, S. & Chandarlapaty, S. Unlocking the potential of antibody–drug conjugates for cancer therapy. *Nat Rev Clin Oncol* **18**, 327–344 (2021).
4. Mansoori, B., Mohammadi, A., Davudian, S., Shirjang, S. & Baradaran, B. The Different Mechanisms of Cancer Drug Resistance: A Brief Review. *Adv Pharm Bull* **7**, 339–348 (2017).
5. Modi, S. *et al.* Trastuzumab Deruxtecan in Previously Treated HER2-Low Advanced Breast Cancer. *New England Journal of Medicine* **387**, 9–20 (2022).
6. Haen, S. P., Löffler, M. W., Rammensee, H.-G. & Brossart, P. Towards new horizons: characterization, classification and implications of the tumour antigenic repertoire. *Nat Rev Clin Oncol* **17**, 595–610 (2020).
7. Schreiber, R. D., Old, L. J. & Smyth, M. J. Cancer Immunoediting: Integrating Immunity's Roles in Cancer Suppression and Promotion. *Science (1979)* **331**, 1565–1570 (2011).
8. Shimasaki, N., Jain, A. & Campana, D. NK cells for cancer immunotherapy. *Nat Rev Drug Discov* **19**, 200–218 (2020).
9. Chen, D. S. & Mellman, I. Oncology Meets Immunology: The Cancer-Immunity Cycle. *Immunity (Cambridge, Mass.)* **39**, 1–10 (2013).
10. Jhunjhunwala, S., Hammer, C. & Delamarre, L. Antigen presentation in cancer: insights into tumour immunogenicity and immune evasion. *Nat Rev Cancer* **21**, 298–312 (2021).
11. Morotti, M. *et al.* Promises and challenges of adoptive T-cell therapies for solid tumours. *Br J Cancer* **124**, 1759–1776 (2021).
12. Bakker, A. B. *et al.* Melanocyte lineage-specific antigen gp100 is recognized by melanoma-derived tumor-infiltrating lymphocytes. *Journal of Experimental Medicine* **179**, 1005–1009 (1994).
13. Press, M. F., Cordon-Cardo, C. & Slamon, D. J. Expression of the HER-2/neu proto-oncogene in normal human adult and fetal tissues. *Oncogene* **5 7**, 953–62 (1990).
14. Rose, N. R. Molecular mimicry and clonal deletion: A fresh look. *J Theor Biol* **375**, 71–76 (2015).
15. Fraietta, J. A. *et al.* Determinants of response and resistance to CD19 chimeric antigen receptor (CAR) T cell therapy of chronic lymphocytic leukemia. *Nat Med* **24**, 563–571 (2018).
16. Waldman, A. D., Fritz, J. M. & Lenardo, M. J. A guide to cancer immunotherapy: from T cell basic science to clinical practice. *Nat Rev Immunol* **20**, 651–668 (2020).

17. Malhotra, D. *et al.* Tolerance is established in polyclonal CD4+ T cells by distinct mechanisms, according to self-peptide expression patterns. *Nat Immunol* **17**, 187–195 (2016).
18. Fife, B. T. & Bluestone, J. A. Control of peripheral T-cell tolerance and autoimmunity via the CTLA-4 and PD-1 pathways. *Immunol Rev* **224**, 166–182 (2008).
19. Harding, F. A., McArthur, J. G., Gross, J. A., Raulet, D. H. & Allison, J. P. CD28-mediated signalling co-stimulates murine T cells and prevents induction of anergy in T-cell clones. *Nature* **356**, 607–609 (1992).
20. Darlington, P. J. *et al.* Surface Cytotoxic T Lymphocyte–associated Antigen 4 Partitions Within Lipid Rafts and Relocates to the Immunological Synapse under Conditions of Inhibition of T Cell Activation. *Journal of Experimental Medicine* **195**, 1337–1347 (2002).
21. Tai, X. *et al.* Basis of CTLA-4 function in regulatory and conventional CD4+ T cells. *Blood* **119**, 5155–5163 (2012).
22. van der Merwe, P. A., Bodian, D. L., Daenke, S., Linsley, P. & Davis, S. J. CD80 (B7-1) Binds Both CD28 and CTLA-4 with a Low Affinity and Very Fast Kinetics. *Journal of Experimental Medicine* **185**, 393–404 (1997).
23. Linsley, P. S. *et al.* Human B7-1 (CD80) and B7-2 (CD86) bind with similar avidities but distinct kinetics to CD28 and CTLA-4 receptors. *Immunity* **1**, 793–801 (1994).
24. Qureshi, O. S. *et al.* Trans-endocytosis of CD80 and CD86: A molecular basis for the cell-extrinsic function of CTLA-4. *Science (1979)* **332**, 600–603 (2011).
25. Marengère, L. E. M. *et al.* Regulation of T Cell Receptor Signaling by Tyrosine Phosphatase SYP Association with CTLA-4. *Science (1979)* **272**, 1170–1173 (1996).
26. Lo, B. *et al.* CHAI and LATAIE: new genetic diseases of CTLA-4 checkpoint insufficiency. *Blood* **128**, 1037–1042 (2016).
27. Agata, Y. *et al.* Expression of the PD-1 antigen on the surface of stimulated mouse T and B lymphocytes. *Int Immunol* **8**, 765–772 (1996).
28. Ishida, Y., Agata, Y., Shibahara, K. & Honjo, T. Induced expression of PD-1, a novel member of the immunoglobulin gene superfamily, upon programmed cell death. *EMBO J* **11**, 3887–3895 (1992).
29. Keir, M. E., Butte, M. J., Freeman, G. J. & Sharpe, A. H. PD-1 and Its Ligands in Tolerance and Immunity. *Annu Rev Immunol* **26**, 677–704 (2008).
30. Freeman, G. J. *et al.* Engagement of the Pd-1 Immunoinhibitory Receptor by a Novel B7 Family Member Leads to Negative Regulation of Lymphocyte Activation. *Journal of Experimental Medicine* **192**, 1027–1034 (2000).
31. Hui, E. *et al.* T cell costimulatory receptor CD28 is a primary target for PD-1–mediated inhibition. *Science (1979)* **355**, 1428–1433 (2017).
32. Tivol, E. A. *et al.* Loss of CTLA-4 leads to massive lymphoproliferation and fatal multiorgan tissue destruction, revealing a critical negative regulatory role of CTLA-4. *Immunity* **3**, 541–547 (1995).
33. Nishimura, H. *et al.* Autoimmune Dilated Cardiomyopathy in PD-1 Receptor-Deficient Mice. *Science (1979)* **291**, 319–322 (2001).

34. Ohue, Y. & Nishikawa, H. Regulatory T (Treg) cells in cancer: Can Treg cells be a new therapeutic target? *Cancer Sci* **110**, 2080–2089 (2019).
35. Wang, X., Teng, F., Kong, L. & Yu, J. PD-L1 expression in human cancers and its association with clinical outcomes. *Onco Targets Ther* **9**, 5023–5039 (2016).
36. Hassounah, N. B. *et al.* Identification and characterization of an alternative cancer-derived PD-L1 splice variant. *Cancer Immunology, Immunotherapy* **68**, 407–420 (2019).
37. Mahoney, K. M. *et al.* A secreted PD-L1 splice variant that covalently dimerizes and mediates immunosuppression. *Cancer Immunology, Immunotherapy* **68**, 421–432 (2019).
38. Hodi, F. S. *et al.* Improved Survival with Ipilimumab in Patients with Metastatic Melanoma. *New England Journal of Medicine* **363**, 711–723 (2010).
39. Schadendorf, D. *et al.* Pooled Analysis of Long-Term Survival Data From Phase II and Phase III Trials of Ipilimumab in Unresectable or Metastatic Melanoma. *Journal of Clinical Oncology* **33**, 1889–1894 (2015).
40. Kwon, E. D. *et al.* Ipilimumab versus placebo after radiotherapy in patients with metastatic castration-resistant prostate cancer that had progressed after docetaxel chemotherapy (CA184-043): a multicentre, randomised, double-blind, phase 3 trial. *Lancet Oncol* **15**, 700–712 (2014).
41. Reck, M. *et al.* Ipilimumab in combination with paclitaxel and carboplatin as first-line therapy in extensive-disease-small-cell lung cancer: results from a randomized, double-blind, multicenter phase 2 trial†. *Annals of Oncology* **24**, 75–83 (2013).
42. Robert, C. *et al.* Nivolumab in Previously Untreated Melanoma without BRAF Mutation. *New England Journal of Medicine* **372**, 320–330 (2014).
43. Borghaei, H. *et al.* Nivolumab versus Docetaxel in Advanced Nonsquamous Non–Small-Cell Lung Cancer. *New England Journal of Medicine* **373**, 1627–1639 (2015).
44. Reck, M. *et al.* Pembrolizumab versus Chemotherapy for PD-L1–Positive Non–Small-Cell Lung Cancer. *New England Journal of Medicine* **375**, 1823–1833 (2016).
45. Rittmeyer, A. *et al.* Atezolizumab versus docetaxel in patients with previously treated non-small-cell lung cancer (OAK): a phase 3, open-label, multicentre randomised controlled trial. *The Lancet* **389**, 255–265 (2017).
46. Nishijima, T. F., Shachar, S. S., Nyrop, K. A. & Muss, H. B. Safety and Tolerability of PD-1/PD-L1 Inhibitors Compared with Chemotherapy in Patients with Advanced Cancer: A Meta-Analysis. Oncologist 22, 470–479 (2017).
47. Michot, J. M. *et al.* Immune-related adverse events with immune checkpoint blockade: a comprehensive review. *Eur J Cancer* **54**, 139–148 (2016).
48. Naidoo, J. *et al.* Toxicities of the anti-PD-1 and anti-PD-L1 immune checkpoint antibodies. *Ann Oncol* **26**, 2375–2391 (2015).
49. Kumar, V. *et al.* Current Diagnosis and Management of Immune Related Adverse Events (irAEs) Induced by Immune Checkpoint Inhibitor Therapy. *Front Pharmacol* **8**, (2017).
50. Lipson, E. J. *et al.* Durable Cancer Regression Off-Treatment and Effective

Reinduction Therapy with an Anti-PD-1 Antibody. *Clinical Cancer Research* **19**, 462–468 (2013).

51. Anagnostou, V. *et al.* Evolution of Neoantigen Landscape during Immune Checkpoint Blockade in Non–Small Cell Lung Cancer. *Cancer Discov* **7**, 264–276 (2017).
52. Tumeh, P. C. *et al.* PD-1 blockade induces responses by inhibiting adaptive immune resistance. *Nature* **515**, 568–571 (2014).
53. Weber, R. *et al.* Myeloid-Derived Suppressor Cells Hinder the Anti-Cancer Activity of Immune Checkpoint Inhibitors. *Front Immunol* **9**, (2018).
54. Kwan, B. *et al.* 783 SGN-PDL1V, a novel, investigational PD-L1-directed antibody-drug conjugate for the treatment of solid tumors. *J Immunother Cancer* **9**, A818 (2021).
55. Roopenian, D. C. & Akilesh, S. FcRn: the neonatal Fc receptor comes of age. *Nat Rev Immunol* **7**, 715–725 (2007).
56. Couey, M. A. *et al.* Delayed immune-related events (DIRE) after discontinuation of immunotherapy: diagnostic hazard of autoimmunity at a distance. *J Immunother Cancer* **7**, (2019).
57. Lee, C. M. & Tannock, I. F. The distribution of the therapeutic monoclonal antibodies cetuximab and trastuzumab within solid tumors. *BMC Cancer* **10**, 255 (2010).
58. Spadiut, O., Capone, S., Krainer, F., Glieder, A. & Herwig, C. Microbials for the production of monoclonal antibodies and antibody fragments. *Trends Biotechnol* **32**, 54–60 (2014).
59. Zak, K. M. *et al.* Structure of the Complex of Human Programmed Death 1, PD-1, and Its Ligand PD-L1. *Structure* **23**, 2341–2348 (2015).
60. Bakail, M. & Ochsenbein, F. Targeting protein–protein interactions, a wide open field for drug design. *Comptes Rendus Chimie* **19**, 19–27 (2016).
61. Tan, S. *et al.* An unexpected N-terminal loop in PD-1 dominates binding by nivolumab. *Nat Commun* **8**, 14369 (2017).
62. S, C. L. & XIAOFAN, Z. COMPOUNDS USEFUL AS IMMUNOMODULATORS. (2015).
63. Zak, K. M. *et al.* Structural basis for small molecule targeting of the programmed death ligand 1 (PD-L1). *Oncotarget* **7**, 30323–30335 (2016).
64. Deng, J. *et al.* Small Molecule Inhibitors of Programmed Cell Death Ligand 1 (PD-L1): A Patent Review (2019–2021). *Expert Opinion on Therapeutic Patents* vol. 32 575–589 Preprint at https://doi.org/10.1080/13543776.2022.2045276 (2022).
65. Guzik, K. *et al.* Small-Molecule Inhibitors of the Programmed Cell Death-1/Programmed Death-Ligand 1 (PD-1/PD-L1) Interaction via Transiently Induced Protein States and Dimerization of PD-L1. *J Med Chem* **60**, 5857–5867 (2017).
66. Basu, S. *et al.* Design, Synthesis, Evaluation, and Structural Studies of C2-Symmetric Small Molecule Inhibitors of Programmed Cell Death-1/Programmed Death-Ligand 1 Protein–Protein Interaction. *J Med Chem* **62**, 7250–7263 (2019).
67. Kawashita, S. *et al.* Symmetry-based ligand design and evaluation of small molecule inhibitors of programmed cell death-1/programmed death-ligand 1 interaction. *Bioorg Med Chem Lett* **29**, 2464–2467 (2019).
68. Muszak, D. *et al.* Terphenyl-Based Small-Molecule Inhibitors of Programmed Cell

Death-1/Programmed Death-Ligand 1 Protein–Protein Interaction. *J Med Chem* **64**, 11614–11636 (2021).

69. Qin, M. *et al.* Discovery of [1,2,4]Triazolo[4,3-a]pyridines as Potent Inhibitors Targeting the Programmed Cell Death-1/Programmed Cell Death-Ligand 1 Interaction. *J Med Chem* **62**, 4703–4715 (2019).
70. Acúrcio, R. C. *et al.* Therapeutic targeting of PD-1/PD-L1 blockade by novel small-molecule inhibitors recruits cytotoxic T cells into solid tumor microenvironment. *J Immunother Cancer* **10**, e004695 (2022).
71. Sasikumar, P. G. *et al.* PD-1 derived CA-170 is an oral immune checkpoint inhibitor that exhibits preclinical anti-tumor efficacy. *Commun Biol* **4**, 699 (2021).
72. Skalniak, L. *et al. Small-molecule inhibitors of PD-1/PD-L1 immune checkpoint alleviate the PD-L1-induced exhaustion of T-cells*. *Oncotarget* vol. 8 www.impactjournals.com/oncotarget/ (2017).
73. MATTHEW, M. M. *et al.* MACROCYCLIC INHIBITORS OF THE PD-1/PD-L1 AND CD80(B7-1)/PD-L1 PROTEIN/PROTEIN INTERACTIONS. (2014).
74. Magiera-Mularz, K. *et al.* Bioactive Macrocyclic Inhibitors of the PD-1/PD-L1 Immune Checkpoint. *Angewandte Chemie International Edition* **56**, 13732–13735 (2017).
75. Magiera-Mularz, K. *et al.* Macrocyclic Peptide Inhibitor of PD-1/PD-L1 Immune Checkpoint. *Adv Ther (Weinh)* **4**, 2000195 (2021).
76. Chang, H.-N. *et al.* Blocking of the PD-1/PD-L1 Interaction by a D -Peptide Antagonist for Cancer Immunotherapy. *Angewandte Chemie* **127**, 11926–11930 (2015).
77. Shin, J., Phelan, P. J., Gjoerup, O., Bachovchin, W. & Bullock, P. A. Characterization of a single chain variable fragment of nivolumab that targets PD-1 and blocks PD-L1 binding. *Protein Expr Purif* **177**, 105766 (2021).
78. Zhang, F. *et al.* Structural basis of a novel PD-L1 nanobody for immune checkpoint blockade. *Cell Discov* **3**, 17004 (2017).
79. Maute, R. L. *et al.* Engineering high-affinity PD-1 variants for optimized immunotherapy and immuno-PET imaging. *Proc Natl Acad Sci U S A* **112**, E6506–E6514 (2015).
80. Foord, E. *et al.* Profound Functional Suppression of Tumor-Infiltrating T-Cells in Ovarian Cancer Patients Can Be Reversed Using PD-1-Blocking Antibodies or DARPin® Proteins. *J Immunol Res* **2020**, 7375947 (2020).
81. Grindel, B. J. *et al.* Directed Evolution of PD-L1-Targeted Affibodies by mRNA Display. *ACS Chem Biol* **17**, 1543–1555 (2022).
82. Lázár-Molnár, E. *et al.* Structure-guided development of a high-affinity human Programmed Cell Death-1: Implications for tumor immunotherapy. *EBioMedicine* **17**, 30–44 (2017).
83. Ganesan, A. *et al.* Comprehensive in vitro characterization of PD-L1 small molecule inhibitors. *Sci Rep* **9**, 12392 (2019).

Chapter II | Development of a Non-antibody Protein Inhibitor

2.1. Introduction

The PD-L1 binding region within the PD-1, immunoglobulin variable-like domain (IgV-like domain, hereafter soluble PD-1), is an ideal protein scaffold for designing the protein ICI. First, as a native PD-L1 binder, soluble PD-1 has lower immunogenicity than other protein scaffold and have shown a therapeutic effect in many reported papers[1]. Besides, the molecular weight of soluble PD-1 is 10-times smaller than antibodies, which would theoretically have a better tumor tissue penetration property. Moreover, soluble PD-1 could be obtained on large-scale through the *E. coli* expression system, which is cheaper and more efficient than the mammalian cell expression system used in antibody production.

The wild-type PD-1 (WT-PD-1) has a moderate binding affinity with PD-L1 at around 1 μM[2], which is about 1000-times weaker than the current antibody and not effective enough to be directly used as an inhibitor. Therefore, affinity maturation is necessary to enhance its affinity by inducing mutagenesis. However, current high-affinity PD-1 variants were developed from a random selection process, which inevitably introduced many unnecessary mutations and raised its immunogenicity. For example, a high-affinity PD-1 variant called HAC has 10 mutations, which means about 10% of residues have been changed[3]. To increase the affinity of PD-1 while suppressing the number of mutations, accurate affinity maturation is desired.

In 2015, Zak et. al reported a high-resolution X-ray crystal structure for the complex of human PD-1/PD-L1[4], providing the opportunity to perform the *in silico* mutagenesis for determining the point mutation candidates that could have a higher binding affinity for the PD-L1. Since the current *in silico* mutagenesis result is not accurate enough, additional experimental verification is necessary to refine the candidates. Traditional verification needs to first produce proteins through the *E. coli* expression system and purify the proteins. PD-1 is expressed as the insoluble inclusion body within *E. coli* and needs the refolding process to solubilize the protein, which makes it even more time-consuming to purify multiple candidates. Besides, verifications are usually performed by using kinetics assay, which is accurate but has a low throughput. In 2016, researchers from the Promega company developed a split luciferase assay, which could produce the proteins within the cell without purification and accurately measured the protein-protein interactions via luminescence.[5] In this chapter, the combination of the *in silico* mutagenesis with the in-cell verification achieved an accurate affinity maturation of soluble PD-1.

2.2. Material & Methods

2.2.1. Materials

The sequence of soluble human PD-1 IgV-like domain (E33-E150) was retrieved from Uniprot with the entry of Q15116. Unpaired cysteine of C93 was substituted with serine to enhance its stability. The sequence of the PD-1 binding domain of PD-L1 (F19-Y134) was retrieved from Uniprot with the entry of Q9NZQ7. Eurofins (Japan) synthesized the DNA coding sequence of PD-1 and PD-L1 with codons optimized for *E. coli* expression. All the reagents used were biochemical research grade. Hela cells were obtained from the Japanese Collection of Research Bioresource (JCRB).

2.2.2. *In silico* mutagenesis

The human PD-1/PD-L1 complex was imported into ICM-pro software (ver. 3.8) from the PDB ID of 4ZQK. Based on the distance, residues of PD-1 which interacts with PD-L1 were automatically determined by the software (Y68, M70, S73, Q75-K78, G124, I126, K131-E136). For each of the residues, binding free energy was calculated using the ICM-pro build-in force filed for the mutant PD-1/PD-L1 (ΔG_{bind}^{mut}) as well as the WT-PD-1/PD-L1 (ΔG_{bind}^{wt}). The effect of mutagenesis was described by the difference between the before and after mutagenesis ($\Delta\Delta G_{\mathrm{bind}} = \Delta G_{bind}^{mut} - \Delta G_{bind}^{wt}$). Point mutations with negative $\Delta\Delta G_{\mathrm{bind}}$ was selected as candidates since they had better thermodynamic stability[6].

2.2.3. Luciferase-based in-cell verification

WT-PD-1 was inserted into pBiT1.1-C [TK/LgBiT] vector (obtained from Promega, USA) using In-Fusion® HD Cloning Kit (TaKaRa, Japan) for constructing the expression vector for the PD-1-LgBiT. A PCR-based mutagenesis was performed for PD-1-LgBiT using the primer design described in PrimeSTAR Mutagenesis Basal Kit (TaKaRa, Japan) to create the expression vector for each *in silico* candidates to give the PD-1 (candidates)-LgBiT. PD-L1 was inserted into pBiT2.1-N [TK/SmBiT] vector (obtained from Promega, USA) to construct the expression vector of SmBiT-PD-L1. Vector of SmBiT-PD-L1 was co-transfected with PD-1 (WT or candidates)-LgBiT into Hela cell, which was preincubated for 20 h in the 96-well plates (B&W Isoplate, PerkinElmer, USA). The transfection was performed using FuGENE® HD reagent (Promega, USA). After 24 h incubation to express the fusion protein within the cells, DMEM medium (10% (v/v) FBS and 1% antibiotics contained, Gibco, USA) was replaced by Opti-MEM (Reduced Serum Medium, no phenol red, Gibco, USA) and Nano-Glo® live cell reagent (Promega, USA) was added into each well. The luminescence of each well of cells was measured by a plate reader (EnSpire®, PerkinElmer, USA) after 10 mins of incubation at room temperate.

2.2.4. PD-1 expression and purification

The expression vector of WT-PD-1 or 2-PD-1 was constructed by inserting their DNA coding sequences into the pET21b(+) vector (Novagen, Germany) using In-Fusion® HD Cloning Kit (TaKaRa, Japan). The expression vector was used for PD-1 expression. The process for the protein expression, refolding and purification was performed by following the previously reported protocol[7]. Further purification using the size exclusion chromatography (HiLoad 16/600 Superdex 200 pg column, Cytiva, Japan) was performed for the proteins used in the T cell reactivation bioassay. The concentration of purified protein is determined by using the NanoDrop™ one (Thermo Fisher Scientific, USA) and aliquots were stored at − 80 °C for further experiment.

2.2.5. Kinetics binding analysis

The purified WT-PD-1 or 2-PD-1 was biotinylated with NHS-dPEG®24-biotin (Quanta BioDesign). BLItz system (Sartorius, Germany) was used for the kinetics binding analysis[8]. Biotinylated WT-PD-1 or 2-PD-1 was dissolved into the kinetics buffer (10 mM HEPES, 5 mg/mL bovine serum albumin, 0.01% (v/v) Tween 20, 150 mM NaCl, pH 7.4) at 100 nM and immobilized onto streptavidin biosensors (Sartorius, Germany). 200 s was set for the detection of an association between PD-L1 and 300s was set for the detection of a dissociation. The Signal was normalized with a non-PD-L1 immobilized kinetics binding curve. A global fitting function pre-installed in the BLItz analysis software was used to fit and calculate the association and dissociation constants.

2.2.6. PD-1/PD-L1 inhibitory assay

The His tag of purified WT-PD-1 and 2-PD-1 is cleaved by thrombin (MP Biomedicals, Japan) and purified by His Spintrap (Cytiva, Japan). AlphaLISA® human PD-1 and PD-L1 binding kit were used for performing the inhibitory assay. Samples are dissolved in the assay buffer (provided within the Kit) to give a starting stock and serial dilutions were prepared from the stock using the assay buffer. 6.67 nM of PD-L1-His tag, 6.67 nM of biotinylated PD-1, 26.67 µg/mL of streptavidin Donor beads, 13.33 µg/mL of anti-His tag Acceptor beads (all provided within the Kit) were dissolved in the assay buffer and added to 384-well plate (ProxiPlate, PerkinElmer, USA) at 6 µL/well under dark environment. Each prepared diluted sample was added to a 384-well plate at 2 µL/well and incubated at room temperature for 90 mins under a dark environment. The AlphaLISA signal of each well was measured using a plate reader (EnSpire®, PerkinElmer, USA). GraphPad Prism was used for fitting the plot with the "inhibitors vs. response – variable slope function" to deduce the IC_{50} as well as the confidence interval.

2.2.7. T cell reactivation bioassay

T cell reactivation assay was performed using the PD-1/PD-L1 blockade bioassay kit (Promega, USA). 100 µL of tumor mimic PD-L1 expressing CHO-K1 cells was suspended in the Ham's F-12 culture medium (provided in the kit) and seeded in the wells of 96-well plate (B&W Isoplate, PerkinElmer, USA) at 125,000 cells/100 µL. After overnight incubation at 37 °C, the culture medium was removed. serial dilutions of size exclusion chromatography purified WT-PD-1 and 2-PD-1 as well as the commercial antibody of nivolumab were prepared in the RPMI 1640 culture medium (1% FBS, provided within Kit) and added to wells at 40 µL/wells. At the same time, luciferase reporter containing Jurkat T cell (provided within the Kit) was suspended in the RPMI 1640 culture medium (1% FBS, provided within Kit) at 50,000 cells/40 µL and added to wells at 40 µL/well. After incubation under 37 °C for 6 h, Bio-Glo reagent was added at 80 µL/well and luminescence was measured using a plate reader (EnSpire®, PerkinElmer, USA). Graphpad Prism was used for fitting the plot using "agonist vs. response" functions to deduce the EC_{50} as well as a confidence interval.

2.3. Results

2.3.1. Development of the high-affinity PD-1 variant.

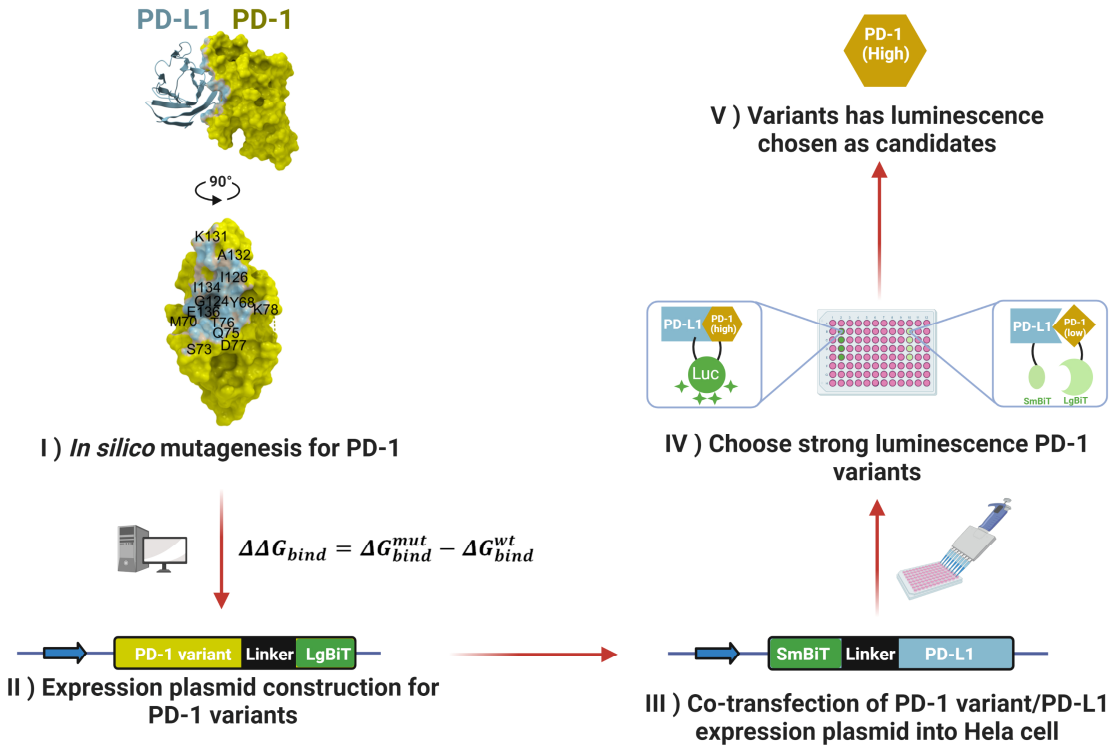

Figure 2.3.1 Schematic illustration for the development method of PD-1 variants. *In silico* mutagenesis was first performed to determine the potent high-affinity point mutation candidates, using the criteria of the decreased binding free energy after mutation. Next, to verify the candidates, the expression vector of PD-1 (variants)-LgBiT and SmBiT-PD-L1 were constructed and co-transfected into the cell. As the PD-1/PD-L1 interaction would reconstitute the LgBiT/SmBiT into the functional luciferase, the luminescence could reflect the affinity of PD-1 variants with PD-L1. This picture is reused from the reported paper with the permission from ACS Chem. Biol. 2021, 16, 2, 316–323, Publication Date: January 15, 2021, https://doi.org/10.1021/acschembio.0c00817, Copyright © 2021 American Chemical Society.

As shown in the **Figure 2.3.1**, the *in silico* mutagenesis and in-cell luciferase-based interaction assay was used to perform the accurate affinity maturation. First, based on the human PD-1/PD-L1 crystal structure, PD-L1-interacting residues (indicated in **Figure 2.3.1** as black characters in the PD-1 structure) within the PD-1 were each mutated into other residues and their difference of binding free energy was calculated. As shown in **Table 2.3.1**, 18 candidates were chosen as the candidates from the *in silico* calculation results. Next, PD-1 candidates were inserted into the expression vector and could be expressed as the fusion protein of PD-1(variants)-LgBiT, where LgBiT is the large subunit of the split NanoLuc luciferase[5]. On the other hand, PD-L1 is expressed into the other expression vector and could

be expressed as the fusion protein of SmBiT-PD-L1, where the SmBiT is the small subunit of the split NanoLuc luciferase. The LgBiT and SmBiT originally have a very weak interaction (about 100-times weaker than the PD-1/PD-L1 interaction) and therefore could only be reconstituted into the complete luciferase of NanoLuc under the PD-1/PD-L1 interaction. Therefore, after the co-transfection of two types of vectors into the cell, the luminescence intensity would correspond to the binding affinity between PD-1 variants. As shown in **Figure 2.3.2.A**, A132V and T76Y showed higher luminescence than the WT-PD-1 and therefore determined as final single mutants. Interestingly, as shown in **Figure 2.3.2.B** their double mutant called as 2-PD-1 showed an even higher luminescence than a simple addition, suggesting the exist of the synergic effect between these two residues.

Table 2.3.1 Representative in silico mutagenesis results.

Res Mut	M70	S73	T76	D77	K78	A132
G	0.759907	0.110184	2.596519	0.707039	3.399946	1.438829
A	0.631900	0.020893	1.382185	0.624219	2.480258	0
V	0.796507	0.108179	0.656440	0.699576	1.731257	**-0.880712**
L	0.625057	0.442064	1.429457	0.715832	1.102812	**-0.501436**
I	0.761945	0.079876	1.720385	0.635723	1.108718	0.255083
P	0.677691	N.D.	0.478055	N.D.	2.083567	4.707685
C	1.126367	0.797384	0.745068	1.228615	2.657524	0.841424
M	0	0.958463	2.667781	0.907181	1.997815	2.204977
S	1.011587	0	0.434279	0.884683	2.751947	0.229906
T	1.019496	0.126606	0	0.798657	2.016041	-0.402220
F	0.767503	**-0.816744**	0.811271	0.927381	**-0.245260**	1.726560
Y	0.787289	**-0.733037**	**-0.772174**	0.824161	0.937286	3.162433
W	0.988866	**-2.059363**	1.155773	1.639607	2.729647	5.835450
N	1.031267	0.439857	**-1.470575**	0.620404	2.433643	-0.046061
Q	**-0.424842**	0.088273	1.728764	0.248273	1.313873	0.809622
D	1.200540	-0.447202	**-4.122689**	0	3.348081	1.900862
E	0.291855	**-0.230489**	**-7.040167**	0.922555	2.916939	2.732248
H	0.757014	**-0.336588**	-0.535852	0.456231	2.819032	0.214480
K	**-0.099451**	0.173693	5.538386	0.387070	0	1.103606
R	**-2.000211**	**-0.284826**	6.283364	**-0.725368**	0.437192	**-1.150459**

Representative residues showing a decreased binding free energy were listed in the first row in the table, and their mutated residues were listed in the first column. The calculated difference of binding free energy was summarized in the table and the chosen candidates were emphasized in red color and bold. N.D. indicates no data as the calculation failed. Unit: kcal/mol. Other residues indicated in 2.2.1 or Figure 2.3.1 were also calculated but not listed here for they did not show the negative binding free energy results. This table is reused from the reported paper with the permission from ACS Chem. Biol. 2021, 16, 2, 316–323, Publication Date: January 15, 2021, https://doi.org/10.1021/acschembio.0c00817, Copyright © 2021 American Chemical Society.

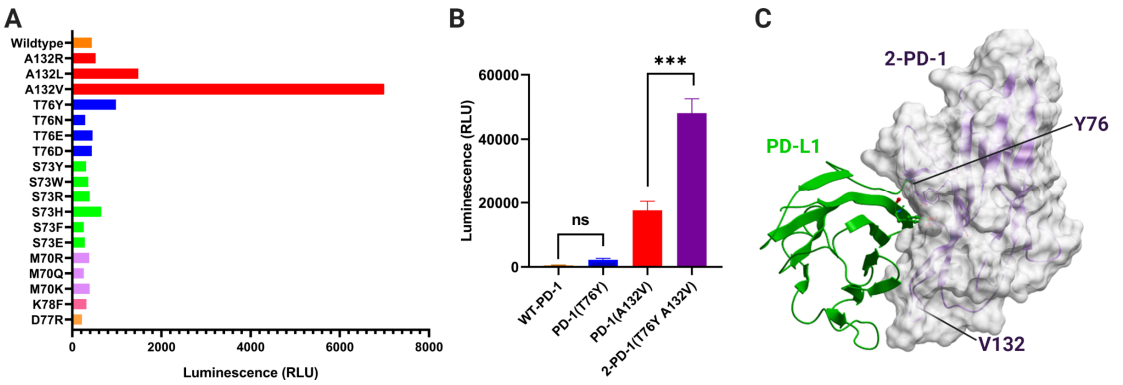

Figure 2.3.2. Luciferase-based in-cell verification results. (A) Luminescence from all *in silico* candidates and WT-PD-1. (B) Luminescence of the selected single mutant of PD-1 (T76Y) and PD-1 (A132V) as well as their double mutant of 2-PD-1. The experiment was conducted in quadruplicates. Turkey's test was performed and *** indicates the $p<0.001$. (C) Notification of the position for the two mutations within the 2-PD-1. This picture is reused from the reported paper with the permission from ACS Chem. Biol. 2021, 16, 2, 316–323, Publication Date: January 15, 2021, https://doi.org/10.1021/acschembio.0c00817, Copyright © 2021 American Chemical Society.

2.3.2. Kinetics binding analysis

Although the luminescence from the luciferase-based in-cell protein assay was correlated with the binding affinity with the PD-1 variants and PD-L1, other elements such as expression amount may also interfere with the luminescence intensity. Therefore, a more accurate kinetics measurement is needed to compare the binding affinity of 2-PD-1 with WT-PD-1. As shown in **Figure 2.3.3** and **Table 2.3.2**, 2-PD-1 showed about 10-times higher association rate constant and about 10-times lower dissociation rate constant than the WT-PD-1, which together contributed to about 100-times lower equilibrium rate constant than the WT-PD-1. This kinetic result was well consisting with the luciferase-based assay, proving that the increase of luminescence intensity of 2-PD-1 is originated from its high affinity.

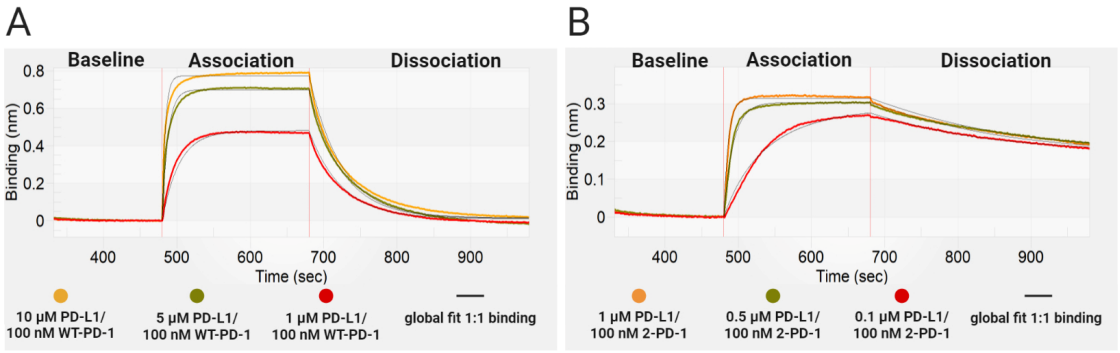

Figure 2.3.3. Kinetics binding curve of (A) WT-PD-1 and (B) 2-PD-1 with different concentrations of PD-L1. The global fitted curves for all three PD-L1 concentrations are depicted as thin black line. This picture is reused from the reported paper with the permission from ACS Chem. Biol. 2021, 16, 2, 316–323, Publication Date: January 15, 2021, https://doi.org/10.1021/acschembio.0c00817, Copyright © 2021 American Chemical Society.

Table 2.3.2 Kinetics parameters deduced from the global fitting of the kinetics binding curves.

Samples	K_D (M)	k_a ($M^{-1}s^{-1}$)	k_d (s^{-1})
WT-PD-1	$1.04\pm0.02 \times 10^{-6}$	$2.11\pm0.03 \times 10^{4}$	$2.20\pm0.02 \times 10^{-2}$
2-PD-1	$1.45\pm0.03 \times 10^{-8}$	$1.54\pm0.01 \times 10^{5}$	$2.23\pm0.02 \times 10^{-3}$

K_D: Equilibrium dissociation constant; k_a: Association rate constant; k_d: Dissociation rate constant. This table is reused from the reported paper with the permission from ACS Chem. Biol. 2021, 16, 2, 316–323, Publication Date: January 15, 2021, https://doi.org/10.1021/acschembio.0c00817, Copyright © 2021 American Chemical Society.

2.3.3. PD-1/PD-L1 inhibitory assay

Although 2-PD-1 showed a higher affinity towards the PD-L1, it may bind to the non-PD-1-binding epitope of PD-L1 that could not provide the competitive inhibitory effect. To directly evaluate the inhibitory effect of the 2-PD-1 for blocking the PD-1/PD-L1 interaction, an inhibitory assay was performed using the AlphaLISA techonology[9] (**Figure 2.3.4**). As shown in **Figure 2.3.4** and **Table 2.3.3**, both 2-PD-1 and WT-PD-1 could fully inhibit the PD-1/PD-L1 interaction as commercial antibody of Nivolumab and 2-PD-1 has about 30-times smaller IC_{50} than that of the WT-PD-1. On the other hand, the IC_{50} of 2-PD-1 was about 10-fold larger than that of the nivolumab.

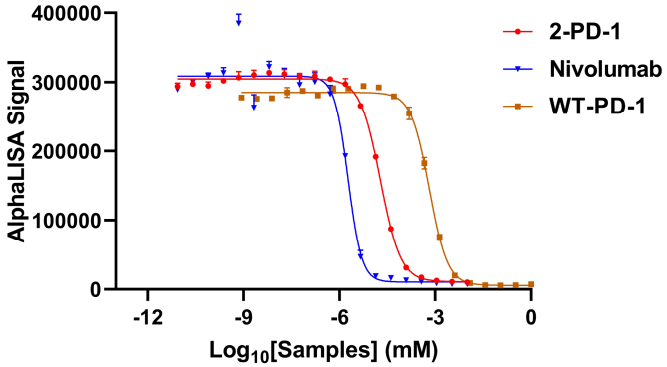

Figure 2.3.4 PD-1/PD-L1 inhibitory assay using the AlphaLISA technology. Dose-dependent inhibition curve for three samples. Each plot indicated the triplicate of the experiment. This figure is reused from the reported with the permission from ACS Chem. Biol. 2021, 16, 2, 316–323, Publication Date: January 15, 2021, https://doi.org/10.1021/acschembio.0c00817, Copyright © 2021 American Chemical Society.

Table 2.3.3 IC_{50} deduced from the fitting of dose-dependent inhibition curve.

Samples	IC_{50} (nM)	95% CI of IC_{50} (nM)
WT-PD-1	6.52×10^2	6.51×10^2 to 6.92×10^2
2-PD-1	1.92×10	1.79×10 to 2.04×10
Nivolumab	1.86	1.57 to 2.21

IC_{50}: Half maximal inhibitory concentration; CI: Confidence interval. This table is reused from the reported paper with the permission from ACS Chem. Biol. 2021, 16, 2, 316–323, Publication Date: January 15, 2021, https://doi.org/10.1021/acschembio.0c00817, Copyright © 2021 American Chemical Society.

2.3.4. T-cell reactivation assay

Although 2-PD-1 could fully block the PD-1/PD-L1 interaction at the protein-protein interaction level, it may fail to reactive the T-cell due to cytotoxicity, which is a common phenomenon that has been observed for many small molecular PD-1/PD-L1 inhibitors[10]. Therefore, a cell experiment was conducted to evaluate the bioactivity as well as cytotoxicity of 2-PD-1 (**Figure 2.3.5**). As shown in **Figure 2.3.5** and **Table 2.3.4**, 2-PD-1 could fully reactive the T cell as commercial antibody of nivolumab and the full activation effect was maintained at the about 30 μM, indicating 2-PD-1 had a much lower cytotoxicity than small molecular inhibitors. 2-PD-1 had 100-times smaller EC_{50} than that of the WT-PD-1, while nivolumab had 50-times smaller EC_{50} than nivolumab.

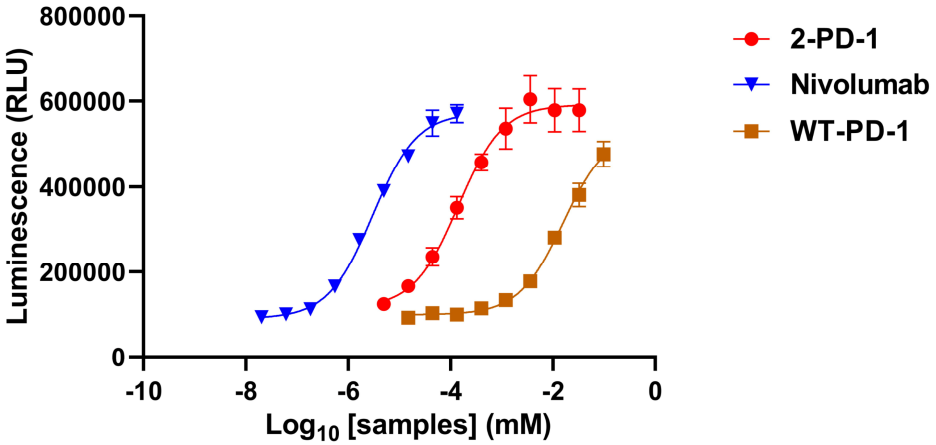

Figure 2.3.5. T cell reactivation assay. Dose-dependent reactivation curve for the three samples. Each plot indicated as the triplicate of the experiment. This figure is reused from the reported with the permission from ACS Chem. Biol. 2021, 16, 2, 316–323, Publication Date: January 15, 2021, https://doi.org/10.1021/acschembio.0c00817, Copyright © 2021 American Chemical Society.

Table 2.3.4. EC50 deduced from the fitting of dose-dependent reactivation curve.

Samples	EC_{50} (nM)	95% CI of EC_{50} (nM)
WT-PD-1	1.60×10^4	1.27×10^4 to 2.02×10^4
2-PD-1	1.40×10^2	9.71×10 to 2.01×10^2
Nivolumab	2.98	2.55 to 3.48

EC_{50}: Half maximum effective concentration. CI: Confidence interval.

2.4. Discussion and conclusion

In this Chapter, the development of the protein ICIs was described. The development methods combined the high-throughput property of *in silico* mutagenesis and the high accuracy and convenience of in-cell verification, successfully achieving the accurate affinity maturation of WT-PD-1 to give the 2-PD-1. 2-PD-1 maintained the advantage of WT-PD-1, such as: small molecular size, low immunogenicity, low cytotoxicity, and easy productivity; while its activity including: PD-L1 binding affinity, PD-1/PD-L1 inhibitory effect, and T cell reactivation bioactivity, was significantly improved than those of the WT-PD-1. As the interaction of PD-1/PD-L1 is mainly composed by the hydrophobic interaction, the T76Y mutation and A132V mutation both had an increased hydrophobicity and thus is reasonable to provide a higher affinity than WT-PD-1. However, 2-PD-1 was still less potent when compared to the commercial antibody of nivolumab. Nivolumab belongs to the IgG, which is bivalent as it has double antigen-binding sites, contributing to an accumulated higher binding strength than the monovalent binders and generally called as the avidity or multivalent effect[11]. Indeed, the monovalent single-chain variable fragment of nivolumab has a reported IC_{50} at 26 nM, which is weaker than the bivalent nivolumab and is comparable as 2-PD-1. On the other hand, a monovalent DAPRin® protein scaffold-based protein inhibitor originally had a T cell reactivity at the EC_{50} of 129.8 nM, which is similar as 2-PD-1. While a bivalent version of DAPR in inhibitor showed a EC_{50} at 4.73 nM, which is comparable to the nivolumab, indicating that the activity of 2-PD-1 could also be enhanced in similar strategy to become an even more promising protein ICIs.

Reference

1. Khan, M., Zhao, Z., Arooj, S., Fu, Y. & Liao, G. Soluble PD-1: Predictive, Prognostic, and Therapeutic Value for Cancer Immunotherapy. *Front Immunol* **11**, (2020).
2. Lázár-Molnár, E. *et al.* Structure-guided development of a high-affinity human Programmed Cell Death-1: Implications for tumor immunotherapy. *EBioMedicine* **17**, 30–44 (2017).
3. Maute, R. L. *et al.* Engineering high-affinity PD-1 variants for optimized immunotherapy and immuno-PET imaging. *Proc Natl Acad Sci U S A* **112**, E6506–E6514 (2015).
4. Zak, K. M. *et al.* Structure of the Complex of Human Programmed Death 1, PD-1, and Its Ligand PD-L1. *Structure* **23**, 2341–2348 (2015).
5. Dixon, A. S. *et al.* NanoLuc Complementation Reporter Optimized for Accurate Measurement of Protein Interactions in Cells. *ACS Chem Biol* **11**, 400–408 (2016).
6. Abagyan, R., Totrov, M. & Kuznetsov, D. ICM—A new method for protein modeling and design: Applications to docking and structure prediction from the distorted native conformation. *J Comput Chem* **15**, 488–506 (1994).
7. Dharmatti, R. *et al.* Escherichia coli expression, purification, and refolding of human folate receptor α (hFRα) and β (hFRβ). *Protein Expr Purif* **149**, 17–22 (2018).
8. Shah, N. B. & Duncan, T. M. Bio-layer interferometry for measuring kinetics of protein-protein interactions and allosteric ligand effects. *J Vis Exp* e51383–e51383 (2014) doi:10.3791/51383.
9. Beaudet, L. *et al.* AlphaLISA immunoassays: the no-wash alternative to ELISAs for research and drug discovery. *Nat Methods* **5**, an8–an9 (2008).
10. Ganesan, A. *et al.* Comprehensive in vitro characterization of PD-L1 small molecule inhibitors. *Sci Rep* **9**, 12392 (2019).
11. Oostindie, S. C., Lazar, G. A., Schuurman, J. & Parren, P. W. H. I. Avidity in antibody effector functions and biotherapeutic drug design. *Nature Reviews Drug Discovery* vol. 21 715–735 Preprint at https://doi.org/10.1038/s41573-022-00501-8 (2022).

Chapter III | Development of Small Molecular Drug Conjugated Peptide Inhibitor

3.1. Introduction

To develop SMI-incorporated peptide (SMI-peptide) ICIs, the main task is to determine a suitable peptide sequence that could exhibit a synergic effect with SMI. However, as introduced in the Chapter1, the PD-1/PD-L1 complex is a difficult target for computational drug design due to their interaction surface being huge and flat. Therefore, an experimental selection method was used to determine the suitable peptide sequence.

In 2018, Frances H. Arnold, George P. Smith, and Sir Gregory P. Winter won the Nobel prize in chemistry because of their contribution to directed evolution [1]. Directed evolution links each phenotype (protein) with its genotype (coding sequence) to achieve high throughput screening. Specifically, George P. Smith developed the phage display, which has been successfully used for various antibody development, including the FDA-approved anti-PD-L1 antibody of Atezolizumab[2]. In phage display, each bacteriophage expresses a certain peptide outside on its surface and maintains the peptide coding sequence inside. After selection against the immobilized target, the amino acid sequence of the target-binding peptide could be decoded by reading its DNA sequence. However, bacteriophage does not have ribosomes and needs to infect and utilize *E. coli* for peptide synthesis, which is not applicable for screening the peptides which are toxic or composed of cell-membrane nonpermeable amino acids.

Besides the phage display, some display methods use cell-free protein synthesis to *in vitro* synthesize the peptide, such as the ribosome display [3]. In the ribosome display, the peptide coding sequence is designed to contain a ribosome-stalling sequence [4] after the peptide coding region and remove the stop codon [3]. As a result, during the translation, each ribosome synthesizes a certain peptide and then is stalled and stabilized to keep holding the peptide coding mRNA, forming the peptide/ribosome/mRNA complex (PRM). Compared to the phage display, the ribosome display directly selects each PRM and thus holds a larger library size of 10^{13}.

One of the challenges in the current ribosome display technique is the difficulty of incorporating noncanonical amino acid (ncAA) into peptide [5]. In natural protein biosynthesis, the amino acid is first charged onto the tRNA through the aminoacyl-tRNA synthetase (aaRS). Next, the charged-tRNA recognizes its corresponding codon and accommodates itself into the ribosome, where the amino acid is transferred from the tRNA to the extended peptide under the catalyzation of the ribosome. Some of the ncAA could be incorporated into the peptides in the same way as canonical amino acids, such as exo BCN-L-Lysine [6]. However, other ncAA (i.e., amino acids modified with SMI) instead may be too large that the peptidyl

transfer of ncAA within ribosome may be failed or have low efficiency. Instead, a two-step synthesis method was designed to circumvent this problem: the first step is to ribosomally incorporate a chemical-reactive ncAA to form the ncAA-peptide and the second step is to chemical selectively ligate the SMI with the ncAA-peptide to give SMI-peptide. Importantly, the SMI-peptide must ligate with its mRNA coding sequence as the SMI-PRM. However, the PRM is formed by noncovalent interaction which is very delicate and needs to be maintained in mild conditions under low temperatures [7] during the ribosome display. Therefore, the reaction between ncAA-PRM and SMI requires high selectivity, rapid kinetics, and mild reaction conditions.

The copper-free click reaction of the strain-promoted inverse electron-demand Diels-Alder cycloaddition between the strained alkenes of bicyclo[6.1.0]non-4-yne (BCN) and tetrazine meets above requirements with a reaction rate constant of round 29,000 $M^{-1}S^{-1}$ under physiological environment [8]. Furthermore, in 2012[6], Kathrin L. et.al engineered the aaRS/tRNA pair of pyrrolysyl-tRNA synthetase (PylRS)/$tRNA_{CUA}$ to achieve the high-efficient ribosomal incorporation of exo BCN-L-Lysine in responding to the amber stop codon (UAG). Therefore, SMI-peptide could be synthesized by first forming the BCN-peptide by incorporating the exo BCN-L-Lysine into the peptide and then ligating the BCN-peptide with the tetrazine-modified SMI (hereafter SMI-tetrazine).

However, the exo BCN-L-Lysine and most SMI are not water-soluble but dissolved in dimethyl sulfoxide (DMSO). It is unknown whether the SMI-peptide could form the stable SMI-PRM in the DMSO solution to finish the ribosome display. In the following sections of this Chapter, a demo selection was first designed to validate the method. Next, SMI-tetrazine was synthesized, and its structure was characterized by ^{1}H-NMR and Mass spectrometry. Furthermore, the click reactivity and PD-1/PD-L1 inhibitory activity of the SMI-tetrazine were confirmed. After completing the above confirmation, the real ribosome display was designed and performed. After the ribosome display, the candidate peptide sequence was determined from the sequencing results and verified.

3.2. Materials & Methods

3.2.1. Materials (plasmid & primer table)

PCR product	PCR template	First PCR primer (Final. Con. 0.2 μM)	Second PCR primer (Final. Con. 0.2 μM)
T7-flag	pTolA022	#13	#1499
T7-flag-amber	pTolA023	#13	#1499
T7-GFP	pTolA028	#13	#1499
T7-tRNAamber	Amber tRNA	#955	Rev_OMe_Py-tRNA
T7-dsDNA-library	T7-ssDNA mixed library	#913	#1499
TolA-SecM	pTolA010_pTolA6	#60	#909
T7-library-TolA-SecM (For 1st round real selection)	T7-library-TolA-SecM	#60	#1499
T7-library-TolA-SecM (2nd-7th round real section)	Recovered cDNA (RNA Eluted from target and prepared by RT-PCR during the real selection)	#13	#948
MiSeq NGS fragment	T7-library-TolA-SecM	#1414	#1415

Primer	Sequence
#13	TTAGCTCACCGAAAATATCATCTG
#60	CAGGAAACAGCTATGAC
#909	TGCGTCCGTCTCGGACAAAGCAGATGCTAAAGCGAAGG
#913	GCTGACCGTCTCTTGTC
#948	CGAAATTAATACGACTCACTATAGGGAGACCACAACGGTTTC
#955	ATACTAATACGACTCACTATAGGAAACCTGATCATGTAGATC
#1414	TCGTCGGCAGCGTCAGATGTGTATAAGAGACAGCGATGTGGGAGACCACAACGGTTTC
#1415	GTCTCGTGGGCTCGGAGATGTGTATAAGAGACAGCGATGTGCCGCAGCGGCTGCCTCG
#1499	CGATAATACGACTCACTATAGGGAG
Rev_OMe_Py-tRNA	TXGGGGAAACCCCGGG (X= 2'-OMe-G)

3.2.2. General Buffer recipes for ribosome display

All the reagents used in the ribosome display selection are RNase-free.

SolC: 5 mM DTT, 1.2 mM ATP, 0.8 mM CTP, 0.8 mM GTP, 0.8 mM UTP, 80 mM creatine phosphate, 50 µg/mL creatine kinase, 2% PEG8000, 68 µM 10-formyl-tetrahydrofolate, 175 µg/mL tRNA mix, 210 mM potassium glutamate, 27.5 mM ammonium acetate, 10.7 mM magnesium acetate, 1mM eighteen-amino acids, 1mM L-cysteine, 1mM L-tyrosine, 50 µg/mL T7 RNA polymerase, 50mM HEPES, pH = 7.4
Click Replace Solution: 210 mM potassium glutamate, 50 mM HEPES, 10.7 mM magnesium acetate, 27.5 mM ammonium acetate, pH = 7.4
WBT: 50 mM Tris-HCl, 140 mM NaCl, 50 mM magnesium acetate, 0.05 % Tween 20, pH = 7.2
Elution Buffer: 7 M Urea, 50 mM Tris-HCl, 140 mM NaCl, 50 mM magnesium acetate, 0.05 % Tween 20, pH = 7.2

3.2.3. Magnetic Beads preparation

Anti-FAM magnetic beads preparation

N-Hydroxysuccinimide (NHS)/ 1-Ethyl-3-[3-dimethylaminopropyl] carbodiimide hydrochloride (EDC) was used to perform the carboxyl/amine coupling between magnetic beads (Dynabeads MyOne Carboxylic acid, Thermo Fisher Scientific, USA) and anti-FAM antibody (IgG Fraction Monoclonal Mouse Anti-Fluorescein, Jackson ImmunoResearch, USA). 10 µL magnetic beads were first washed by 25 mM MES buffer (2-MorpholinoethanesµLfonic acid, pH = 6) for three times. Then, 10 µL EDC/NHS solution (50 mg/mL in 25 mM MES buffer, pH = 6) was mixed with 10 µL magnetics beads and incubated for 30 mins to pre-activate the beads. After pre-activation, beads were washed with the above MES buffer for two times and mixed with 6 µL anti-FAM antibodies. After overnight incubation at 4 °C, beads were washed by in vitro selection washing buffer (named with WBT, 50 mM Tris-HCl, 140 mM NaCl, 50 mM Magnesium acetate, and 0.05 % Tween 20) and stored at 4 °C for further use. The successful coupling between anti-FAM antibodies and magnetic beads was confirmed by immune staining with anti-mouse antibodies.

Anti-His tag magnetic beads preparation

Dynabeads™ Protein G (10003D, Thermo Fisher Scientific, USA) was first washed by PBS-T (Phosphate Buffered Saline with Tween 20, pH7.4, Takara Bio, Japan) three times and mixed with either Anti-6X His tag mAb (RM146, Abcam, UK) or Anti-DDDDK-tag mAb (FLA-1, MEDICAL & BIOLOGICAL LABORATORIES, Japan) at the volume ratio of 1 to 0.3. Besides, PBS-T was also added up to five-fold of the volume of the beads. After incubation at room temperature for 30 mins, beads were washed by WBT four times and kept at their original volume in WBT for further use. The resulting anti-His tag or anti-Flag magnetic beads were freshly prepared every time on the day of performing the real selection.

3.2.4. Random DNA library preparation for ribosome display

A Series of single-stranded DNA (ssDNA) libraries were ordered from Eurofins Genomics (Japan) and mixed with a certain ratio to give the final T7-ssDNA mixed library. Its sequence contains the T7 promoter, ribosome binding site[9], and random peptide coding sequence of 5'- ATGACAACATGT$(XXX)_5$TAG$(XXX)_5$TGTTCTTGGGACAAGAGACGGTCAGC-3'. TAG is the amber stop codon for encoding ncAA and the XXX means either VVN or NNK, where V is A, G, or C, N is A, T, G, or C, K is G or T. VVN could only encode twelve amino acids while high ratio (2/3) among them is hydrophilic. On the contrary, NNK could encode more amino acids while a low ratio (8/19) among them are hydrophilic amino acids. Therefore, the mix of VVN and NNK was aimed to ensure that displayed peptides have both hydrophilicity and diversity. The double-stranded library of T7-dsDNA-library was prepared by a single round of PCR using TaKaRa Ex Taq® (TaKaRa, Japan) and purified via gel extraction with NucleoSpin® Gel and PCR Clean-up kit (Takara Bio, Japan). On the other hand, a DNA fragment called TolA-SecM which contains a helical linker of TolA and ribosome arrest sequence of SecM was prepared by PCR using the DNA fragment of T7-dsDNA-library. TolA-SecM was cleavaged with the restriction enzyme of BsmBI (New England Biolabs, USA) and ligated with T4 DNA Ligase (Takara Bio, Japan) to give the product called T7-library-TolA-SecM. After being amplified by three-round of PCR and purified by gel extraction, the T7-library-TolA-SecM was divided into aliquots and stored at -80 °C for real selection.

3.2.5. mRNA library preparation

DNA fragments of T7-flag, T7-flag-amber, and T7-GFP were prepared by PCR using PrimeSTAR® GXL DNA Polymerase (TaKaRa bio, Japan) and digested with DpnI (New England Biolabs, USA). The PCR product was purified with QIAquick PCR Purification Kit (QIAGEN, Germany). The resulting PCR product was used as a DNA template for in vitro transcription via the MEGAscriptTM T7 Transcription Kit (Thermo Fisher Scientific, USA). After overnight incubation at 37 °C, the remained DNA template was digested via TURBOTM DNase (Thermo Fisher Scientific, USA). Obtained mRNA product was purified and concentrated by RNA Clean & Concentrator Kits (Zymo Research, USA). The final concentration of mRNA was determined by NanoDrop One (Thermo Fisher Scientific, USA). The purity of mRNA was confirmed by agarose gel electrophoresis (E-Gel™ Go! Agarose Gels, 2%, Thermo Fisher Scientific, USA) after being treated with mRNA unfolding buffer (0.5 mM Sodium Acetate, 0.6 mM EDTA, 26 mM MOPS [3-(N-morpholino) propane sulfonic acid)] for 10 mins at 70 °C. Thirty-five cycles of PCR were performed by using the final mRNA as the PCR template (primer pair #13 and #948). No visible bands should be observed in the electrophoresis result to ensure the complete removal of the remained DNA template. Otherwise, mRNAs will be repeatedly digested with TURBOTM DNase and purified until bands in the electrophoresis become invisible. The resulting mRNA library was stored at -80 °C for further use.

For real selections, the prepared random DNA libraries called T7-library-TolA-SecM were

used as the template for in vitro transcription, and the purification and quality control were performed the same way described above.

3.2.6. Pyrrolysyl-tRNA synthetase (PylRS) and $tRNA_{CUA}$ preparation

For the synthesis of PylRS, the BL21(DE3) *E. coli* was transformed with the plasmid of PET054_MmPylRS-03 and used for the expression of the PylRS, using the same procedure as described in Chapter2 “Large scale protein expression and purification”.

For the synthesis of $tRNA_{CUA}$, DNA fragment for *in vitro* transcription was generated by PCR (PCR template of amber_tRNA, primer pairs of #955 and Rev_OMe_Py-tRNA). After gel extraction with NucleoSpin® Gel and PCR Clean-up kit (Takara Bio, Japan), the resulting DNA fragment was used as the template for in vitro transcription via MEGAscript™ T7 Transcription Kit (Thermo Fisher Scientific, USA). To ensure the 5’ terminal of tRNA has monophosphate for effectively charging amino acid, guanosine monophosphate (GMP) was additionally added at a final concentration of 75 mM into the PCR solution. After translation at 37 °C for 16 h, the remained DNA template was digested by TURBO™ DNase (Thermo Fisher Scientific, USA) and purified via RNA Clean & Concentrator Kits (Zymo Research, USA). The resulting tRNA was divided into aliquots and stored at -80 °C for further use.

3.2.7. Demo selection via ribosome display

The GFP mRNA was mixed with either Flag mRNA or Flag-amber mRNA at the mass ratio of nine to one to generate two different RNA libraries of GFP/Flag or GFP/Flag-amber. A 25 µL cell-free protein synthesis (CFPS) system was constructed for each library. Each CFPS system was composed of 6 µL E. coli S30 lysate extract (1mL/g cell pellet, including ribosome component and translation factors), 8.8 µL of SolC (including energy resource, amino acids, tRNA, etc., the recipe was described in “General buffer recipes”), 2.7 µL of PylRS, 5 µg of $tRNA_{CUA}$, 1.25 µL of 100 mM exo BCN-L-Lysine (stock in 0.2 M 15% DMSO/NaOH solution) and 1 µL of RNaseOUT™ Recombinant Ribonuclease Inhibitor (Thermo Fisher Scientific, USA). The constructed CFPS system was incubated at 37 °C for 15 mins for ribosome assembly. Then, 5 µg 37 °C pre-heated mRNA library (GFP/Flag or GFP/Flag-amber) was added into each CFPS system and each system was incubated at 37 °C for 15 mins for the generation of peptide-ribosome-mRNA complexes (PRMs). After translation, the excessive free exo BCN-L-Lysine was removed through buffer exchange using 50% DMSO contained Click Replace Solution (prepared by mixing with Click Replace Solution and 100% DMSO at equal volume) via the desalt spin column (NucAway™ Spin Columns, Thermo Fisher Scientific, USA or MicroSpin™ S-200 Column, Cytiva, USA). Then, 1 µL of 100 mM 5-FAM-PEG4-Tetrazine DMSO solution (Conju-probe, USA) was added into the CFPS system, and volume up to 100 µL with 50% DMSO contained Click Replace Solution. 5 mins incubation at 37 °C was allowed for the click reaction between exo BCN-L-lysine incorporated PRMs and FAM-PEG4-Tetrazine. After the click reaction, the excessive 5-FAM-PEG4-Tetrazine was

removed through buffer exchange with Click Replace Solution by desalt spin column. Next, the CFPS solution was mixed with 20 μL anti-FAM magnetic beads and 100 μL ice-cold WBT (the recipe was described in "General buffer recipes"). The resulting solution was incubated at 4 °C for 30 mins to allow the affinity binding between FAM-conjugated PRMs and anti-FAM beads. Next, the magnetic beads were extensively washed with 390 μL ice-cold WBT eight times to remove unbounded PRMs. After washing, mRNAs were released from PRMs by mixing magnetic beads with 130 μL Elution buffer (the recipe was described in "General buffer recipes") and heating at 75 °C for 5 mins. The released mRNA was purified through RNA Clean & Concentrator Kits (Zymo Research, USA) and reverse-transcribed into cDNA via SuperScript® IV Reverse Transcriptase (Thermo Fisher Scientific, USA) with the primer of #13. Meanwhile, the unselected input RNA library was 1000-fold diluted with distilled water and reverse-transcribed into cDNA as the control group. Next, all the cDNAs are used as the template for PCR with primer pairs of #13 and #948 at 15,20,25,30,35 cycles. Additionally, PCR without a template was performed to ensure no primers had been contaminated with DNA. Finally, PCR products were visualized by polyacrylamide gel electrophoresis with ethidium bromide staining.

3.2.8. Chemical synthesis and structure characterization of BMS-1166-tetrazine

72.00 mg (1 eq.) of BMS-1166 (DC Chemicals, China), 31.63 mg (1.5 eq.) of 1-(3-dimethylaminopropyl)-3-ethylcarbodiimide Hydrochloride (EDC·HCl), and 22.29 mg (1.5 eq.) of anhydrous 1-hydroxybenzotriazole (HOBt) was dissolved in 1 mL anhydrous DMF and stirred at 4 °C for 1 h. After 1h reaction, 23.01 μL (1.5 eq.) of triethylamine (TEA) and 25.00 mg (1.2 eq.) of (4-(1,2,4,5-tetrazin-3-yl)phenyl)methanamine hydrochloride (Amine-tetrazine) was dissolved into 400 μL anhydrous DMF and dropwise transferred to the BMS-1166 solutions. The resulting solution was stirred at RT for 17 h. After removing the solvent under reduced pressure, the resulting BMS-1166-tetrazine was first purified by silica gel flash chromatography (Hexane: Ethyl acetate = 5:5 to Ethyl acetate: Methanol = 9:1, v/v). After confirming the structure by ^{1}H-NMR (JEOL, Japan, DMSO-D6 as solvent) and MALDI- MS (α-Cyano-4-hydroxycinnamic Acid (CHCA) as the matrix, microflex® LRF, BRUKER, USA), the BMS-1166-tetrazine was furtherly purified by high-performance liquid chromatography (HPLC).

3.2.9. Reactivity test between CFPS translated peptide and tetrazine compounds

PCR039 plasmid (which translated into a fusion protein as HAT-Thioredoxin-TEV-Peptide-Amber-Flag, 100 ng/25 μL CFPS system) was used to construct three 25 μL CFPS systems. After 3 h of translation at 37 °C, the resulting proteins were desalted first to remove excessive exo BCN-L-Lysine with Desalting Buffer (1mM DTT, 50 mM Tris-HCl, 0.5 mM EDTA, pH = 8.0). Next, TEV protease (New England Biolabs, USA) was added at 0.1% v/v, and cleavage was performed by incubation at 30 °C for 1 h. Next, BMS1166-tetrazine or 5-FAM-PEG4-Tetrazine or DMSO was added at a final concentration of 1 mM (10% DMSO), and click

reaction was allowed at 4 °C for 15 min. Next, exo BCN-L-Lysine was added at 10 mM to quench the excessive tetrazine compounds. The above solution was mixed with 10 µL anti-Flag magnetic beads (MEDICAL & BIOLOGICAL LABORATORIES, Japan) and volume up to 900 µL with Washing Buffer (50 mM Tris-HCl, 150 mM NaCl, pH = 7.5). Affinity capture was allowed by incubation under 4 °C for 36 h. Then the anti-Flag magnetic beads were washed with Washing Buffer for three times, followed by washing with water for three times. Next, peptides were released from magnetic beads by mixing beads with 10 µL 0.2% TFA-contained water solution and incubating at room temperature for 10 mins. Finally, the peptides were detected by MALDI-MS (microflex® LRF, BRUKER, USA) with the α-cyano-4-hydroxycinnamic Acid as the matrix.

3.2.10. Real selection via ribosome display

CFPS system (5 µg input RNA library to every 50 µL CPFS system) was constructed using the same method as in the section of demo selection (3.2.6). After 15 mins pre-heating of the CFPS system and random RNA library, the CFPS was mixed with the random RNA library and incubated for 15 mins for translation. After removing the excessive exo BCN-L-Lysine with desalt spin column with Click Replace Solution, BMS-1166-tetrazine was added at a final concentration of 2 mM (10% DMSO), and click reaction was performed at 4 °C for 15 mins to form the BMS-1166-PRMs. After removing the excessive BMS-1166-tetrazine in the same method as described, the resulting solutions were mixed with freshly prepared anti-Flag magnetic beads (33.5 µL anti-Flag beads to 5 µg input RNA library) and incubated at 4 °C for 1 hour to allow the negative selection for removing Flag-target PRMs or protein-G-target PRMs. After negative selection, the supernatant was mixed with PD-L1-His tag (Recombinant human PD-L1 protein, ab167713, Abcam, UK) at a final concentration of 30 ng/µL and incubate at 4 °C for 30 mins to allow the interaction between BMS-1166-PRMs and PD-L1. Next, the resulting solutions were mixed with freshly prepared anti-His tag magnetic beads (67 µL anti-His tag beads to 5 µg input RNA library) and incubated at 4 °C for 30 mins to capture all PD-L1-His tag proteins. Next, the anti-His tag beads were extensively washed by WBT sixteen times. Specifically, at the 4th, 8th, 12th, and 16th time, 390 µL WBT was mixed with beads and vertexing together for 30 mins at 4 °C. After sixteen-times wash process, the PRMs complex was eluted by competitive elution with HAC by mixing HAC contained WBT (final HAC concentration of 10 µM) and incubating at 4 °C for 30 mins. Next, the mRNAs were released from PRMs and purified with RNA Clean & Concentrator Kits (Zymo Research, USA) and then were reverse transcribed into cDNA. A small part of cDNA was used to perform PCR for verifying the selection result. Based on the results, a suitable PCR cycle round was determined, and recovered cDNAs were used as a PCR template to prepare a new random DNA library. Finally, the new DNA library was used to transcript into the RNA library and used for the next round of selection.

Some minor differences are varied between different rounds of selection. At 1st round selection, 10 µg of input library was used for 50 µL of the CFPS system to increase the

sequence diversity. Besides, all the recovered mRNA from PRM were used as templates for reverse transcription to maximize the sequence diversity. At 3rd round selection, half of the washed anti-His tag magnetics beads were eluted by MAA[10], which is a protein that has a similar IgV-like structure as PD-1 without binding affinity to PD-L1; while the other half of the beads were eluted with HAC. At 4th round selection, 48 μM final concentration of wild-type PD-1 was first used to compete out weak-binding PRMs, after washing out weak-binding PRMs, 8 μM final concentration of HAC was used to elute strong-binding PRMs. Begin with the 5th round selection, 26 μM final concentration of 2-PD-1 was first used for pre-elution to elute weak and medium-binding PRMs, after washing out the 2-PD-1 eluted PRMs, 8 μM final concentration of HAC was used to elute strong binding PRMs. Begin with the 6th round selection, 1% Bovine Serum Albumin (BSA, RNase free, final concentration was 20 μM) was included in the WBT as the interference. On the other hand, 2-PD-1 was added as the interference (final concentration of 20 μM) into the tube during the PD-L1 incubation and PD-L1 capturing process at 6th round selection. To be noted, the sequencing data of this group was only used for filtering out the low-count peptides in edgeR and PCA. Within all the above six rounds of selection, only HAC-eluted PRMs were used to produce the DNA/RNA library for next-round selection. Besides, an additional 4th round selection was performed using the same input RNA library as 4th round selection. Elution Buffer or HAC was separately used for the elution process. The sequencing results of this additional selection round were only used for filtering out the low-count peptides in edgeR and PCA.

At the 7th round selection, during the PD-L1 dimerization process, half of the beads were incubated with HAC-His tag protein instead of PD-L1-His tag protein, as a counterpart negative-target selection. After capturing the PD-L1-His tag and HAC-His tag via anti-His tag magnetic beads and extensive washing of the beads, the PRMs were eluted sequentially by first WBT, then by 20 μM 2-PD-1 containing WBT, then by 45 μM HAC containing WBT, finally eluted by Elution Buffer with heating.

3.2.11. Next-generation sequencing (NGS) and data pretreatment

Two sequencing techniques (Illumina Miseq and Oxford Nanopore MinION) were used for the Next-generation sequencing for all-rounds eluted samples. Detailed sample information could be known from the legend of PCA results. For the sample preparation for the Illumina Miseq sequencing, the DNA recovered from each selection was amplified by primer pairs #1414 and #1415 at an optimized PCR cycle. After being purified by NucleoSpin® Gel and PCR Clean-up kit (Takara Bio, Japan), samples were sent to the Support Unit for Bio-Material Analysis (BMA) in RIKEN Center for Brain Science and NGS was performed by the technical staff using Miseq system (Illumina, USA). Next-generation sequencing via Oxford Nanopore MinION was performed using PCR Barcoding Kit (SQK-PBK004, Oxford Nanopore, Technologies, UK) for sample preparation and MinION Mk1B as the sequencing device. Base calling data were obtained from both methods as the raw NGS results.

The read count table is a necessary input for peptide differential binding analysis and PCA. Therefore, the first step was to process the raw base calling data into the peptide read count table. Firstly, the average quality score of every single sequence was calculated to filter out the low-quality base calling data. Due to the accuracy of each sequencing technique, different criteria of the quality score were used for the filtering. For the Illumina Miseq sequencing result, sequences with an average quality score below 30 were filtered out; for the Oxford Nanopore MinION sequencing result, sequences with an average quality score below 20 were filtered out. This filtering process ensured an average accuracy of 99.9% for Illumina Miseq sequencing results and an average accuracy of 99% for Oxford Nanopore MinION sequencing results. Then, DNA sequencing data were translated into amino acids sequence where amber codon was translated into ncAA of exo-BCN–L–Lysine, indicated by letter "B." The peptide sequences were filtered with a fixed pattern of "MTTCxxxxxBxxxxxCSWD" ("x" stands for any canonical amino acid, and "B" stands for the ncAA) and organized into a read count table via a self-made python script. The final read count table comprised every unique peptide sequence and its read number in each NGS sample.

3.2.12. Differential binding analysis for determining peptide candidates

Recently, Karlis Pleiko. Identify the organ-specific peptides from their phage display results using a well-known RNA-seq analysis R package, edgeR [11]. Here, edgeR was also used in this study for identifying the specific binding peptide candidates. The complete R script can be accessed from GitHub (https://github.com/Cinamoyang/display_analysis_script). A brief concept and critical steps were described here as follows. First, the above peptide read count table was used as input data. Theoretically, the peptides should be gradually enriched along with the increased selection round and thus be detected in most selection rounds. Therefore, only peptides with zero read count number for less than fourteen of twenty-nine libraries are kept. Then, since different NGS libraries have different sequencing depths, the actual read count number of the peptide was not accurate enough to represent its abundance. The edgeR build-in "TMMwsp" method was used to normalize the read count number according to its sequencing depth. Based on the observed mean-variance relationship for the replicates of peptides, edgeR assumes the read count number of peptides follows the negative binomial distribution, whose shape depends on two parameters, mean and dispersion. Different treatments (i.e., different targets, different elution methods) and the properties of the peptide itself together determine the final mean read count of the peptide. For all 7th-round peptide libraries, the generalized linear model was set as $log2(\mu) = \beta_0 + \beta_1 x_1 + \beta_2 x_2 + \beta_3 x_3 + \beta_4 x_4 + \beta_5 x_5 + \beta_6 x_6 + \beta_7 x_7$. Here the β_0 represents the peptide-specific mean read count number; $\beta_1$represents the elution method of 2-PD-1; β_2 represents the method of HAC; β_3 represents the elution method of urea; β_4 represents the selection target of PD-L1; β_5 represents the interaction term of the elution method of 2-PD-1 together with the selection target of PD-L1; β_6 represents the interaction term of the elution method of HAC together with the selection target of PD-L1; β_7 represents the interaction term of the elution method of urea together with the selection target of PD-L1. The sequencing method of Illumina Miseq

and Oxford Nanopore MinION were used as replicates of the same treatment. As all treatments (elution method and selection target) were included, the count number from different libraries could be represented from various combinations of dummy variable x_1 (0 or 1) for a specific peptide sequence. For example, the mean read count of a particular peptide that was eluted by 2-PD-1 from the target of PD-L1 (2-PD-1_PD-L1) could be represented as $log2(\mu_{2PD-1\_PD-L1}) = \beta_0 + \beta_1 * 1 + \beta_2 * 0 + \beta_3 * 0 + \beta_4 * 1 + \beta_5 * 1 + \beta_6 * 0 + \beta_7 * 0$; while for this peptide, the mean read count eluted by 2-PD-1 from the target of HAC could be represented as $log2(\mu_{2PD-1\_HAC}) = \beta_0 + \beta_1 * 1 + \beta_2 * 0 + \beta_3 * 0 + \beta_4 * 0 + \beta_5 * 0 + \beta_6 * 0 + \beta_7 * 0$. Since the difference between 2-PD-1_PD-L1 and 2-PD-1_HAC originated from β_4 and β_5, if the peptide sequence has $\beta_4 + \beta_5 \neq 0$, then the peptide will have a different count number between the target of PD-L1 and HAC when eluted by the 2-PD-1. Furthermore, the higher the value of $\beta_4 + \beta_5$ means the condition of the target of PD-L1 during 2-PD-1 will give a higher final peptide read count. Therefore, hypothesis testing with a null hypothesis of $\beta_4 + \beta_5 = 0$ and an alternative hypothesis of $\beta_4 + \beta_5 \neq 0$ was used to find peptides that showed statistically significant (false-discovery rate, FDR less than 0.1) differences between the two selection targets during 2-PD-1 elution. Furthermore, the peptides which had more read count to the target of PD-L1 than HAC during 2-PD-1 elution could be found by searching $\beta_4 + \beta_5$ more than one (approximately 2-fold more enrichment in the target of PD-L1 than the target of HAC). The edgeR package first fitted the above generalized linear model with the normalized count table to deduce the dispersion and β of each peptide sequence through several fitting methods. Then edgeR performed the hypothesis testing (glmQLFTest) for the desired combination of the β and calculated the FDR. Three types of peptides were separately found using a different combination of βs together with the mutual criteria of FDR < 0.1 and β_{sum} >1: (a) peptides that have more elution against the target of PD-L1 than HAC during 2-PD-1 elution ($\beta_{sum} = \beta_4 + \beta_5$). (b) peptides that have more elution against the target of PD-L1 than HAC during HAC elution ($\beta_{sum} = \beta_5 + \beta_7$). (c) peptides that have more elution with 2-PD-1 and HAC than washing buffer ($\beta_{sum} = 0.5 * (\beta_2 + \beta_3 + \beta_6 + \beta_7)$). The intersection was taken from (a), (b), and (c) to find the peptide sequence has all three properties. The final FDR was calculated by $1 - (1 - FDR_a) * (1 - FDR_b) * (1 - FDR_c)$.

3.2.13. Principal component analysis (PCA)

PCA was performed for the top two-hundred peptide sequences with the largest standard deviations across all NGS sample libraries via the build-in function from edgeR. The obtained x and y coordinates were imported into GraphPad Prism 9 for plotting the figure. The contribution rate of each component was calculated from their eigenvalue. The full R script can be accessed from GitHub (https://github.com/Cinamoyang/display_analysis_script).

3.2.14. PD-1/PD-L1 inhibition assay with 10% DMSO

AlphaLISA Human PD-1 and PD-L1 binding Kit (PerkinElmer, USA) was used for the assay.

100% DMSO solutions of inhibitors were mixed with 10X assay buffer (Kit provided) and volumed up with water to give a 40% DMSO-containing inhibitor 1X buffer solution. Each stock solution of inhibitors was made by mixing 100% DMSO inhibitor solution with 10X assay buffer and water to give 40% DMSO buffered stock solution. Serial dilution of inhibitors was prepared using the 40% DMSO-contained 1X buffer solution and 40% DMSO buffered stock solution. Assay solution (6.67 nM of Biotinylated PD-1 (Kit provided), 6.67 nM of His tagged PD-L1 (Kit provided), 26.67 µg/mL of streptavidin Donor beads, 13.33 µg/mL of anti-His tag Acceptor beads, 1X assay buffer) was added into the 384-well plate (ProxiPlate, PerkinElmer, USA) at 6 µL/well. Next, serial dilutions of inhibitor were added to each well at 2 µL/well to give the final concentration of 10% DMSO and incubated at RT for 90 mins in a dark environment. The AlphaLISA signal of each well was measured using the plate reader (EnSpire™, PerkinElmer, USA). The normalized AlphaLISA signal percentage was calculated by subtracting each AlphaLISA signal at specific concentration with the background signal (usually using the signal at the highest BMS-1166 concentration or nivolumab concentration) and divided each subtracted AlphaLISA signal with the subtracted AlphaLISA signal at the lowest sample concentration.

3.2.15. Solid-phase peptide synthesis

The canonical peptides were synthesized using Liberty Blue (CEM Japan, Japan) with standard Fmoc protected amino acids (CEM Japan, Japan) and Rink Amide Resin (ProTide, CEM Japan, Japan). After releasing the peptides from resin with Cleavage Cocktails (5% w/v Phenol, 5% v/v H_2O, 5% v/v thioanisole, 2.5% v/v 1,2-ethanedithiol, 1% v/v triisopropylsilane, 81.5% v/v trifluoroacetic Acid, 2 mL used for 0.025 mmol resin, 2 h incubation at 40 °C), the peptides were precipitated and washed with ether. The dried peptides were purified with HPLC and lyophilized. The peptide concentration was determined by NanoDrop One (Thermo Fisher Scientific, USA), and the extinction coefficient of each peptide was calculated using the ProtParam (https://web.expasy.org/protparam/).

The BMS-1166-peptide was synthesized in a two-step method: the BCN-peptide was first chemically synthesized by NHS-BCN coupling onto the lysine residue of the peptide, then the BCN-peptide was incubated with BMS-1166-tetrazine to give the final product of BMS-1166-peptide. BCN-peptides were synthesized using a reported method [12]. Briefly, standard Fmoc protected amino acids (CEM Japan, Japan) and N^2-(((9H-fluoren-9-yl)methoxy)carbonyl)-N6-(2,2,2-trifluoroacetyl)-L-lysine (Fmoc-Lys(Tfa)-OH) (BLDpharm, China) was used as building blocks for synthesizing the N-acetylated peptides using Liberty Blue (CEM Japan, Japan) on the Rink Amide Resin (ProTide, CEM Japan, Japan). The Fmoc-Lys(Tfa)-OH was used as the building block for peripheral lysine that would not be modified into BCN-Lysine. After releasing the peptides from resin with Cleavage Cocktails, peptides were precipitated and washed with ether. Dried peptides were dissolved into DMF. For the No.1 and No.3 peptides, 3 eq. of (1R,8S,9r)-bicyclo[6.1.0]non-4-yn-9-ylmethyl

succinimidyl Carbonate (exo-BCN-NHS carbonate) (SiChem, China) and 4 eq. of N,N-diisopropylethylamine were added and the resulting solution was stirred for 17 h at RT. For the No.2 peptide, 0.8 eq. of exo-BCN-NHS carbonate and 1 eq. of N,N-diisopropylethylamine was dissolved into DMF and dropwise added into the DMF solution of No.2 peptide, the resulting solution was stirred for 17 h at RT. After the reaction, the solvent of DMF was removed by lyophilization. The Tfa-protected BCN-peptides were purified through HPLC and lyophilized again to remove the solvent. To remove the protecting group of TFA, the purified Tfa-protected BCN-peptides (No.1 and No.3) were treated twice with 1mL Deprotect Solution (aq. NaOH/Dioxane at 1:2 v/v, final concentration of aq. NaOH is 0.1 M) for 30 min at RT. The pH of deprotected BCN-peptides were adjusted around 7.5 and BMS-1166-tetrazine was added and incubated at RT for 15 mins. The resulting BMS-1166-peptides were purified with HPLC and lyophilized. The concentration of peptides was estimated using the Pierce™ BCA Protein Assay Kit (Thermo Scientific, USA).

3.3. Results

3.3.1. Demo selection

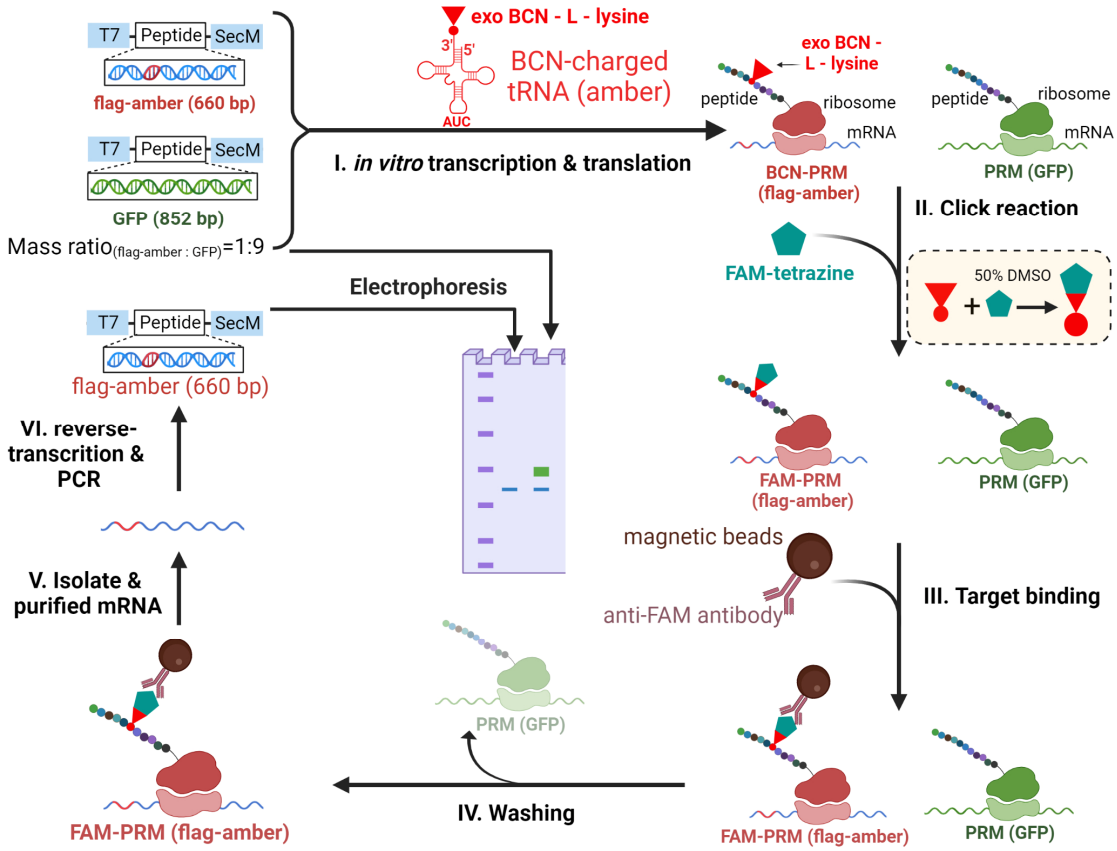

Figure 3.3.1. Schematic illustration of the demo selection. A long DNA sequence of GFP (amber-lacking) and a short DNA sequence of flag-amber (amber-containing) were mixed at a mass ratio of 9:1 to give a demo DNA library. Peptide/ribosome/mRNA complex (PRM) was formed for both sequences while the amber codon within flag-amber would be translated into exo BCN-L-Lysine to give the BCN-peptide. After FAM-tetrazine was added, the click reaction occurred between BCN-peptide and FAM-tetrazine under 50 % DMSO to form the FAM-PRM. The FAM-PRM of flag-amber would be captured by anti-FAM magnetic beads while the PRM of GFP could not and thus be washed out. DNA sequences were recovered from the anti-FAM magnetic beads and visualized by electrophoresis. T7: T7 promoter; SecM: ribosome arrest sequence; PylRS: Pyrrolysyl-tRNA Synthetase.

To test the compatibility of the two-step SMI-peptide synthesis with ribosome display, a demo selection was designed by using tetrazine-modified fluorescent dye of fluorescein (FAM) as “SMI-tetrazine” to synthesize the FAM-peptide and selecting FAM-peptide with anti-FAM magnetic beads (**Figure 3.3.1**). As the FAM-peptide was formed by the click-reaction between FAM-tetrazine and BCN-peptide, only the amber codon-contained sequence could generate BCN-peptide and be selectively enriched. Therefore, two kinds of sequences were prepared for the selection: an amber codon-contained sequence and an amber codon-

lacking coding sequence. To facilitate the visualization of selection result via electrophoresis, the amber codon-lacking sequence was designed to be longer than the amber-contained sequence. Two kinds of sequences were mixed to form the mixed library for the demo selection.

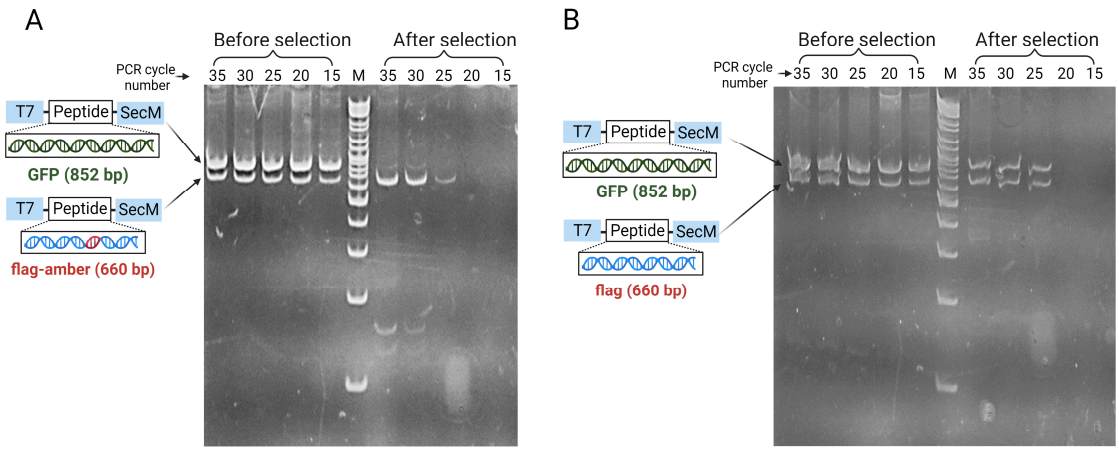

Figure 3.3.2. Demo selection results indicate the click-reaction could be combined with ribosome display. Demo selection was performed using FAM-tetrazine and anti-FAM beads. (A) In the case of the amber codon-lacking sequence of GFP and amber codon-contained sequence of flag-amber, enrichment was observed for flag-amber. (B) In the case of the amber codon-lacking sequence of GFP and the amber codon-lacking sequence of the flag, no enrichment was observed. M: DNA ladder markers.

As shown in **Figure 3.3.2.A**, before the selection, the mixed library is composed of both the short amber codon-contained sequence of flag-amber and the long amber codon-lacking sequence of GFP, while after the selection, flag-amber was specifically enriched than GFP. Besides, when removing the amber codon from the flag-amber, the amber codon lacking sequence could be enriched (**Figure 3.3.2.B**). These results indicated the FAM-peptide was successfully synthesized in response to the amber codon as designed. Moreover, the selection is based on the interaction between FAM-peptide and anti-FAM antibodies while the results are detected as DNA enrichment, indicating that FAM-peptide forms the FAM-PRM with mRNA under 50 % DMSO contained click buffer to facilitate the ribosome display.

3.3.2. BMS-1166-tetrazine synthesis and characterization

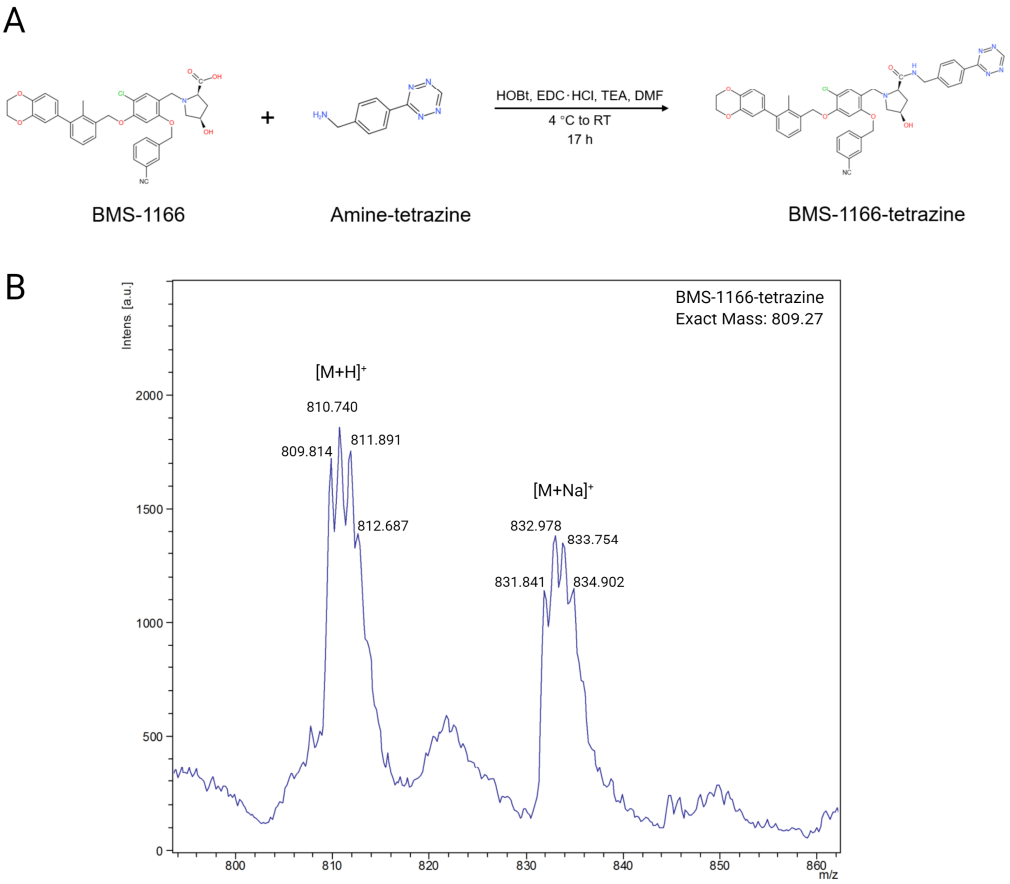

Figure 3.3.3. BMS-1166-tetrazine synthesis and structural characterization. (A) The synthesis scheme of BMS-1166-tetrazine. (B) MALDI-MS results of BMS-1166-tetrazine. Plus-proton peaks and plus-sodium peaks could be observed as monoisotopic peaks.

Since the demo selection successfully proved that click-reaction could be combined with ribosome display, the next step was the preparation of the real selection, beginning with the synthesis of SMI-tetrazine. One of the BMS compounds introduced in Chapter1, BMS-1166, was chosen as the SMI for its relatively low cytotoxicity and high inhibitory activity among the BMS compounds. Besides, BMS-1166 contains a carboxylic acid group at its hydrophilic tail which facilitates its chemical modification with amine-tetrazine. As shown in **Figure 3.3.3.A**, amine–carboxylic acid coupling reaction was used for preparing the BMS-1166-tetrazine. After double-purification through flash chromatography and HPLC, the structure of BMS-1166-tetrazine was confirmed through MALDI-MS and ^{1}H-NMR (**Figure 3.3.3.B Figure 3.3.4**). These results proved that the BMS-1166 was successfully modified with tetrazine to be the BMS-1166-tetrazine.

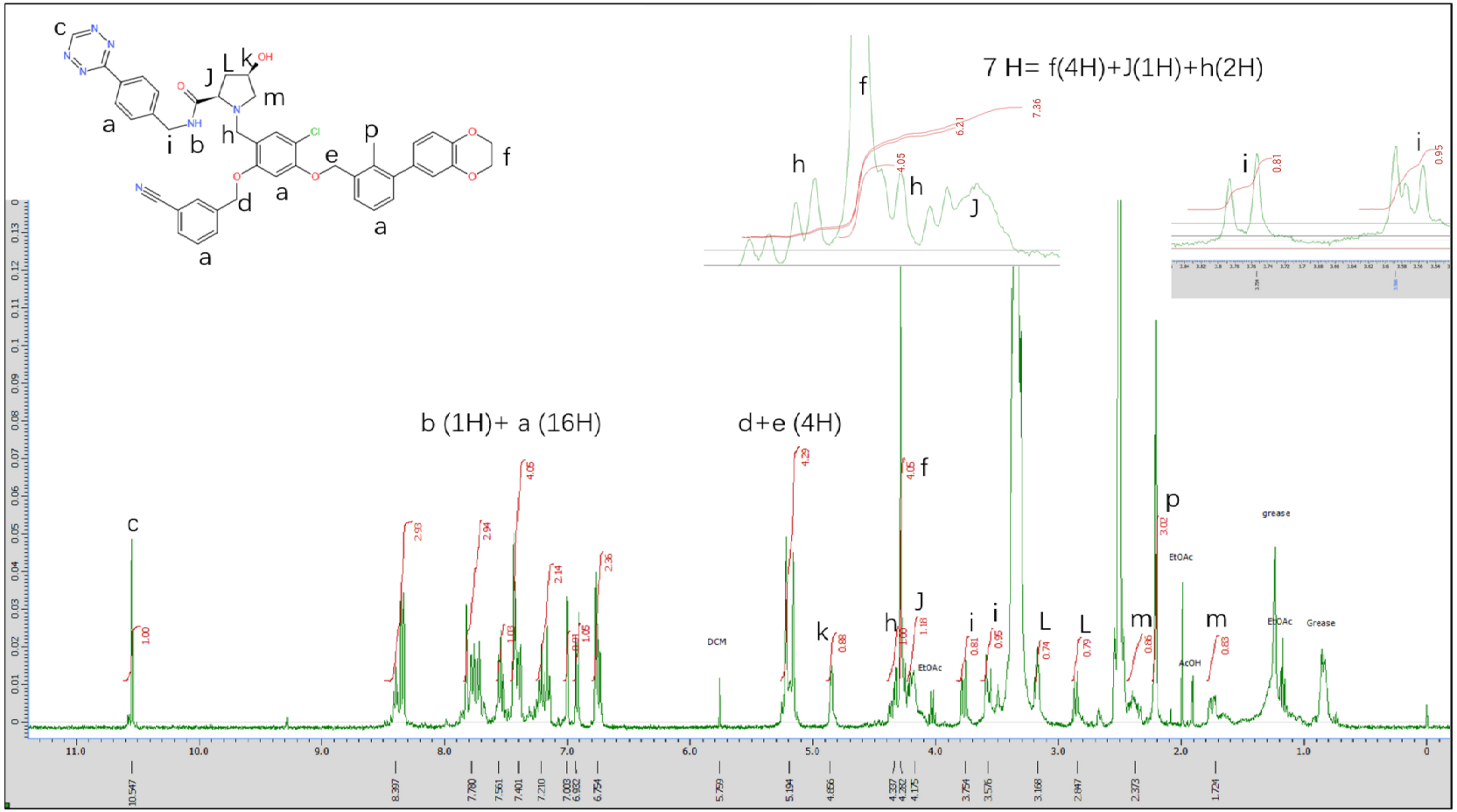

Figure 3.3.4. [1]H-NMR spectra result of BMS-1166-tetrazine. Peaks were assigned to corresponding protons, indicated as characters in the graph. Specifically, the characterized tetrazine-originated proton (proton “c” in the result, chemical shift around 10.5)[13] was observed from the NMR results, indicating the success of conjugation.

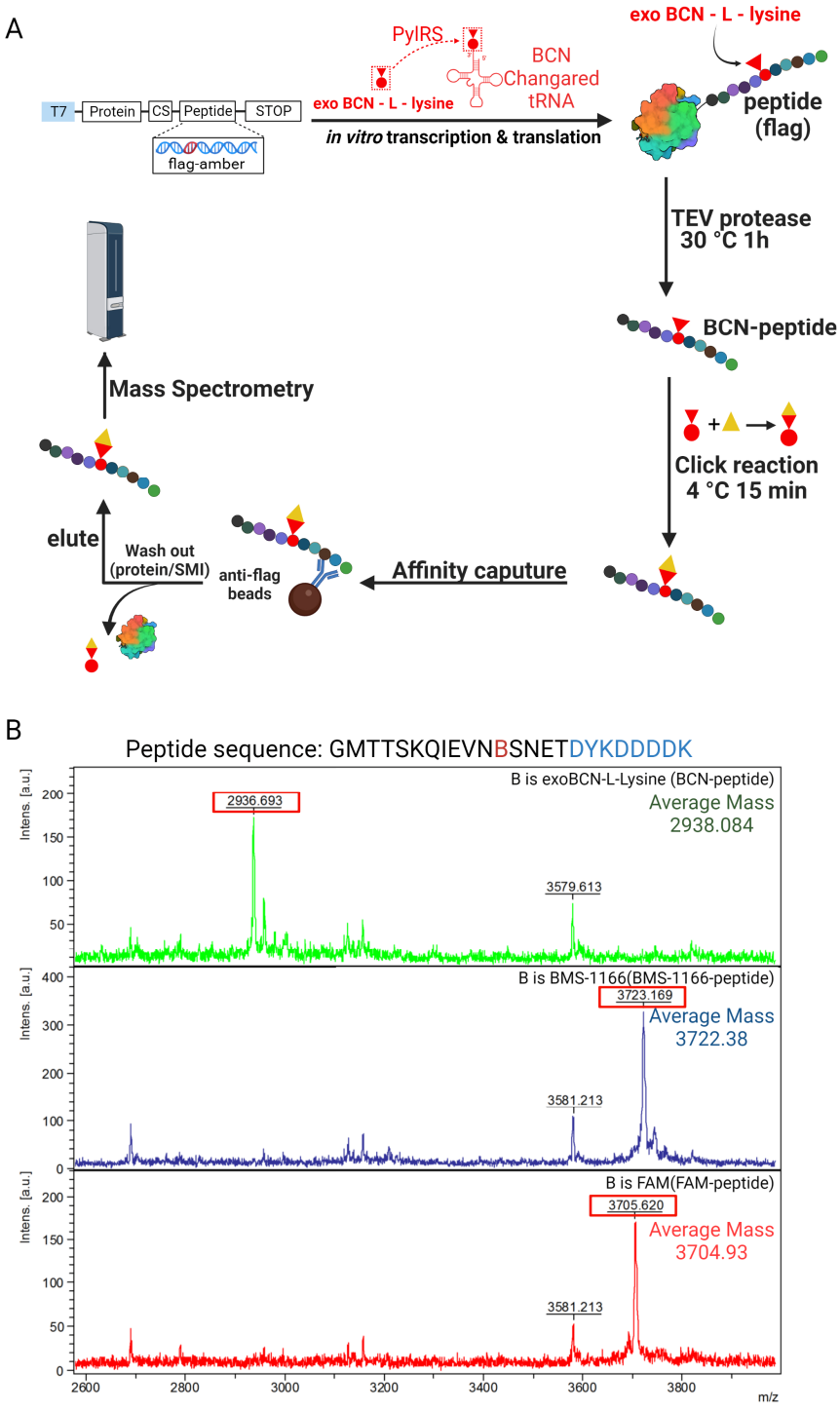

Figure 3.3.5. Reactivity verification of BMS-1166-tetrazine. (A) Schematic illustration of the click-reaction reactivity test. BCN-peptide was synthesized by translation of a fusion protein and released by protease cleavage. BCN-peptide was then reacted with the BMS-1166-tetrazine, positive control of FAM-tetrazine, or negative control of DMSO. The resulting peptides are purified through magnetic beads and detected by MALDI-MS. CS: cleavage-site for Tobacco Etch Virus (TEV) Protease. (B) The MALDI-MS results of the reactivity test. The average mass of each peptide is indicated in the graph.

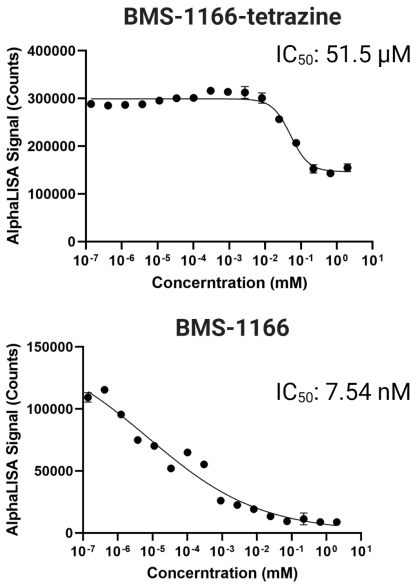

Figure 3.3.6. Inhibitory ability verification of BMS-1166-tetrazine. PD-1/PD-L1 inhibition results using AlphaLISA assay. Although BMS-1166-tetrazine could inhibit PD-1/PD-L1 interaction, its inhibitory effect is weaker than BMS-1166. Each data point is the quadruplicate of the experiment.

Since BMS-1166-tetrazine was composed of two functional parts: the tetrazine parts for click-reaction and the BMS-1166 part for PD-1/PD-L1 inhibition; two experiments were designed to confirm these functionalities (**Figure 3.3.5 and Figure 3.3.6)**. The reactivity of BMS-1166-tetrazine was confirmed by reacting with *in vitro* synthesized BCN-peptide, followed by the MALDI-MS detection. To be noted, 4 °C but not 37 °C was tested for the click-reaction reactivity as this condition could further stabilize the PRM during the ribosome display. As demonstrated in **Figure 3.3.5.B**, the peak of BMS-1166-peptide could be observed from MALDI-MS without nearby impurity peaks and showed an increase in mass compared to the BCN-peptide. To confirm the PD-1/PD-L1 inhibition ability of BMS-1166-tetrazine, a commercial AlphaLISA assay was used as its signal would be decreased when PD-1/PD-L1 interaction was inhibited. As shown in **Figure 3.3.6**, BMS-1166-tetrazine has the inhibitory ability to decrease the PD-1/PD-L1 AlphaLISA signal, indicating its feasibility as the key molecular in peptide to provide preliminary protein interaction. However, its inhibitory activity is much weaker than BMS-1166, presumably due to the modification with tetrazine inducing the unfavorable steric hindrance with PD-L1. This phenomenon has been recently reported as the modification of the carboxylic acid group of BMS-1166 by amine-derived pomalidomide abolished the activity of BMS-1166[10]. However, as the final desired inhibitor form is the BMS-1166-peptide, a sophisticatedly designed ribosome display selection could find a peptide sequence to remedy the decreased inhibitory activity and even show a higher inhibitory effect than the original BMS-1166.

3.3.3. Real selection

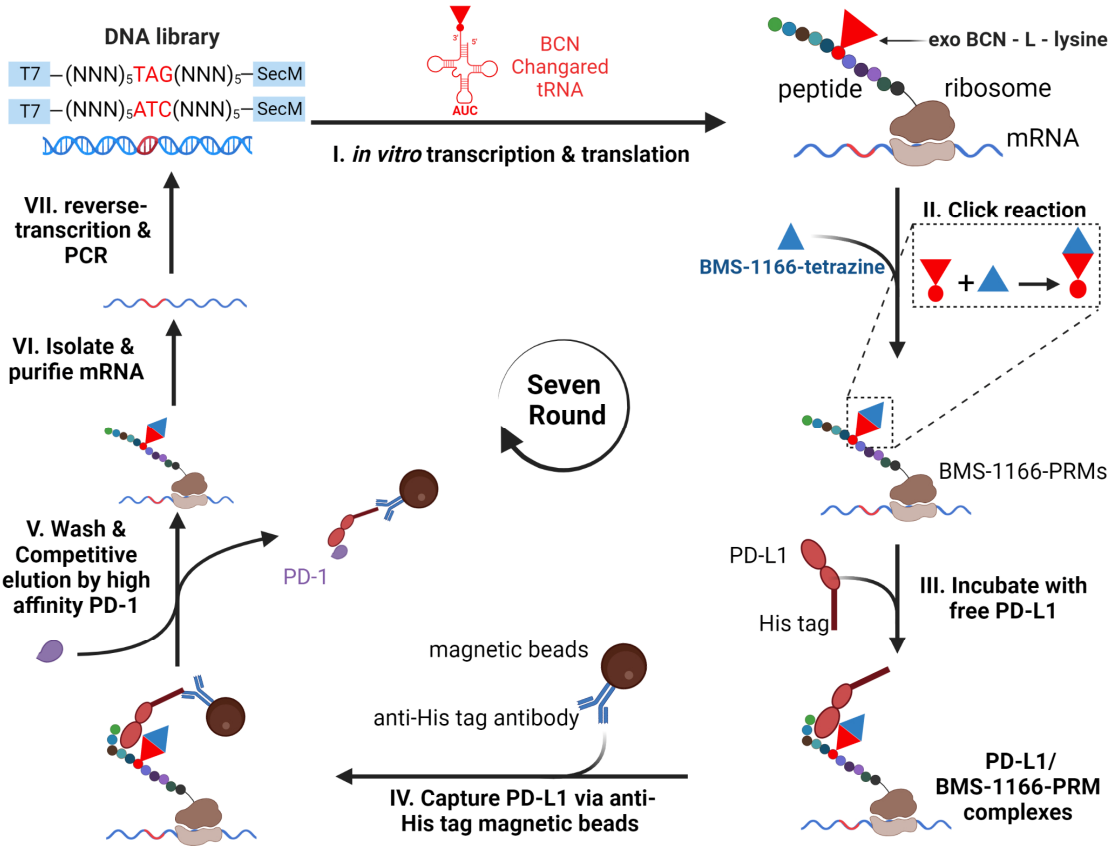

Figure 3.3.7. Schematic illustration of real selection for BMS-1166-peptide. DNA library was designed to contain ten randomized codons while having a fixed amber codon (TAG) at the center. Firstly, random BCN-peptides were synthesized via in vitro translation and held with their coding sequence as the BCN-PRMs via ribosome. Next, BMS-1166-tetrazine was mixed with BCN-PRMs to prepare the BMS-1166-PRMs. The BMS-1166-PRMs were then incubated with free PD-L1-His tag to facilitate their interaction to form the PD-L1/BMS-1166-PRM complex. All the PD-L1-His tag was then captured by anti-His tag magnetic beads and PD-L1-unbound BMS-1166-PRMs would not be co-captured and be washed out. In the elution step, high-affinity PD-1 was used to competitively elute the BMS-1166-PRMs. The mRNA was then recovered from the PRMs and reverse-transcribed into a new DNA library for the next round of selection. T7: T7 promoter; SecM: ribosome arrest sequence; PylRS: Pyrrolysyl-tRNA Synthetase.

The selection of BMS-1166-peptide was performed as shown in **Figure3.3.7**. Different from the demo selection, which used a defined, amber-contained peptide coding sequence, the real selection used a DNA library composed of randomized peptide coding sequences. Specifically, the DNA library used in the real selection was designed to contain an amber codon (ATG) flanked by each of five random codons on both two sides. Since each random codon could encode 20 amino acids while the amber codon encodes the exo BCN-L-lysine, the initial DNA library could theoretically encode 10^20 different BCN-peptide sequences. Similar to the demo selection, the ribosome stalled at the secM sequence after the BCN-

peptides translation and linked each BCN-peptide with its coding sequence as the BCN-PRMs. BMS-1166-tetrazine was added to the BCN-peptide and incubated at 4 °C to form the BMS-1166-peptide. Since the BMS-1166 binds to PD-L1 by inducing PD-L1 dimerization, BMS-1166-PRMs may also bind to PD-L1 in the same way. As the pre-immobilization of PD-L1 onto the beads may inhibit PD-L1 dimerization, BMS-1166-PRMs were first mixed with free PD-L1-His tag and then the PD-L1 bound BMS-1166-PRMs were co-captured through anti-His tag beads via PD-L1 capturing while the unbound BMS-1166-PRMs would be washed out.

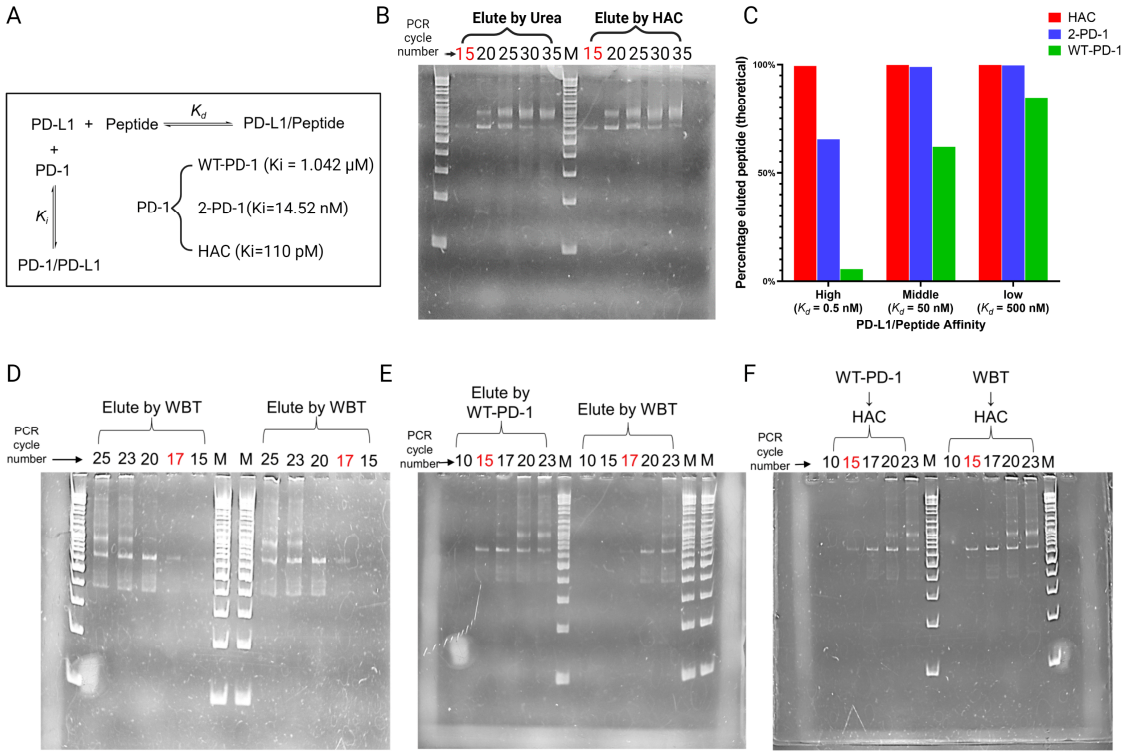

Figure 3.3.8. Competitive elution using PD-1 variants to elute PD-L1-specific BMS-1166-PRMs. (A) The chemical equation for the PD-1 variants-PD-L1-Peptide reaction. As the PD-1 variants were used as inhibitors here, the dissociation constants of PD-1/PD-L1 were represented as K_i. The dissociation constant of 2-PD-1/PD-L1 and WT-PD-1/PD-L1 was experimentally determined (Chapter2) while the dissociation constant of HAC was obtained from the reported paper[14]. The dissociation constant (K_d) between PD-L1 and peptide could not be determined during the ribosome display and thus be assumed as different values to represent the high-affinity (K_d = 0.5 nM), middle-affinity (K_d = 50 nM), and low-affinity (K_d = 500 nM) BMS-1166-PRMs. (B) Experimental elution results using urea or HAC. The least PCR cycle that could visualize the recovered DNAs was marked as red color. (C) Theoretical elution ability for 10 μM HAC, 2-PD-1, and WT-PD-1 to elute different affinity of PD-L1 binding peptides (BMS-1166-PRMs). A one-to-one stoichiometry for PD-L1 and peptide binding was used to simplify the calculation. (D) At 4th round selection, an equal amount of BMS-1166-PRMs captured magnetics beads was eluted by WBT, same least PCR cycle number of 17 was observed for both beads. (E) When beads were eluted with either WT-PD-1 or WBT. A smaller least PCR cycle number was observed in WT-PD-1, indicating it eluted more PRMs than WBT. (F) Beads

were pre-eluted with either WT-PD-1 or WBT, after washed-out eluted PRMs, and subsequently both eluted through HAC. WT-PD-1 pre-eluted beads have slightly more faint bands than WBT pre-eluted beads, indicating the WT-PD-1 pre-eluted low-binding PRMs while keeping the Higher-affinity PRMs.

After the washing process, the traditional elution method in ribosome display is to denature the ribosome by heating or by adding urea, which is problematic as it is not target-specific. For example, we have observed the anti-His tag binding peptide was enriched under the traditional elution method (data not shown). Moreover, the BMS-1166-PRM eluted through non-specific elution may bind to the non-PD-1 binding epitope of PD-L1 and thus cannot be used as the antagonist. To solve these problems, competitive elution was performed using high-affinity PD-1 variants. It has been reported that competitive elution could effectively reduce the unspecific binding[15] and successfully achieve peptide affinity maturation[16] in the phage display. A high affinity (K_i = 110 pM [14]) PD-1 variant called HAC was chosen for the competitive elution since 10 μM of HAC could theoretically elute more than 99% peptide even if the peptide has a high affinity (K_d = 0.5 nM) with PD-L1 (**Figure 3.3.8.C**). Indeed, the least PCR cycle for visualizing the recovered DNA from eluted PRMs was the same for both elution methods of HAC and urea, indicating that HAC could almost elute the equal amount of BMS-1166-PRMs as urea did. (**Figure 3.3.8B**).

The BMS-1166 originally has an affinity with PD-L1, which means most of the BMS-1166-PRMs may potentially have PD-L1 binding affinity. However, the single elution method could not distinguish the strong binder from the weak binder, resulting in the enrichment of weak PD-L1-binding peptides. To remove the weak PD-L1 binding BMS-1166-PRMs, at 3rd round selection and 4th round selection, a low-affinity PD-1 (K_i = 1.042 μM) of WT-PD-1 was added before HAC to elute the low-affinity BMS-1166-PRMs (**Figure 3.3.8.C**). Furthermore, at 5th round selection, instead of adding WT-PD-1, a middle-affinity PD-1 (K_d = 14.52 nM) of 2-PD-1 was added to firstly eluting both low-affinity BMS-1166-PRMs and middle-affinity BMS-1166-PRMs (**Figure 3.3.8.C**). As shown in **Figure 3.3.8.D, E&F**, the least PCR cycle for visualizing the recovered DNA from eluted PRMs indicated the amount of PRMs eluted by different methods. During the 4th round selection, WT-PD-1 could elute more PRMs than washing buffer (WBT), which theoretically should be the low-affinity BMS-1166-PRMs and the relatively high-affinity BMS-1166-PRMs should remain on the PD-L1 with magnetic beads. Indeed, the subsequential elution with HAC still generated fewer PRMs in the pre-elution of WBT than pre-elution of WT-PD-1, indicating some low-affinity BMS-1166-PRMs were pre-eluted by the WT-PD-1. Besides, the subsequential elution after pre-elution of WT-PD-1 still eluted more BMS-1166-PRMs than WBT elution, indicating the eluted BMS-1166-PRMs contained specific PRMs more than non-specific PRMs. This kind of confirmation was performed for all the selection rounds (data not shown). The DNA recovered from HAC-eluted PRMs was sequenced by NGS and used for the library for the next round of selection.

3.3.4. Principal component analysis for all rounds of selection

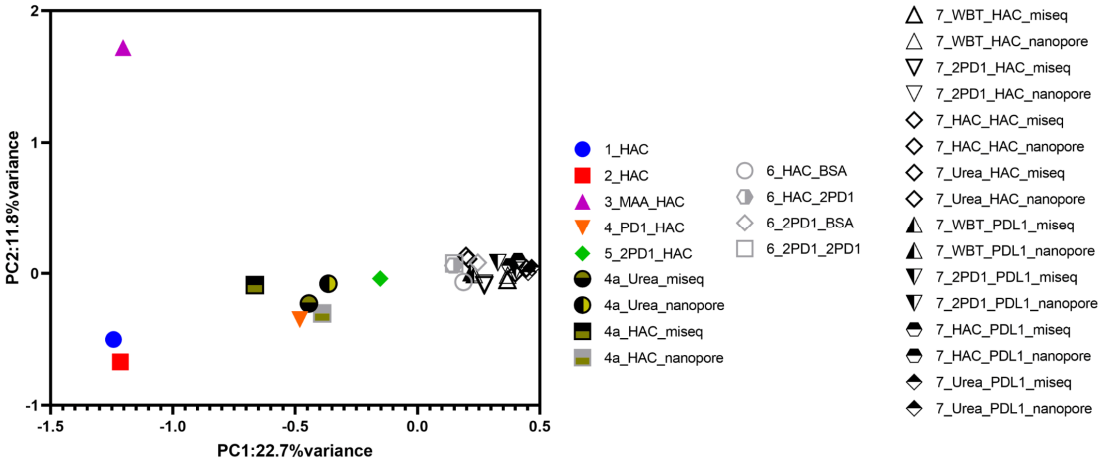

Figure 3.3.9. Principal component analysis for all rounds of selection. Nomenclature of 1st to 5th round selection: “selection-round”_(”pre-elution”)_”final-elution”. Nomenclature of 6th round selection: “selection-round”_”elution-method”_”interference”. Nomenclature of 7th round selection: “selection-round”_’”elution-method”_”selection-target”_”sequencing-method”. Nomenclature of additional 4th round selection: “selection round (4a)”_”final-elution”_”sequencing-method”. The percentage of PC1 and PC2 means the contribution ratio of the two main components to the whole variance.

To visualize the main difference between all NGS samples, principal component analysis (PCA) was performed for all NGS samples using the top two-hundred peptides which had largest standard deviations across the samples. The variance of each NGS sample included the selection round, pre-elution methods, sequencing method, and final-elution method. As shown in **Figure 3.3.9**, the NGS samples were clustered according to their selection rounds, indicating each round of selection was effective to change the count number of top peptides.

3.3.5. Differential binding assay for determining peptide candidates

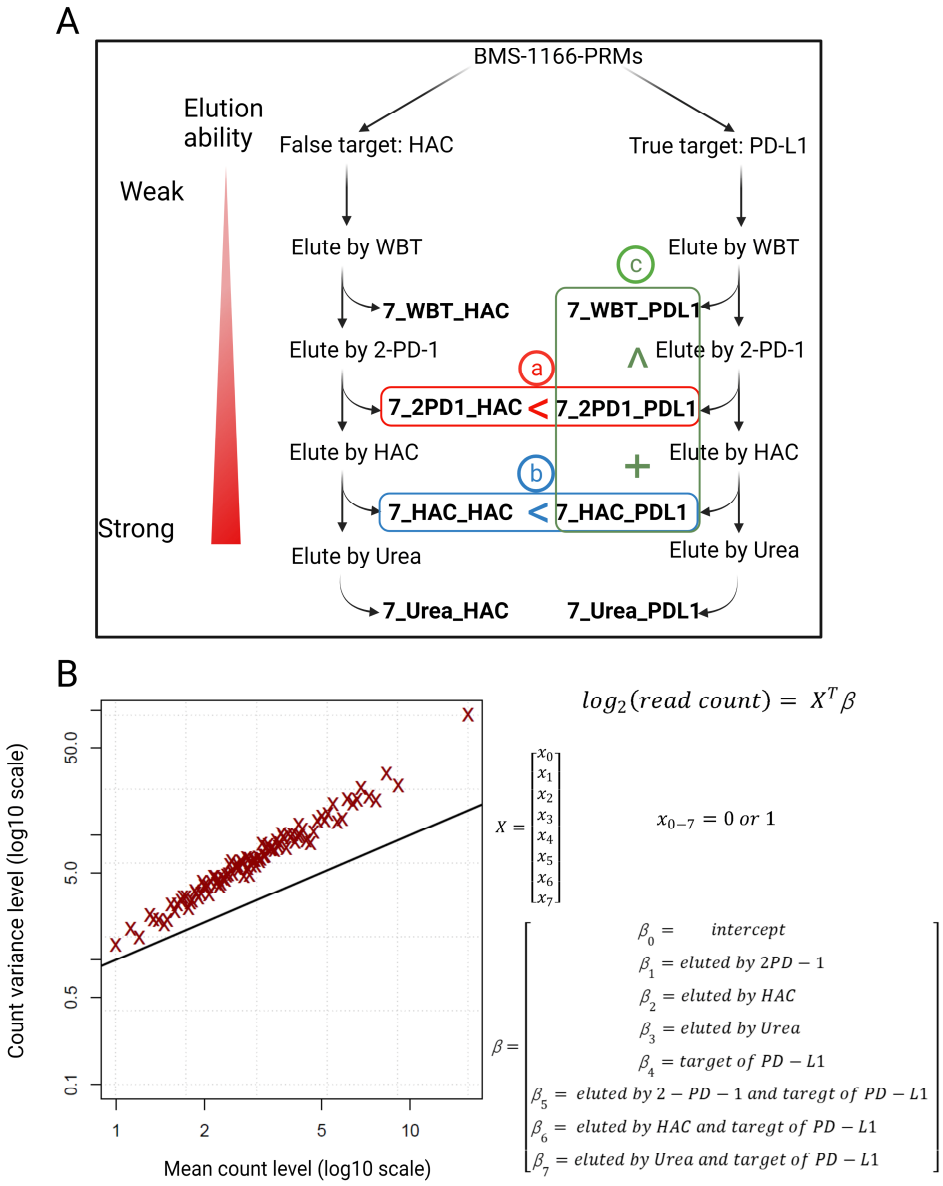

Figure 3.3.10. Differential binding assay design. (A) At the 7th round selection, a differential binding assay was performed by separately incubating the aliquots of BMS-1166-PRMs with either a true target of PD-L1 or a false target of HAC. Sequential elution from weak to strong was performed for both target-bound BMS-1166-PRMs and each resulting NGS library was indicated as the name of "selection-rounds (7)_elution-method_selection-target" in bold type. Three categories of peptides (a, b, and c) that would be determined were indicated on the graph. (B) Mean-variance relationship for all 7th round eluted libraries. The mean-variance of Individual peptide count data was indicated as a red cross. The Poisson mean-variance relationship (mean equals variance) was indicated as the black line. Peptides count data showed a larger variance than the mean, indicating a negative binomial distribution model. The thereafter generalized linear model was indicated at the left side of the graph and was fitted using the read count table as input to give the coefficients (β) of each peptide.

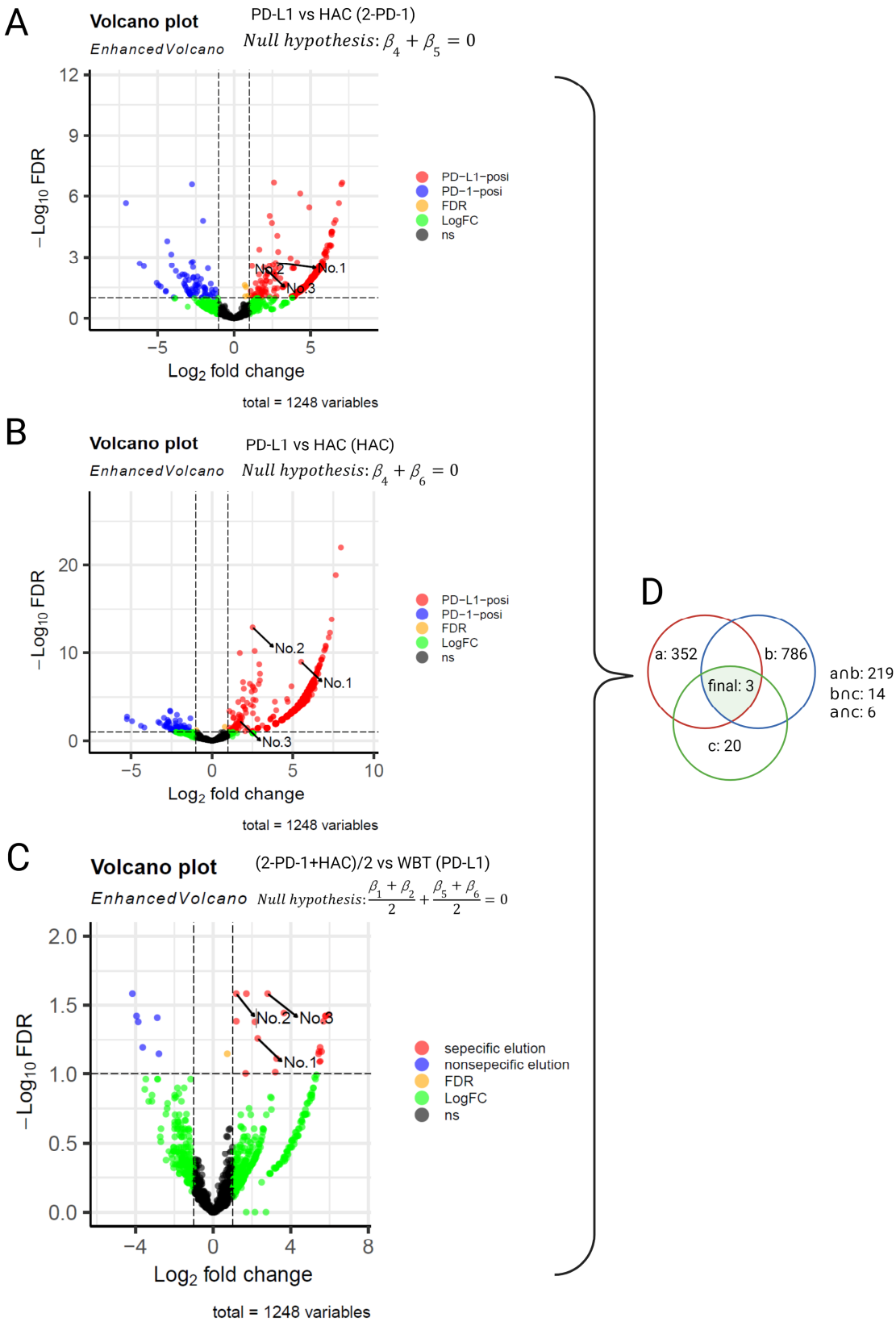

Figure 3.3.11. Data analysis results for the differential binding assay. The different combinations of coefficients could be used to determine different categories of peptides by hypothesis test. Within each

category, hit peptides were determined under the criteria that FDR is less than 0.1 and binary logarithm fold change of read count (Log2 fold change, LogFC) is large than 1. Hit peptides were indicated as red dots in each volcano plot and corresponding legends names changed with categories. As the hypothesis changed (combination of β changed) for each category, the volcano plot also changed. See the **Section 3.2.12. Differential binding analysis** for more explanation. (A) Peptides in the "a " category (PD-L1 vs HAC (2-PD-1)): peptides had more 2-PD-1-elution to the target of PD-L1 than the target of HAC. (B) Peptides in the "b " category (PD-L1 vs HAC (HAC)): peptides had more HAC-elution to the target of PD-L1 than the target of HAC. (C) Peptides in the "c " category ((2-PD-1+HAC)/2 vs HAC (PD-L1)): PD-L1-targeted peptides had more average elution amount with 2-PD-1 and HAC than elution with WBT. (D) The number of induvial peptides that belonged to the three categories. The union of hit peptides within all three categories gave the final three peptides. Other legends in the volcano plot: FDR: FDR is less than 0.1 while LogFC is less than 1. LogFC: LogFC is large than 1 while FDR is large than 0.1. ns: FDR is large than 0.1 while logFC is less than 1.

Since the high-affinity PD-1 of HAC was used to elute the BMS-1166-PRMs, the HAC-binding BMS-1166-PRMs may be eluted during this process. To identify the BMS-1166-PRMs with PD-L1 specificity, the 7th round selection was performed as the differential binding assay by separately incubating the BMS-1166-PRMs with the true target of free PD-L1 or the false target of free HAC. Furthermore, to ensure the inhibitory ability of PD-L1-bound BM1166-PRMs, a sequential elution process including both specific elution method (2-PD-1 and HAC) and non-specific elution method (WBT and urea) was performed for both target-bound BMS-1166-PRMs (**Figure 3.3.10.A**). The recovered DNA from each elution as well as other rounds of DNAs was sequenced through NGS. A duplicate of NGS sequencing was performed for 7th round of recovered DNAs, using two different technologies (Illumina Miseq or Oxford nanopore MinION). In 2021, Pleiko K. et. al successfully used RNAseq analysis software of EdgeR [17] to distinguish the brain-homing peptide from the recovered peptide library from phage display [18], proving that the differential analysis method for RNAseq could be used for analyzing the differential binding profiles of peptide sequences. Besides, the mean-variance relationship of the 7th round of peptide count data (**Figure 3.3.10.B**) also indicated the read count of peptides followed the negative binomial distribution, which was the probability distribution model used in the edgeR. Therefore, edgeR was used to statistically identify the peptides with the desired specificity. See the Section **3.2.12. Differential binding analysis** for the explanation of the mechanism of the edgeR analysis. Three categories of peptides were identified using edgeR under the criteria of FDR < 0.1 and binary logarithm fold change (LogFC) > 1, (a) peptides with more elution to the target of PD-L1 than HAC during the 2-PD-1 elution (**Figure 3.3.11.A**). (b) peptides with more elution to the target of PD-L1 that HAC during the HAC elution (**Figure 3.3.11.B**). (c) PD-L1 bound peptides with more elution to the specific elution (2-PD-1 and HAC) than non-specific elution (WBT) (**Figure 3.3.11.C**). The union of all three categories of hit peptides gave the final three peptide candidates (**Figure 3.3.11.D**).

The Figure 3.3.12 showed the number of the peptide within each category and the union of

all these categories gave three peptide candidates. As shown in **Figure 3.3.12** and **Table 3.3.1,** the three peptides mutually satisfied the above criteria which could theoretically specifically bind to the PD-1 binding domain of PD-L1 as a PD-L1 inhibitor.

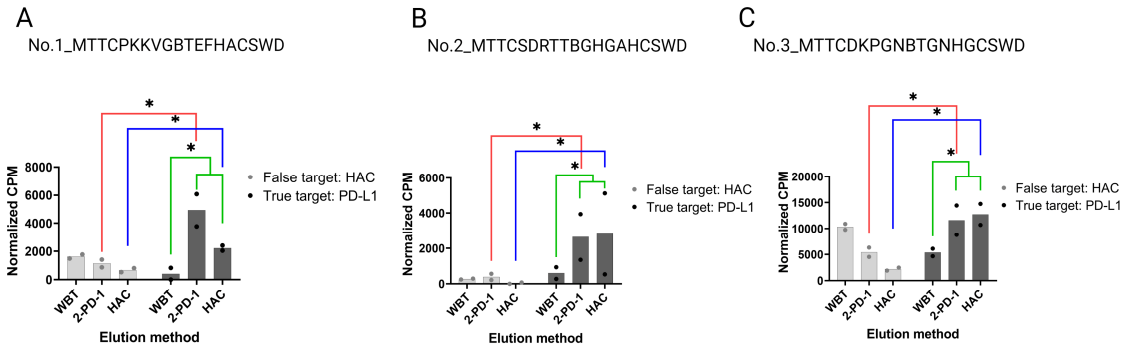

Figure 3.3.12. Normalized read counts of each final peptide candidate in different 7th round selection. (A) Normalized read counts of No.1 peptide candidate in the elution of 7th round selection. (B) Normalized read counts of No.2 peptide candidate in the elution of 7th round selection. (C) Normalized read counts of No.3 peptide candidate in the elution of 7th round selection. * indicated the false-positive rate of the quasi-likelihood F-test is less than 0.1. CPM: count per million. The red color indicated the “a” category, the blue color indicated the “b” category and the green color indicated the “c” category. Black or gray dots indicated the induvial count from two different sequencing results.

Table 3.3.1 Paraments calculated for three peptide candidates.

Peptides	logFC.a	FDR.a	logFC.b	FDR.b	logFC.c	logCPM	FDR.c	Final_FDR
No.1	2.716206	0.001871	5.515514	1.048714×10^{-9}	2.297604	10.67417	0.05492645	0.05669496
No.2	1.172113	0.002743	2.513106	1.333868×10^{-13}	1.193690	13.09279	0.02618700	0.02885806
No.3	1.957359	0.003279	1.723985	6.160893×10^{-3}	2.808928	11.08731	0.02618700	0.03536027

LogCPM: binary logarithm count per million, indicating the average read count of peptide among all 7th round selection library. LogFC: binary logarithm fold change of read count, indicating the read count difference between the specified NGS libraries (a,b and c categories). FDR: individual false discovery rate for three catergories. Final_FDR: overall false discovery rate.

3.3.6. Synthesis of BMS-1166-peptide candidates and activity evaluation

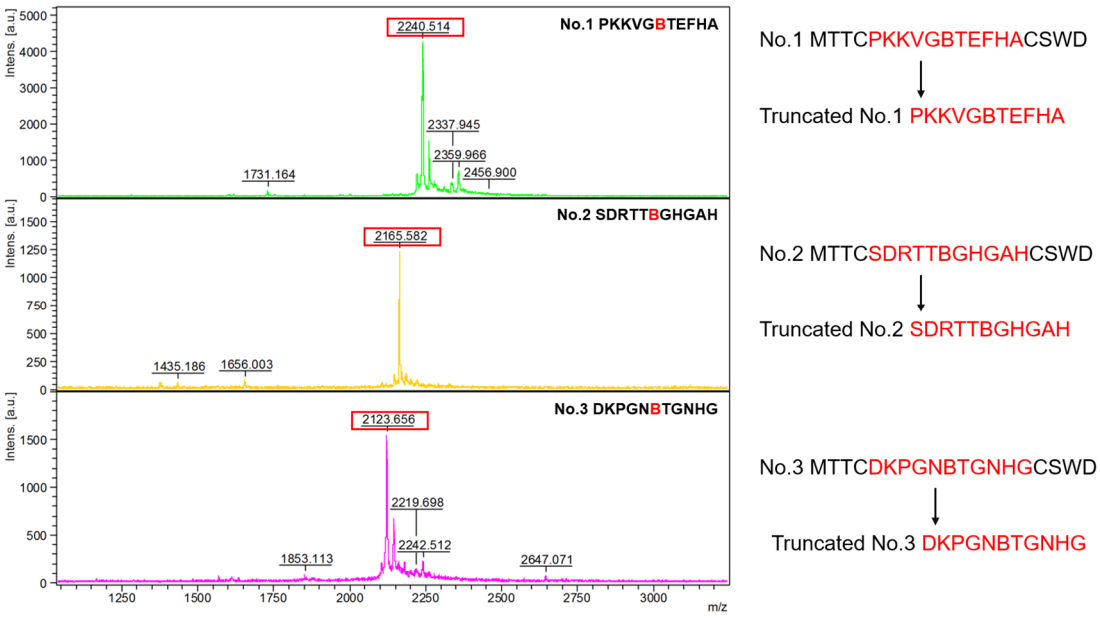

Figure 3.3.13. The MALDI-MS results of synthesized truncated BMS-1166-peptides. The target peak was indicated using a red rectangle. B denoted BMS-1166, conjugated onto BCN-lysine with tetrazine group.

To experimentally verify the activity of candidate BMS1166-peptides, the BMS-1166-peptides were chemically synthesized using a modified solid phase peptide synthesis method[12]. The conserved sequence of the designed peptide library was MTTCxxxxxBxxxxxCSWD (B denotes BMS-1166, and x denotes canonical amino acids). However, the sequences containing MTTC and CSWD showed a bad NHS-BCN coupling yield, possibly due to the side reaction between cysteine and BCN. Therefore, a truncated version of candidate BMS-1166-peptides instead (**Figure 3.3.13**). Besides, the full-length peptides with lysine that substituted the BMS-1166 were also synthesized.

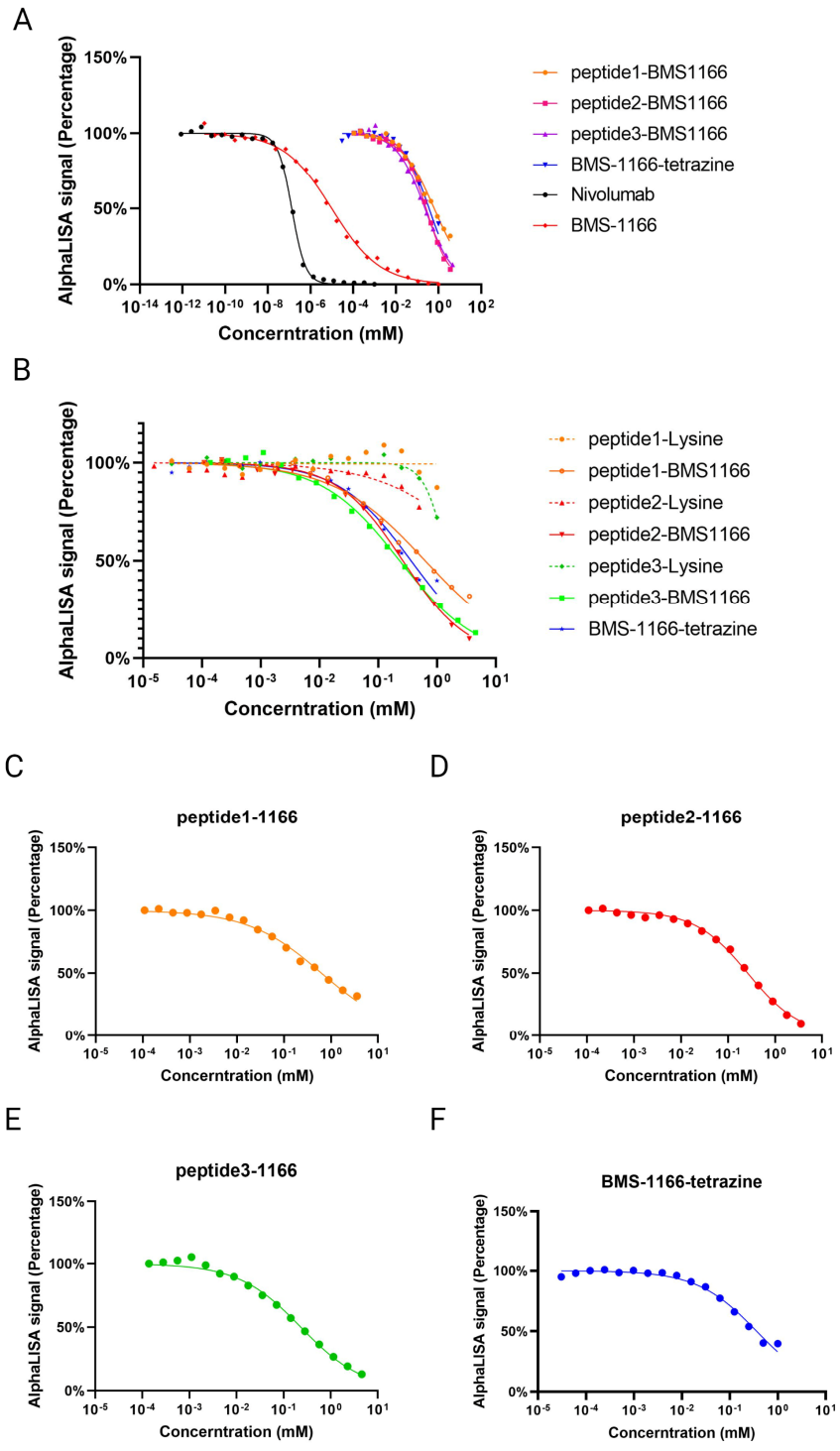

Figure 3.3.14. The inhibition activity for the peptide candidates to interrupt PD-1/PD-L1 interaction. (A) The inhibition curve of BMS-1166-peptide candidates and known SMI of BMS-1166 as well as antibody inhibitor of Nivolumab. (B) The inhibition curve of BMS-1166-peptide candidates and full-length normal lysine peptide candidates. (C) The inhibition curve of No.1 BMS-1166-peptides. (D) The inhibition curve of No.2 BMS-1166-peptides. (E) The inhibition curve of No.3 BMS-1166-peptides. (F) The inhibition curve of BMS-1166-tetrazine.

The *in vitro* activity for the peptide candidates to interrupt PD-1/PD-L1 interaction was measured. As shown in the **Figure 3.3.14.A**, all the BMS-1166-peptides candidates could interrupt PD-1/PD-L1 at high concentrations, while their activity was much weaker than the known inhibitors of BMS-1166 or Nivolumab (**Figure 3.3.14.A** and **Table 3.3.2**). While the peptide3-1166 showed the lowest IC_{50} among all three BMS-1166-peptide candidates. On the other hand, the BMS-1166-peptides exhibited a higher inhibitory effect when compared with their full-length BMS-1166-nonconjugated versions, indicating that the BMS-1166 modification was critical for their activity (**Figure 3.3.14.B**). However, the BMS-1166 modification in this study was achieved using the BMS-1166-tetrazine, which has much lower inhibitory activity than BMS-1166. Therefore, the activity comparison should be focused on the BMS-1166-tetrazine and BMS-1166-peptides. As shown in **Figure 3.3.6** and **Figure 3.3.14.F**, the BMS-1166-tetrazine could only inhibit half of the PD-1/PD-L1 interaction even at the highest concentration, which may be due to the reason of unfavored structure or poor solubility. Interestingly, the BMS-1166-peptide candidates could reach a higher inhibition percentage as well as lower IC_{50} than BMS-1166-tetrazine (**Figure 3.3.14.C, D&E** and **Table 3.3.2**), demonstrating the advantage of SMI-peptide to enhance the activity of SMI. Besides, the IC_{50} difference of the Nivolumab between **Table 2.3.3** and **Table 3.3.2** could be explained by the lot difference between the AlphaLISA Kit as well as the experimental random error.

Table 3.3.2 Absolute IC_{50} deduced from the fitting of dose-dependent inhibition curve by constraining the top of curve at 100 and bottom of curve at 0.

Samples	Absolute IC_{50} (nM)	95% CI of IC_{50} (nM)
BMS-1166	9.93	7.99 to 1.24×10
Nivolumab	1.33×10^{-1}	1.21×10^{-1} to 1.46×10^{-1}
peptide1-1166	6.32×10^{5}	5.34×10^{5} to 7.54×10^{5}
peptide2-1166	2.64×10^{5}	2.41×10^{5} to 2.89×10^{5}
peptide3-1166	2.33×10^{5}	1.99×10^{5} to 2.72×10^{5}
BMS-1166-tetrazine	3.64×10^{5}	3.02×10^{5} to 4.45×10^{5}

IC_{50}: Half maximal inhibitory concentration; CI: Confidence interval.

3.4. Discussion and conclusion

In this Chapter, the development of the peptide ICIs was described. The development method successfully combined the click-chemistry with ribosome display and was strictly verified by the demo selection, greatly expanding the application of the general ribosome display method. Besides, the real selection has been carefully designed to decrease the non-specific binding and ensure strong PD-L1 inhibitory binding of the selected peptides. Furthermore, by using a differential binding assay at the final selection and combining it with the statistical analysis, the peptide candidate is determined under statistical significance which is more reasonable and repeatable. The binding ability of peptide candidates with PD-L1 had been indicated by the high accuracy *in silico* modeling. The BMS-1166-peptide candidates showed a superior PD-1/PD-L1 inhibitory effect than the key molecular of BMS-1166-tetrazine, demonstrating the advantage of SMI-peptides. This improved activity may be benefited from their improved water-solubility or mechanism reasons. However, the current BMS-1166-peptides remained much weaker than the antibodies or BMS-1166. One of the reasons was that the activity of the key molecular of BMS-1166-tetrazine was much lower than that of BMS-1166. Therefore, the selected peptide sequence could not fully remedy the activity loss of BMS-1166-tetrazine caused by the tetrazine modification. Moreover, since the current BMS-1166-peptides were a truncated peptide without the conserved sequence of MTTC and CSWD, the cysteine or other residues within the conserved sequence may be critical for the activity and thus cause the unexpected weak affinity. As further works, the structure of BMS-1166-tetrazine needs to be optimized to obtain similar inhibitory activity as BMS-1166, and the synthesis method of full-length BCN-peptide needs to be investigated.

Reference

1. Packer, M. S. & Liu, D. R. Methods for the directed evolution of proteins. *Nature Reviews Genetics* vol. 16 379–394 Preprint at https://doi.org/10.1038/nrg3927 (2015).
2. Alfaleh, M. A. *et al.* Phage Display Derived Monoclonal Antibodies: From Bench to Bedside. *Frontiers in Immunology* vol. 11 Preprint at https://doi.org/10.3389/fimmu.2020.01986 (2020).
3. Mattheakis, L. C., Bhatt, R. R. & Dower, W. J. An in vitro polysome display system for identifying ligands from very large peptide libraries. *Proceedings of the National Academy of Sciences* **91**, 9022–9026 (1994).
4. Zhang, J. *et al.* Mechanisms of ribosome stalling by SecM at multiple elongation steps. *Elife* **4**, e09684 (2015).
5. Katoh, T. & Suga, H. In Vitro Genetic Code Reprogramming for the Expansion of Usable Noncanonical Amino Acids. *Annu Rev Biochem* **91**, 221–243 (2022).
6. Lang, K. *et al.* Genetic Encoding of Bicyclononynes and trans-Cyclooctenes for Site-Specific Protein Labeling in Vitro and in Live Mammalian Cells via Rapid Fluorogenic Diels–Alder Reactions. *J Am Chem Soc* **134**, 10317–10320 (2012).
7. Wang, H. & Liu, R. Advantages of mRNA display selections over other selection techniques for investigation of protein-protein interactions. *Expert Rev Proteomics* **8**, 335–346 (2011).
8. Oliveira, B. L., Guo, Z. & Bernardes, G. J. L. Inverse electron demand Diels–Alder reactions in chemical biology. *Chem Soc Rev* **46**, 4895–4950 (2017).
9. Olins, P. O. & Rangwala, S. H. A Novel Sequence Element Derived from Bacteriophage T7 mRNA Acts as an Enhancer of Translation of the lacZ Gene in Escherichia coli. *Journal of Biological Chemistry* **264**, 16973–16976 (1989).
10. Nakamura, T. *et al.* Tertiary Structure and Carbohydrate Recognition by the Chitin-Binding Domain of a Hyperthermophilic Chitinase from Pyrococcus furiosus. *J Mol Biol* **381**, 670–680 (2008).
11. Robinson, M. D., McCarthy, D. J. & Smyth, G. K. edgeR: a Bioconductor package for differential expression analysis of digital gene expression data. *Bioinformatics* **26**, 139–140 (2010).
12. La–Venia, A., Dzijak, R., Rampmaier, R. & Vrabel, M. An Optimized Protocol for the Synthesis of Peptides Containing trans-Cyclooctene and Bicyclononyne Dienophiles as Useful Multifunctional Bioorthogonal Probes. *Chemistry - A European Journal* **27**, 13632–13641 (2021).
13. Karver, M. R., Weissleder, R. & Hilderbrand, S. A. Synthesis and Evaluation of a Series of 1,2,4,5-Tetrazines for Bioorthogonal Conjugation. *Bioconjug Chem* **22**, 2263–2270 (2011).
14. Maute, R. L. *et al.* Engineering high-affinity PD-1 variants for optimized immunotherapy and immuno-PET imaging. *Proc Natl Acad Sci U S A* **112**, E6506–E6514 (2015).
15. Duan, Z. & Siegumfeldt, H. An Efficient Method for Isolating Antibody Fragments Against Small Peptides by Antibody Phage Display. *Comb Chem High Throughput Screen* **999**, 1–11 (2010).
16. Kabir, M. E., Krishnaswamy, S., Miyamoto, M., Furuichi, Y. & Komiyama, T. An improved

phage-display panning method to produce an HM-1 killer toxin anti-idiotypic antibody. *BMC Biotechnol* **9**, (2009).

17. Robinson, M. D., McCarthy, D. J. & Smyth, G. K. edgeR: a Bioconductor package for differential expression analysis of digital gene expression data. *Bioinformatics* **26**, 139–140 (2010).
18. Pleiko, K. *et al.* In vivo phage display: identification of organ-specific peptides using deep sequencing and differential profiling across tissues. *Nucleic Acids Res* **49**, e38–e38 (2021).

Chapter IV | Development of the SMI Conjugated Dendrimer Inhibitor

4.1. Introduction

The SMI-peptide increased the activity of SMI by enhancing its protein contact area through an additional peptide chain, while the SMI-peptide itself remained to be a monovalent inhibitor. As an alternative strategy, SMI could be multiply immobilized onto a polymer to develop polymer ICIs through the multivalency effect.

The multivalency effect is also referred to as avidity, it describes the phenomenon that when a compound is composed of multiple target-binding units, its binding ability will become synergically higher than a compound with only a single target-binding unit. This phenomenon has already been observed in both polymers[1] and antibodies[2]. Statistical rebinding has been suggested as one of the mechanisms for the multivalency effect[1]. For a multivalent compound, once one of the target-binding units dissociates from the target, other adjacent target-binding units could bind to the target in a more energy-efficient manner than the free target-binding unit. Besides, as the PD-L1 is multiply expressed on various cells, including the tumor cell, a chelation mechanism with favorable entropy term between a multivalent compound and multiple targets could further enhance the multivalency effect[1,3]. Moreover, it has been reported that a multivalent peptide inhibitor conjugated polymer ICI inhibited the PD-L1 recycling via surface PD-L1 crosslinking, exhibiting a prolonged PD-L1 blockade effect[4].

Therefore, in this chapter, the development of the SMI conjugated polymer inhibitor was described. Since the SMI has a 150-times lower molecular weight compared to the antibody, the molecular weight of a multivalently SMI-modified polymer would still be smaller than the antibody and thus has better tumor penetration than the antibody. As a demonstration of the idea, BMS-1166 was chosen as the SMI since it has a relatively high activity and low cytotoxicity. On the other hand, the generation 4 poly(amidoamine) (PAMAM-G4) was chosen as the polymer since it contains sixty-four surface amines which could be immobilized with BMS-1166 to give the PAMAMG4-BMS1166.

4.2. Materials & Methods

4.2.1. Materials

PAMAM-G4 was purchased from Sigma-Aldrich (USA), BMS-1166 was purchased from DC Chemical (China). All other reagents used for the synthesis of PAMAM G4-BMS1166 were purchased from the Fujifilm Wako Pure chemical corporation (Japan) or Tokyo Chemical Industry (Japan).

4.2.2. Synthesize of the PAMAMG4-BMS1166

BMS-1166 (6 mg, 9.9 μmol), 1-(3-Dimethylaminopropyl)-3-ethylcarbodiimide Hydrochloride (EDC·HCl, 1.89 mg, 9.9 μmol) and 1-hydroxybenzotriazole (HOBt, 1.5 mg, 9.9 μmol) were dissolved in 3 mL Dimethyl Sulfoxide (Super Dehydrated). After stirring for 30 min under the N_2 gas protection, PAMAM-G4 (3.75 mg, 0.264 μmol) and N,N-diisopropylethylamine (DIPEA, 2.23 μL, 13.2 μmol) were added into the above solution. After stirring at 35°C for 72 h under the N2 gas protection, the solvent was removed by lyophilization. The product was redissolved into 2.5 mL H_2O and purified through the PD-10 column. The collected solution was lyophilized to give the final product.

4.2.3. Structure characterization of PAMAM-BMS1166

For the ^{1}H-NMR measurement, PAMAM-G4 and PAMAMG4-BMS1166 were dissolved into the Deuterated methanol (CD_3OD) and measured by JNM-ECZ400R (JEOL, Japan). For the MALDI-MS measurement, lyophilized PAMAMG4-BMS1166 power was sent to the Support unit for Bio-Material Analysis of RIKEN, and measurement was performed by technique staff. 2,5-Dihydroxybenzoic Acid (DHB) was used as the matrix. UV measurements were conducted using the UV-Visible spectrophotometer of V-750 (JASCO, Japan)

4.2.4. PD-1/PD-L1 Inhibitory assay

The experimental process is similar to the description in the 3.2.14. PAMAM-G4, BMS-1166, and PAMAMG4-BMS1166 were dissolved in the DMSO solution to give the 100% DMSO stock solution. Stock solutions were then mixed with 10X assay buffer and volume up by H_2O to give the 40% DMSO 1X assay buffer starting solution. Serial dilutions of inhibitor were prepared using 1X assay buffer (40% DMSO). 6.67 nM of PD-L1-His tag, 6.67 nM of biotinylated PD-1, 26.67 μg/mL of streptavidin Donor beads, 13.33 μg/mL of anti-His tag Acceptor beads (all provided within the Kit) were prepared by dissolving in the 1X assay buffer and added to 384-well plate (ProxiPlate, PerkinElmer, USA) at 6 μL/well under dark environment. Serial dilutions of samples were added into the wells at 2 μL/well to give the final concentration of DMSO at 10%. After incubating at room temperature for 90 mins in dark

environments, the AlphaLISA signal of each well was measured by the plate reader (EnSpire™, PerkinElmer, USA). After normalizing the signal with the well without adding the samples, the plots were fitted using the “[inhibitor] vs. normalized response” function of the GraphPad Prism software.

4.3. Results

4.3.1. Synthesis of PAMAMG4-BMS1166

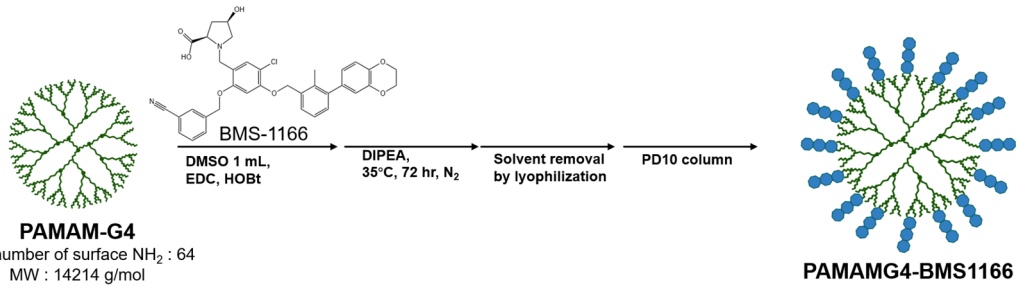

Figure 4.3.1. The synthesis scheme of PAMAMG4-BMS1166.

Since the hydrophilic tail of BMS-1166 contains the carboxyl acid group, a similar synthesis scheme of BMS-1166-tetrazine was used for the coupling of BMS-1166 to PAMAM-G4 using the HOBt-mediated amide formation (**Figure 4.3.1**). Since the PAMAM-G4 contains sixty-four surface amines, the molar ratio of PAMAM-G4 to BMS-1166 was set as 1 to 37. After coupling, an improved water solubility was observed for the PAMAMG4-BMS1166 as the free BMS-1166 is not dissolved in water. Finally, the uncoupled small molecular of BMS-1166 was removed by the desalting column of PD-10.

4.3.2. Structural characterization of PAMAMG4-BMS1166

To confirm the successful synthesis of PAMAMG4-BMS1166, UV-Vis spectrometry, ^{1}H-NMR, and MALDI-MS were used to characterize the structure. BMS-1166 contains several aryl groups which the PAMAM-G4 does not have. Besides, as the BMS-1166 had been removed through the PD-10 desalting column, the aryl-originated peaks observed from the purified product of PAMAMG4-BMS1166 could be considered as the origin from the conjugated BMS-1166. As shown in **Figure 4.3.2.A**, the PAMAMG4-BMS-1166 showed a similar UV absorption pattern as the BMS-1166 with a peak around 300 nm wavelength, while the non-conjugated PAMAM-G4 did not show. Moreover, in the ^{1}H-NMR results (**Figure 4.3.2.C&D**), the PAMAMG4-BMS-1166 showed a characterized aryl-originated chemical shift around 6~7 ppm, which could not be observed in the ^{1}H-NMR results of PAMAM-G4. Moreover, the MALDI-MS results of PAMAMG4-BMS1166 showed that it has an average molecular weight of around 24,019 g/mol (**Figure 4.3.2.B**). As it has been reported that the molecular weight of PAMAM-G4 is 14,214 g/mol [5], the increased molecular weight could be considered as the conjugated BMS-1166. Therefore, the average number of BMS-1166 conjugated onto the PAMAM-G4 should be around fifteen, which indicated 23% surface amine was coupled with BMS-1166. Overall, all the results indicated that the PAMAMG4-BMS1166 was successfully synthesized.

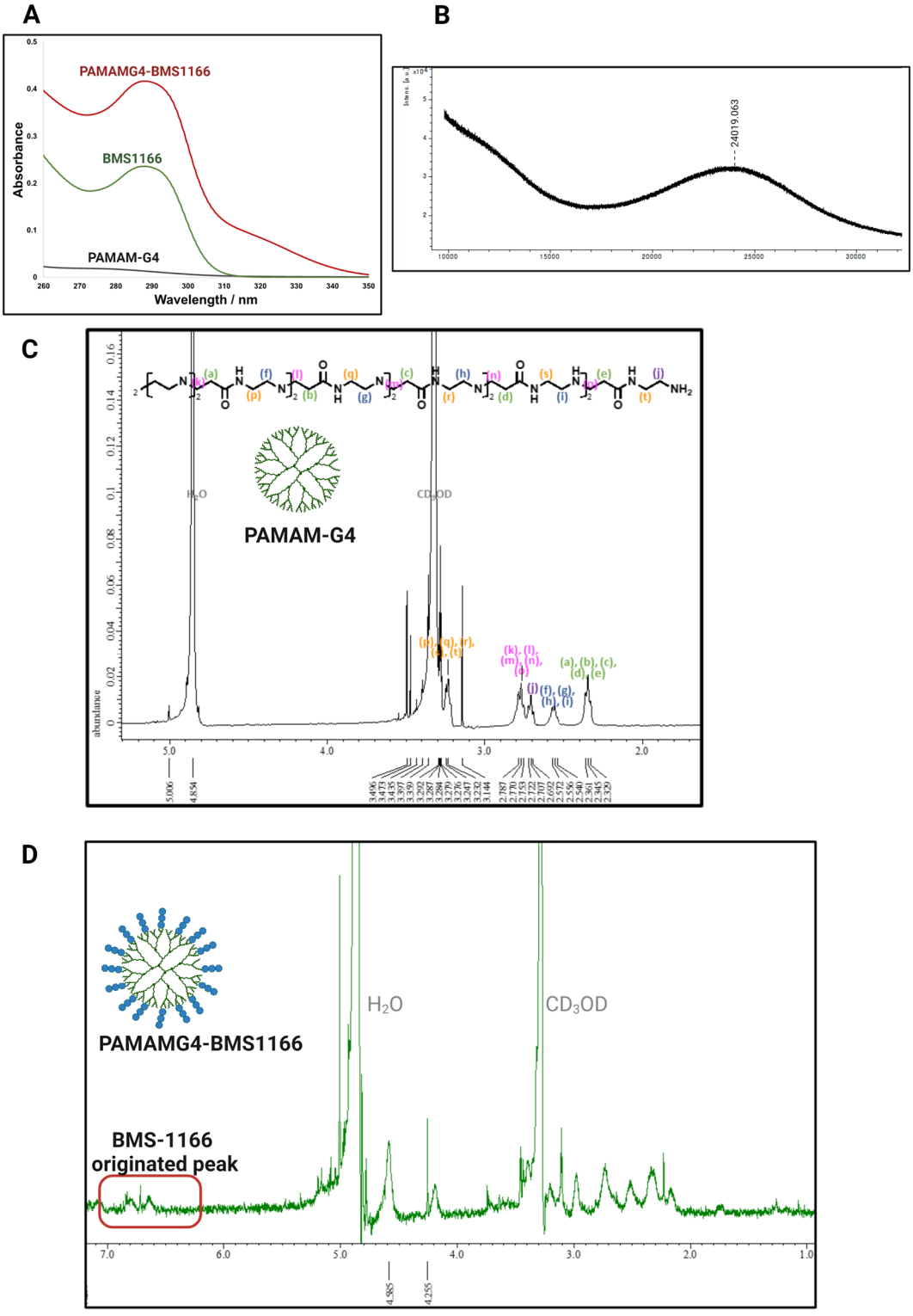

Figure 4.3.2. Structural characterization of PAMAMG4-BMS1166. (A) UV-Vis spectrometry results of three compounds. (B) MALDI-MS of PAMAG4-BMS1166. (C) ^{1}H-NMR result of PAMAM-G4. Assigned peaks are indicated on the graph. (D) ^{1}H-NMR result of PAMAMG4-BMS1166. The BMS-1166-originated chemical shift peaks were indicated in the graph.

4.3.3. PD-1/PD-L1 Inhibitory assay for PAMAMG4-BMS1166

PD-1/PD-L1 inhibitory assay was performed to confirm the inhibitory effect and multivalency effect of the PAMAMG4-BMS1166. As shown in **Figure 4.3.3** and **Table 4.3.1**, PAMAMG4-BMS1166 could inhibit the interaction between PD-1 and PD-L1, with the IC_{50} equivalent to the commercial antibody. However, the IC_{50} of PAMAMG4-BMS1166 had no improvement when compared to the free SMI of BMS-1166. This phenomenon may be due to the conjugation of BMS-1166 inducing the steric hindrance that decreased its inhibitory effect, as shown for the BMS-1166-tetrazine (**Figure 3.3.4.D**) and the multivalency effect remedied this decreased inhibitory effect so that the PAMAMG4-BMS1166 showed similar inhibitory effect with BMS-1166.

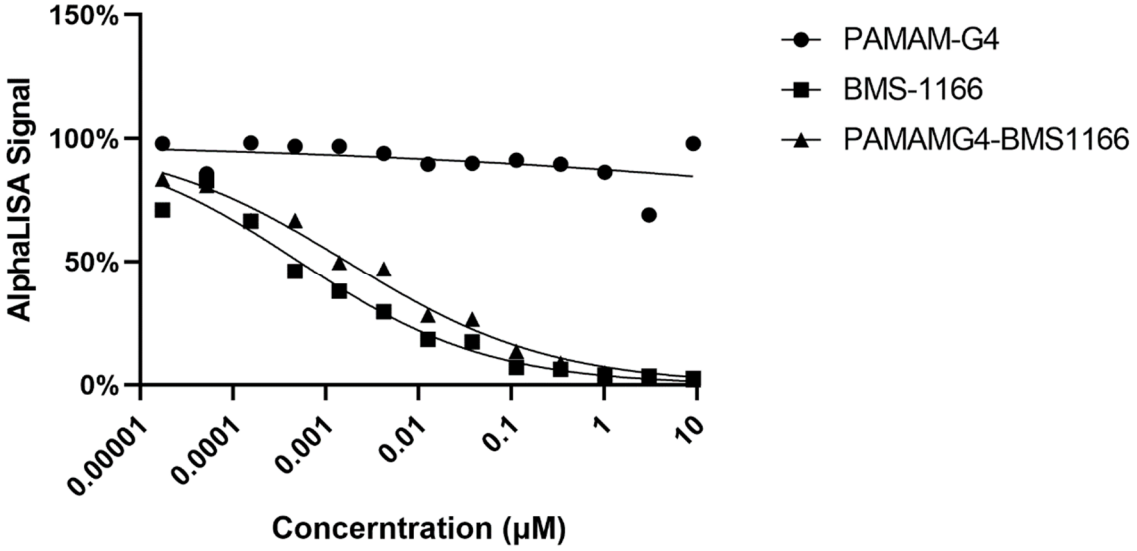

Figure 4.3.3. Dose-dependent inhibition curve for PAMAM-G4, BMS-1166, and PAMAMG4-BMS1166 to inhibit the PD-1/PD-L1 interaction.

Table 4.3.1. IC_{50} deduced from the fitting of the dose-dependent inhibition curve

Samples	IC_{50} (nM)	95% CI of IC_{50} (nM)
PAMAMG4	N.D.	N.D.
BMS-1166	0.519	0.326 to 0.810
PAMAMG4-BMS1166	1.71	1.22 to 2.36
Nivolumab**	1.86	1.57 to 2.21

**: Data reused from Chapter2

N.D.: Failed to calculate IC_{50} because no inhibition effect

4.4. Discussion and conclusion

In this Chapter, the development of the SMI-conjugated dendrimer ICI was described. The design concept was to utilize the multivalency effect to convert SMI to a more potent dendrimer ICI. By using the sixty-four surface amines containing PAMAM-G4 as the dendrimer, a high conjugation number of an average fifteen BMS-1166 per dendrimer was achieved. Several structural characterization methods were used to confirm the successful synthesis of PAMAMG4-BMS1166. Owning to the small size of BMS-1166, the total molecular weight of PAMAMG4-BMS1166 was still more than 7-times lower than the antibody. The PAMAMG4-BMS1166 exhibited equivalent *in vitro* PD-1/PD-L1 inhibition effect as the commercial antibody, indicating it has enough inhibition effect as the ICI. However, as there was no linker between the BMS-1166 and PAMAM-G4, the conjugation itself would be highly possible to decrease the inhibitory effect of the conjugated BMS-1166 due to steric hindrance. Therefore, the PAMAMG4-BMS-1166 did not show a higher inhibition effect than the free BMS-1166. This could be solved by adding the flexible linker or increasing the conjugation number of BMS-1166 to the dendrimer.

Reference

(1) Li, J.; Yu, F.; Chen, Y.; Oupický, D. Polymeric Drugs: Advances in the Development of Pharmacologically Active Polymers. *Journal of Controlled Release* **2015**, *219*, 369–382. https://doi.org/10.1016/j.jconrel.2015.09.043.

(2) Oostindie, S. C.; Lazar, G. A.; Schuurman, J.; Parren, P. W. H. I. Avidity in Antibody Effector Functions and Biotherapeutic Drug Design. *Nature Reviews Drug Discovery*. Nature Research October 1, 2022, pp 715–735. https://doi.org/10.1038/s41573-022-00501-8.

(3) Kitov, P. I.; Bundle, D. R. On the Nature of the Multivalency Effect: A Thermodynamic Model. *J Am Chem Soc* **2003**, *125* (52), 16271–16284. https://doi.org/10.1021/ja038223n.

(4) Li, L.; Li, Y.; Yang, C.-H.; Radford, D. C.; Wang, J.; Janát-Amsbury, M.; Kopeček, J.; Yang, J. Inhibition of Immunosuppressive Tumors by Polymer-Assisted Inductions of Immunogenic Cell Death and Multivalent PD-L1 Crosslinking. *Adv Funct Mater* **2020**, *30* (12), 1908961. https://doi.org/https://doi.org/10.1002/adfm.201908961.

(5) Flores-Mejía, R.; Fragoso-Vázquez, M. J.; Pérez-Blas, L. G.; Parra-Barrera, A.; Hernández-Castro, S. S.; Estrada-Pérez, A. R.; Rodrígues, J.; Lara-Padilla, E.; Ortiz-Morales, A.; Correa-Basurto, J. Chemical Characterization (LC–MS–ESI), Cytotoxic Activity and Intracellular Localization of PAMAM G4 in Leukemia Cells. *Sci Rep* **2021**, *11* (1), 8210. https://doi.org/10.1038/s41598-021-87560-w.

Chapter V | Conclusion and Prospects

5.1. Conclusion

ICIs have achieved unprecedented anti-cancer therapeutic effects by blocking the PD-1/PD-L1 interaction to reactivate T-cells. Current antibody ICI has several problems: First, its long serum elimination time extends the inevitable immune-related adverse effect; Second, its high molecular weight decreases its tumor distribution amount and thus compromises its therapeutic effect; Third, its high manufacturing cost decreases the affordable number of patients. For providing a better ICI than antibody, several non-antibody ICIs have been reported. However, the low bioactivity, immunogenicity, and cytotoxicity limit their therapeutic effect. This thesis attempted to develop three improved non-antibody ICIs by using novel methods.

In Chapter2, a combined method of *in silico* mutagenesis and in-cell verification was designed and applied to obtain the protein ICI of 2-PD-1. 2-PD-1 was 10-times smaller than the current antibody and had only two point-mutations of the wild-type PD-1, which theoretically should have a better tumor penetration and low immunogenicity. As for the bioactivity, 2-PD-1 showed about 100-times more enhancement than WT-PD-1, while its bioactivity was about 50-times weaker than the bivalent antibodies.

In Chapter3, for achieving a higher inhibitory activity and specificity than SMI or peptide ICI, SMI was designed to be conjugated with peptide as SMI-peptide. A combined method of ribosome display and click-chemistry was designed to biosynthesize a library composed of billions of SMI-peptide/ribosome/mRNA complexes. A demo selection verified this method by using FAM as SMI and observing the FAM-peptide coding sequencing could be specifically enriched by anti-FAM magnetic beads. The selection of SMI-peptide was performed by using BMS-1166 as SMI and selecting a random SMI-peptide library against the PD-L1. After 7^{th} round of selection, three PD-L1 specific BMS-1166-peptides candidates were statistically determined from a differential binding experiment. Three truncated BMS-1166-peptide candidates were chemically synthesized using a modified solid-phase peptide synthesis method. All three BMS-1166-peptides showed the inhibitory effect for the PD-1/PD-L1 interaction, and peptide3-BMS1166 showed the lowest IC_{50} among all three peptides. Besides, all the BMS-1166-peptides exhibited a superior inhibitory effect than the key molecular of BMS-1166-tetrazine, proving the effectiveness of the SMI-peptide strategy. However, the current BMS-1166-peptides were much weaker than the BMS-1166, which may be due to the limited activity of BMS-1166-tetrazine or the loss of critical residues of truncated BMS-1166-peptides.

In Chapter4, to utilize the multivalency effect for developing a more potent ICI, multiple small molecular inhibitors of BMS-1166 were conjugated onto a single dendrimer of PAMAM-G4 to

form the PAMAMG4-BMS1166. PAMAMG4-BMS1166 had an average conjugation number of fifteen BMS-1166 and had a 7-times smaller molecular weight than the antibody. Due to unfavorable steric hindrance, PAMAMG4-BMS1166 showed an equivalent PD-1/PD-L1 inhibitory ability as the antibody ICI and SMI but did not reach a higher inhibitory effect as expected.

The development methods combined the recent advanced techniques and were general that could be furtherly used to develop other inhibitors for other targets. Specifically, the development method of 2-PD-1 was a combination of *in silico* mutagenesis and in cell verification, which had the advantage of high-throughput and high accuracy. This method could be further used for developing high-affinity protein mutants based on the known crystal structure. On the other hand, the development method of SMI-peptide combined the ribosome display with click-chemistry, which achieves the biosynthesis of random SMI-peptides/ribosome/mRNA complexes for their selection to the specific target. Any tetrazine modified molecular could be theoretically biosynthesized as peptide-molecular conjugates for their selection. For example, the molecular could be a fluorescent dye of 4-N,N-dimethylamino-1,8-naphthalimide[1], a polymerization initiator of 3,4-ethylenedioxythiophene[2] or a metal binding molecular of L-3,4-dihydroxyphenylalanine (L-DOPA)[3].

5.2. Prospects

Since the currently developed ICIs were not potent enough to provide a higher therapeutic effect than antibody ICIs, further investigation is needed to enhance their activity. In Chapter2, the inhibition activity of 2-PD-1 is still weaker than the current antibodies. Since 2-PD-1 is a monovalent ICI while antibodies are bivalent ICIs, 2-PD-1 can be dimerized to provide higher inhibition activity and bioactivity. This strategy has been reported in the development of the PD-L1 blocking DARPin® Protein[4], as the dimerization of monovalent DARPin-1 through a linker created the bivalent DARPin-2 and showed about 30-fold bioactivity improvements. Besides, in Chapter3 and Chapter4, the amine modification of the carboxylic acid group of the BMS-1166 showed a decrease in the inhibitory activity. A similar phenomenon has been recently reported as the modification of the carboxylic acid group within the BMS-1166 with amine-derived pomalidomide greatly dropped the activity of the modified BMS-1166[5]. Since the carboxylic acid group of BMS-1166 interacts with the K124 of PD-L1[6], the modification may abolish the interaction between BMS-1166 and PD-L1. A flexible linker can be added to BMS-1166 and its conjugates to remove the unfavorable steric hindrance for enhancing their inhibitory effect. Alternatively, the BMS-202 could be modified instead of BMS-1166, as the 3-substitution of the pyridine group within the BMS-202 with methylamine-derivates successfully maintained the inhibition activity of BMS-202[5].

The other problem in this study is the difficulty of the chemical synthesis for the full-length BMS-1166-peptides. The first reason is that the intermediates of BCN-peptides were unstable under TFA-cleavage conditions during the traditional automatic Fmoc-based solid phase peptide synthesis. And the second reason is the low yield during the NHS-BCN coupling onto the lysine within the full-length peptides. As the unwanted side-reaction between BCN and cysteine partially explained the second reason, it has been suggested that adding the β-mercaptoethanol into the reaction solution may reduce the side-reaction[7]. Alternatively, the synthesis of BMS-1166-peptide may be achieved through the click reaction between tetrazine-peptide and BCN-BMS-1166. Firstly, it has been reported that tetrazine-containing amino acids could be incorporated into proteins using the *E.coli* expression system[8], which ensures the *in vitro* biosynthesis of the tetrazine-peptide. Besides, the tetrazine-peptide could be directly chemically synthesized using the Boc-chemistry solid phase peptide synthesis[9] and thus avoids the later coupling process as in the case of BCN-peptide. However, the Boc-chemistry needs the strong acid of anhydrous hydrogen fluoride for the cleavage of the peptide from resin and side-chain deprotection, which is highly toxic and needs special protection[10].

Recently artificial intelligence (AI) has been applied to pharmaceutical research and can be furtherly integrated with the methods developed in this thesis. In Chapter2, the prerequisite for the *in silico* mutagenesis is the known crystal structure of the protein/ligand complex. However, it is not easy to obtain the high-resolution crystal structure as the difficulty in protein

crystallization[11]. Recently, the AI-based protein modeling software of AlphaFold2 achieved extremely high accuracy and resolution with only the input of amino acid sequence[12]. Therefore, the developed method in Chapter2 can combine with AlphaFold2 to discover the high-affinity mutant for a protein without the experimentally determined structure. On the other hand, Chapter3 specially designed 7th round selection and used the NGS data for statistics-based differentially binding analysis to determine the PD-L1-specific BMS-1166 peptide candidates. It has been recently reported that the NGS data of the target-binding peptides could be used for training the AI model for designing stronger target-binding peptides[13,14]. However, the target-binding peptides used for training AI-model were determined simply based on the enrichment ratio[13] or even high-count number sequence[14], which contained high experimental noise and limit the performance of the trained AI model. The statistics-based determination of target-binding peptide used in Chapter3 could remove the experimental noise and therefore potentially provide better peptide candidates input for training the AI models. Moreover, it has been recently reported that the sequencing data could be used for the prediction of absolute K_d value using an interpretable machine learning model[15]. The gradient elution method with different affinity PD-1 variants used in Chapter3 can be combined with this model and provide a more accurate interpretation of K_d.

As demonstrated in Chapter4, the multiple modifications of BMS-1166 on the dendrimer of PAMAM-G4 could provide a multivalency-enhanced therapeutic effect. The monovalent ICIs developed in Chapter2 and Chapter3 could be furtherly modified onto the PAMAM-G4 for a higher therapeutic effect as well. Furthermore, compared to the BMS-1166 whose activity is easy to be decreased by steric hindrance, the relatively large size of biomolecules offers higher structure flexibility that may be more suitable for the multiple modifications on the PAMAM-G4.

Reference

(1) Wang, W.; Zhu, L.; Hirano, Y.; Kariminavargani, M.; Tada, S.; Zhang, G.; Uzawa, T.; Zhang, D.; Hirose, T.; Taiji, M.; Ito, Y. Fluorogenic Enhancement of an in Vitro-Selected Peptide Ligand by Replacement of a Fluorescent Group. *Anal Chem* **2016**, *88* (16), 7991–7997. https://doi.org/10.1021/acs.analchem.6b01032.

(2) K. C., T. B.; Tada, S.; Zhu, L.; Uzawa, T.; Minagawa, N.; Luo, S.-C.; Zhao, H.; Yu, H.; Aigaki, T.; Ito, Y. In Vitro Selection of Electrochemical Peptide Probes Using Bioorthogonal TRNA for Influenza Virus Detection. *Chemical Communications* **2018**, *54* (41), 5201–5204. https://doi.org/10.1039/C8CC01775A.

(3) Zhu, W.; Chen, L.; Wu, Z.; Li, W.; Liu, X.; Wang, Y.; Guo, M.; Ito, Y.; Wang, L.; Zhang, P.; Wang, H. Bioorthogonal DOPA-NGF Activated Tissue Engineering Microunits for Recovery from Traumatic Brain Injury by Microenvironment Regulation. *Acta Biomater* **2022**, *150*, 67–82. https://doi.org/https://doi.org/10.1016/j.actbio.2022.07.018.

(4) Foord, E.; Klynning, C.; Schoutrop, E.; Förster, J. M.; Krieg, J.; Mörtberg, A.; Müller, M. R.; Herzog, C.; Schiegg, D.; Villemagne, D.; Fiedler, U.; Snell, D.; Kebble, B.; Mattsson, J.; Levitsky, V.; Uhlin, M. Profound Functional Suppression of Tumor-Infiltrating T-Cells in Ovarian Cancer Patients Can Be Reversed Using PD-1-Blocking Antibodies or DARPin® Proteins. *J Immunol Res* **2020**, *2020*, 7375947. https://doi.org/10.1155/2020/7375947.

(5) Shaabani, S.; Gadina, L.; Surmiak, E.; Wang, Z.; Zhang, B.; Butera, R.; Zarganes-Tzitzikas, T.; Rodriguez, I.; Kocik-Krol, J.; Magiera-Mularz, K.; Skalniak, L.; Dömling, A.; Holak, T. A. Biphenyl Ether Analogs Containing Pomalidomide as Small-Molecule Inhibitors of the Programmed Cell Death-1/Programmed Cell Death-Ligand 1 Interaction. *Molecules* **2022**, *27* (11). https://doi.org/10.3390/molecules27113454.

(6) Skalniak, L.; Zak, K. M.; Guzik, K.; Magiera, K.; Musielak, B.; Pachota, M.; Szelazek, B.; Kocik, J.; Grudnik, P.; Tomala, M.; Krzanik, S.; Pyrc, K.; Dömling, A.; Dubin, G.; Holak, T. A. *Small-Molecule Inhibitors of PD-1/PD-L1 Immune Checkpoint Alleviate the PD-L1-Induced Exhaustion of T-Cells*; 2017; Vol. 8. www.impactjournals.com/oncotarget/.

(7) Tian, H.; Sakmar, T. P.; Huber, T. A Simple Method for Enhancing the Bioorthogonality of Cyclooctyne Reagent. *Chemical Communications* **2016**, *52* (31), 5451–5454. https://doi.org/10.1039/C6CC01321J.

(8) Seitchik, J. L.; Peeler, J. C.; Taylor, M. T.; Blackman, M. L.; Rhoads, T. W.; Cooley, R. B.; Refakis, C.; Fox, J. M.; Mehl, R. A. Genetically Encoded Tetrazine Amino Acid Directs Rapid Site-Specific in Vivo Bioorthogonal Ligation with Trans-Cyclooctenes. *J Am Chem Soc* **2012**, *134* (6), 2898–2901. https://doi.org/10.1021/ja2109745.

(9) Zeglis, B. M.; Emmetiere, F.; Pillarsetty, N.; Weissleder, R.; Lewis, J. S.; Reiner, T. Building Blocks for the Construction of Bioorthogonally Reactive Peptides via Solid-Phase Peptide Synthesis. *ChemistryOpen* **2014**, *3* (2), 48–53. https://doi.org/https://doi.org/10.1002/open.201402000.

(10) Pedersen, S. W.; Armishaw, C. J.; Strømgaard, K. Synthesis of Peptides Using Tert-Butyloxycarbonyl (Boc) as the α-Amino Protection Group. In *Peptide Synthesis and*

Applications; Jensen, K. J., Tofteng Shelton, P., Pedersen, S. L., Eds.; Humana Press: Totowa, NJ, 2013; pp 65–80. https://doi.org/10.1007/978-1-62703-544-6_4.

(11) McPherson, A.; Gavira, J. A. Introduction to Protein Crystallization. *Acta Crystallogr F Struct Biol Commun* **2014**, *70* (Pt 1), 2–20. https://doi.org/10.1107/S2053230X13033141.

(12) Jumper, J.; Evans, R.; Pritzel, A.; Green, T.; Figurnov, M.; Ronneberger, O.; Tunyasuvunakool, K.; Bates, R.; Žídek, A.; Potapenko, A.; Bridgland, A.; Meyer, C.; Kohl, S. A. A.; Ballard, A. J.; Cowie, A.; Romera-Paredes, B.; Nikolov, S.; Jain, R.; Adler, J.; Back, T.; Petersen, S.; Reiman, D.; Clancy, E.; Zielinski, M.; Steinegger, M.; Pacholska, M.; Berghammer, T.; Bodenstein, S.; Silver, D.; Vinyals, O.; Senior, A. W.; Kavukcuoglu, K.; Kohli, P.; Hassabis, D. Highly Accurate Protein Structure Prediction with AlphaFold. *Nature* **2021**, *596* (7873), 583–589. https://doi.org/10.1038/s41586-021-03819-2.

(13) Liu, G.; Zeng, H.; Mueller, J.; Carter, B.; Wang, Z.; Schilz, J.; Horny, G.; Birnbaum, M. E.; Ewert, S.; Gifford, D. K. Antibody Complementarity Determining Region Design Using High-Capacity Machine Learning. *Bioinformatics* **2020**, *36* (7), 2126–2133. https://doi.org/10.1093/bioinformatics/btz895.

(14) Saka, K.; Kakuzaki, T.; Metsugi, S.; Kashiwagi, D.; Yoshida, K.; Wada, M.; Tsunoda, H.; Teramoto, R. Antibody Design Using LSTM Based Deep Generative Model from Phage Display Library for Affinity Maturation. *Sci Rep* **2021**, *11* (1), 5852. https://doi.org/10.1038/s41598-021-85274-7.

(15) Rube, H. T.; Rastogi, C.; Feng, S.; Kribelbauer, J. F.; Li, A.; Becerra, B.; Melo, L. A. N.; Do, B. V.; Li, X.; Adam, H. H.; Shah, N. H.; Mann, R. S.; Bussemaker, H. J. Prediction of Protein–Ligand Binding Affinity from Sequencing Data with Interpretable Machine Learning. *Nat Biotechnol* **2022**, *40* (10), 1520–1527. https://doi.org/10.1038/s41587-022-01307-0.

List of achievements

Academic paper:

○**Boyang Ning**, Xueli Ren, Kyoji Hagiwara, Shinji Takeoka, Yoshihiro Ito, and Hideyuki Miyatake,"Development of a non-IgG PD-1/PD-L1 inhibitor by in silico mutagenesis and an in-cell protein protein interaction assay", ACS Chem. Biol., 16, 3161-323 (2021)

Eun-Hye Kim, **Boyang Ning**, Masuki Kawamoto, Hideyuki Miyatake, Eiry Kobatake, Yoshihiro Ito, and Jun Akimoto, "Conjugation of biphenyl groups with poly(ethylene glycol) to enhance inhibitory effects on the PD-1/PD-L1 immune checkpoint interaction", J. Mater. Chem. B, 8, 10162-10171 (2020)

Acknowledgement

Thanks for Prof. Yoshihiro ITO and Prof. Shinji TAKEOKA for their kindly suggestion, guidance and encouragement of my research and thesis. It was very precious experience to study in both RIKEN and Takeoka Lab.

Thanks for Dr. Hideyuki MIYATAKE for his guidance in the study of 2-PD-1, the teaching of other basic biochemistry experiment manipulations and daily encouragement and support of my research.

Thanks for Dr. Takanori UZAWA for his guidance in the study of SMI-peptide, teaching of ribosome display manipulations and peptide solid phase synthesis, and daily encouragement and support of my research.

Thanks for Dr. Masuki KAWAMOTO for his guidance in the synthesis of BMS-1166-tetrazine.

Thanks for Dr. Nandakumar AVANASHIAPPAN and Dr. EunHye KIM for their suggestions in the synthesis of BCN-peptide and PAMAMG4-BMS1166.

Thanks for Mrs. Noriko MINAGAWA, Mrs. Akiko YUMOTO and Ms. Izumi Kono as well as other technical staff in RIKEN for their daily support of my experiment.

Thanks for Mr. Liang-Chun WU, Ms. Mingxin HU, Ms. Kun FANG, Dr. Xueli REN and Dr. Hsiu-Pen Lin as well as other lab member for their suggestion, accompany for my daily life in Japan.

Thanks for my family especially my father for their support for my life and study.